Macroscale Analysis of Strain Path Change Effects in AA3104 by Digital Image Correlation

By
Yusha Lan, B. Eng

Submitted to the Faculty of Graduate and Postdoctoral Studies
In partial fulfillment of the M.A.Sc program in
Advanced Materials and Manufacturing

Ottawa-Carleton Institute for
Mechanical and Aerospace Engineering

University of Ottawa

Master of Applied Science (2014)

The Ottawa-Carleton Institute for Mechanical and Aerospace Engineering
Ottawa, Ontario

Title: Macroscale Analysis of Strain Path Change Effects in AA3104 by Digital Image Correlation
Author: Yusha Lan
Supervisor: Dr. Arnaud G. Weck
Number of pages: xix+ 158 = 177

Abstract

Cold rolled aluminum is a widely used metal in industry. The forming limit diagram (FLD) which is commonly used to predict safe deformation parameters currently fails to predict the uniform elongation after non-proportional strain path often found in industrial operations.

In this work, a non-proportional strain path change in aluminum alloy 3104 going from plane strain tension to uniaxial tension was investigated. Plane strain tensile tests have been carried out to various pre-strains (3%, 6% and 9%), followed by uniaxial tensile tests at various orientation with respect to the tensile direction (0°, 45° and 90°). Digital image correlation (DIC) was employed to analyze the strain distribution in the sample during deformation. The mechanical response was studied as a function of pre-strain and reloading angle to quantify the effect of strain path change on AA3104.

Acknowledgements

First, I would like to thank my supervisor Dr. Arnaud Weck for his advice and guidance throughout this project.

Second, I appreciate the help from the Novelis Inc. and Dr. Haiou Jin regarding their knowledge and wisdom on the properties of aluminum alloys.

Third, I would also like to thank my colleagues Elisa Cantergiani, Marina Pushkareva, Mishaal Azhar, Yaser Alinaghian, Mahyar Asadi, Amirhossein Ketabchi, Stephen Knapp, Trevor Meunier and Jean-Michel Guay in the Fracture Ottawa Group for their insightful advice and companionship.

Finally, I would like to thank my family and Gabriel Mak for their continuous support.

Table of Contents

List of Figures

List of Tables

List of Symbols

$\mathbf{m}$	A material constant in 3-D yield functions
$\boldsymbol{\sigma_e}$	The effective stress identified with the yield stress in an equibiaxial tension test in 3-D yield functions
$\boldsymbol{V_i}$	The eigenvalues of the 3 by 3 symmetric matrix in 3-D yield functions.
$\mathbf{K}$	The stress index of Hollomon equation
$\mathbf{n}$	The strain hardening exponent of Hollomon equation
$\boldsymbol{\alpha}$	A parameter to characterize strain path change
$\mathbf{d\varepsilon}$	The unit vectors, representing the plastic strain tensors just prior to the strain path change
$\mathbf{d\varepsilon_p}$	The unit vectors, representing the plastic strain tensors just after the strain path change
$\boldsymbol{\varphi}$	The angle between these two tensors
$\boldsymbol{\lambda_i}$	A weighting factor to allow for the relative intensities or strengths of the various components
$\mathbf{M}$	The Taylor factor
$\boldsymbol{\sigma_y}$	The yield stress
$\boldsymbol{\tau_o}$	The critical resolved shear stress (CRSS)
$\boldsymbol{\sigma_{be}}$	The reloading yield stress

$\boldsymbol{\sigma_r}$	The reference stress
$\boldsymbol{M_r}$	The average Taylor factor
$\tilde{\boldsymbol{\tau}}$	The effective resolved shear stress
$\boldsymbol{M_{be}}$	The average Taylor factor along the reloading direction
$\tilde{\boldsymbol{\tau}} + \Delta\tilde{\boldsymbol{\tau}}$	The effective reloading shear stress
γ, β	Material constants for the criterion for ductile fracture initiation
$\boldsymbol{\sigma_b}$	The back stress
$\boldsymbol{H_K}$	The proportionality factor of Melan-Prager hardening rule
$\boldsymbol{D_e}$	The elastic material stiffness tensor
$\boldsymbol{\lambda}$	The factor of flow rule
$\boldsymbol{n_{Linear}}$	The number of pictures in the linear middle section
$\boldsymbol{n_{tension}}$	the number of pictures during the tensile test
$\boldsymbol{t_{Linear}}$	The time when the time vs. displacement curve is in the middle linear section of the stress strain curve
$\boldsymbol{t_{tension}}$	The total duration of the tensile test
$\boldsymbol{\varepsilon_{yy}}$	The true strain in the tensile direction
$\boldsymbol{\varepsilon_{xx}}$	The true strain in the transverse direction
$\boldsymbol{\varepsilon_{zz}}$	The true strain in the thickness direction
$\boldsymbol{L_0}$	The initial gauge width
L	The instantaneous gauge width
$\boldsymbol{t_0}$	The initial thickness of the specimen

$\mathbf{t}$	The instantaneous thickness of the specimen
$\boldsymbol{A_0}$	The initial cross-sectional area
$\boldsymbol{A}$	The current cross-sectional area
$\boldsymbol{n_{pic}}$	The picture number
$\boldsymbol{D_{pic}}$	The displacement per picture
$\boldsymbol{D_{Linear}}$	The total displacement in the linear part of the test.
$\boldsymbol{P_{corrs}}$	The corresponding load
$\boldsymbol{\varepsilon_{true}}$	The true strain
$\boldsymbol{\sigma_{True}}$	The true stress
$\boldsymbol{\sigma_{corrected}}$	The stress after Bridgman correction
$\boldsymbol{\sigma_{measured}}$	The measured true stress
$\mathbf{R}$	The radius of the external neck of the sample
$\mathbf{a}$	The minimum cross sectional radius of the sample
$\boldsymbol{\sigma_{un}}$	The unloading stress at pre-strain
$\boldsymbol{\sigma_{be}/\sigma_{un}}$	The reloading yield stress divided by the unloaded stress
$\boldsymbol{\sigma_{be}/\sigma_{r}}$	The reloading yield stress divided by the reference stress
$\boldsymbol{\theta}$	The work-hardening rate
$\boldsymbol{\sigma_{UTS}}$	The ultimate stress
$\boldsymbol{\varepsilon_{necking}}$	The necking strain
$\boldsymbol{\varepsilon_{be}}$	The reloading yield strain
$\boldsymbol{\varepsilon_{e}}$	The effective necking strains after strain path change

$\boldsymbol{\varepsilon_y}$	The yield strain at pre-strain
$\boldsymbol{\varepsilon_p}$	Pre-strain
$\boldsymbol{\varepsilon_{ep}}$	The effective pre-strains
$\boldsymbol{\varepsilon_{total\ necking}}$	The total effective necking strain
$\boldsymbol{A_f}$	The final fracture area
ε_f	The true fracture strain

1 Introduction

Aluminum is the most plentiful metallic element on earth. It has various attractive properties, such as high corrosion resistance, excellent machining properties, light weight, high thermal/electrical conductivity and high ductility/deformability [1]. As a result, it has been widely used since the end of the 19^{th} century in transportation, construction, electrical, thermal and, packaging applications.

The forming limit diagram (FLD) is usually employed to characterize the deformation of aluminum sheets. However, during industrial operations, non-proportional loading is applied, which means that the metal first deforms in one direction, and then deforms in another direction. The change in straining direction is called a strain path change. Standard forming limit diagrams were found to be inappropriate to predict the deformation behavior of materials undergoing a strain path change. The typical stress-strain curve after strain path change shows transient reduction or increase in work-hardening rate which are due to plastic anisotropy. Plastic anisotropy originates from different sources at different length scale including shear bands, grain orientation, and dislocation cells.

The goal of this project is to study strain path change effects in aluminum alloy AA3104. This alloy was selected due to its strong strain path change effect. A two stage of deformation was employed. An in-plane plane strain tension followed by uniaxial tension at 0°, 45° and 90° to the pre-strain tensile axis was conducted. The

evolution of surface strain distribution during deformation was obtained using digital image correlation (DIC).

The structure of this report is as follows: Chapter 2 consists of a literature review on the relevant properties of aluminum alloys and the current knowledge related to strain path change effects in various materials. Chapter 3 is details of experimental procedures used in this thesis. The experimental results are presented in Chapter 4. Chapter 5 discusses the results in view of the current literature. Conclusions and future work are presented in Chapter 6.

2 Literature Review

2.1 Aluminum Alloys

2.1.1 Specification for Aluminum and Aluminum Alloys

Aluminum alloys can be divided into two major categories: casting compositions and wrought compositions [1]. The Aluminum Association of the United States uses a four-digit numerical system to identify aluminum alloys. The nomenclature for wrought alloys (see Table 1) is called the International Alloy Designation System (IADS). The first digit indicates the alloy group, and the last two digits identify the aluminum alloy or indicate the aluminum purity. The second digit indicates modifications of the original alloy or impurity limits. As for the cast alloys (see Table 2), although the first digit for cast alloys is essentially the same as for wrought alloys, the second two digits is used to identify a particular composition. The digit after the decimal point identifies the casting alloy limits. The 6XX.X series is unused.

Table 1. Specification for wrought aluminum and aluminum alloys [2].

Main alloying element	Four-digit designation
99.00% (min) aluminum	1 XXX
Copper	2 XXX
Manganese	3 XXX
Silicon	4 XXX
Magnesium	5 XXX
Magnesium and silicon	6 XXX
Zinc	7 XXX
Others	8 XXX

Table 2. Specification for cast aluminum and aluminum alloys [2].

Main alloying element	Four-digit designation
99.00% (min) aluminum	1 XX.X
Copper	2 XX.X
Silicon with added copper and/or magnesium	3 XX.X
Silicon	4 XX.X
Magnesium	5 XX.X
Zinc	7 XX.X
Tin	8 XX.X
Others	9 XX.X

2.1.2 **Microstructure of AA3104**

The chemical composition of AA3104 is shown in Table 3.

Table 3. Chemical composition of AA3104 [3].

Alloys	Si	Fe	Cu	Mn	Mg
AA3104	0.202	0.449	0.155	1.085	1.090

Liu et al. [4], [5] have investigated the evolution of the dislocation boundary structure during the cold rolling of AA3104 using electron channeling contrast (ECC) imaging and electron backscattered diffraction (EBSD) techniques (see Figure 1). The average grain size was approximately 36 microns, with sizes ranging from 10 to 80 microns. There are two types of second-phase particles in the microstructure of AA3104, namely, coarse intermetallics and fine dispersoids. Energy-dispersive X-ray microanalysis shows that the intermetallics, often referred to as "constituent particles", are $FeMnAl_6$ and AlFeMnSi with lengths on the range of 2-20 microns. The dispersoid particles are AlMnSi with sizes in the range of 0.1 to 0.5 microns. They have also indicated that the effect of second-phase particles on the evolution of the deformation microstructure, during cold rolling, is decided by the size of the particles.

Significant local distortions in the deformed microstructure are formed near the coarse constituent particles (see Figure 2) while, however, there is no clear effect observed in fine dispersoid particles.

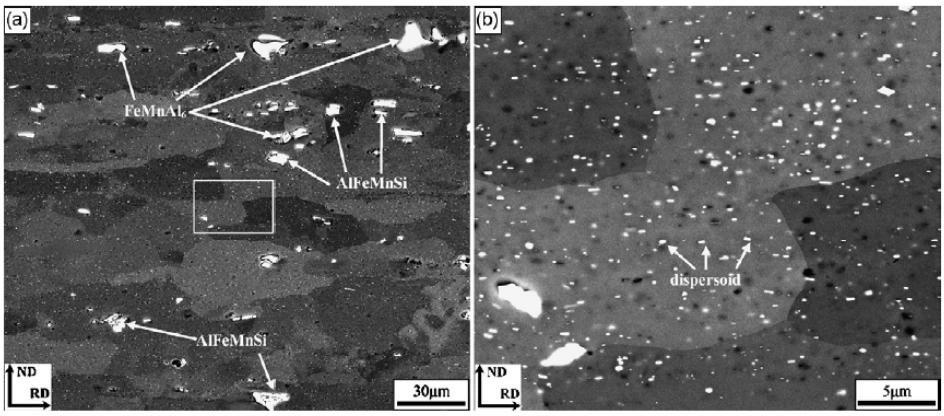

Figure 1. ECC images showing the microstructure of undeformed AA3104. (a) Large constituent particles: $FeMnAl_6$ and AlFeMnSi; (b) dispersoids within the grains (indicated by arrows) [4].

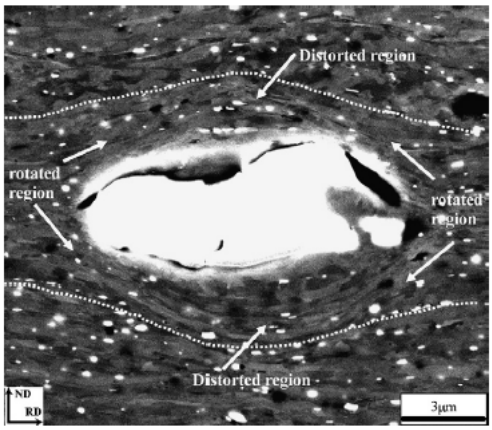

Figure 2. High magnification of view of region showing a typical deformation microstructure near large particles. The arrows indicate distorted regions and rotated regions. [4]

2.1.3 **Mechanical Properties of AA3104**

Wu et al. [6] studied the anisotropic behavior of AA3104 using the phenomenological approach via 3-D yield functions as follows.

$$\emptyset = |V_1 - V_2|^m + |V_2 - V_3|^m + |V_3 - V_1|^m = 2\sigma_e^m \qquad \text{(Equation 2-1)}$$

where the exponent m is a material constant, σ_e is the effective stress identified with the yield stress in an equibiaxial tension test and V_i are the eigenvalues of the 3 by 3 symmetric matrix.

They reported experimental results on FLD for AA3104 and achieved high agreements with their theoretical predictions, when the M-K hypothesis, which will be explained in 2.5.1, is applied. They also obtained the experimental stress-strain response of AA3104-H19 (see Figure 3) from uniaxial tensile test along rolling direction (RD). They calculated the hardening characteristic of the materials by fitting the experimental stress strain curve with Hollomon relationship:

$$\sigma = K\varepsilon^n \qquad \text{(Equation 2-2)}$$

where K is 390.4 MPa and the strain hardening parameter n is 0.07.

Later, since Wu et al. [6] didn't give the details on the measurements of FLD, Korhonen and Heikinheimo [7] repeated the test by using AA3104-H19 type aluminum sheet, with a thickness of 0.275mm and mechanical properties given in Table 4, in tensile test [8] and hydraulic bulge test. They found a good agreement with the experimental results on FLD measurement for AA3104-H19 from Wu et al [6]. However, they also found that the failure patterns in the rolling and transverse directions were distinctly different. As a result, they have corrected the strain hardening parameter to 0.04 because it was pointed out that Wu et al. [6] used higher values to compensate for the decrease in the calculated limit strains resulting from the

erroneous assumption of a pre-existing trough in the sheet. Also, they found that the failure patterns in the rolling and transverse directions were different. In the tensile test, samples loaded in the rolling direction failed transverse to the rolling direction, but in the transverse direction, the fracture was inclined at ~55° to the tensile axis. This indicates that the alloy is highly anisotropic.

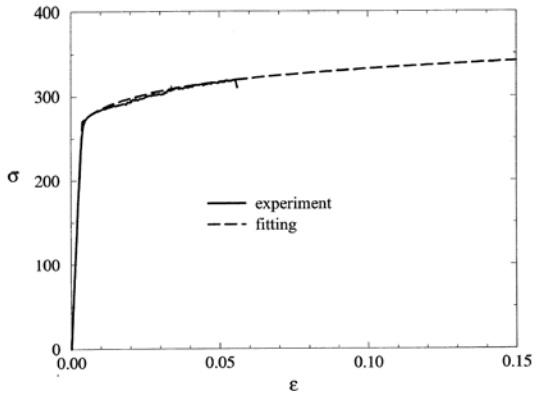

Figure 3. The experimental tensile stress-strain response in uniaxial tension along RD for AA3104-H19 [6].

Table 4. Mechanical properties of AA-3104-H19 [7].

	σ_y/MPa	σ_{UTS}/MPa	Total elongation/%
Rolling direction	277	298	3.5
Transverse direction	285	312	4.2

2.2 Observations of strain path changes in industrial settings

2.2.1 Definition of strain path change

Various studies in the literature have reported that strain path change, to some extent, can exert an influence on the substructures and flow stress. Strain path change depends on the amplitude of the change applied. To characterize this amplitude,

Schmitt et al. (1985)[9] proposed to use the parameter α defined as:

$$\alpha = \cos\varphi = \frac{d\varepsilon_p \cdot d\varepsilon}{\|d\varepsilon_p\| \cdot \|d\varepsilon\|} \qquad \text{(Equation 2-3)}$$

where $d\varepsilon$ and $d\varepsilon_p$ are unit vectors, representing the plastic strain tensors just prior to and after the strain path change, and φ is the angle between these two tensors. Accordingly, α=1 (or θ=0°), α=0 (or θ=90°) and α=-1 (or θ=180°) correspond to monotonic, cross and reverse deformations, respectively. When the α value evolves from 0 to -1, it corresponds to the Bauschinger Effect.

2.2.2 **Various strain path change tests encountered**

The experimental method, especially the loading mode, appears to be one of the important parameters when observing the strain path change. A combination of several simple loading test sequences is an effective way to investigate the dislocation structure of sheet metals under various forming conditions.[10]

E. V. Nesterova et al. [11] conducted simple-shear and uniaxial-tension/ simple-shear strain path change tests on a low-carbon Ti-killed interstitial-free (IF) steel, to observe the microstructure and texture evolution after strain path change under transmission electron microscope (TEM). X. Liu et al. [12] have studied fatigue behavior and the dislocation substructures of 6063 aluminum alloy under several non-proportional path loadings, which were circle, ellipse, rectangle, and square path (see Table 5). N.A. Sakharova et al. [13] have performed tension-rolling and rolling-tension strain path sequences on copper sheets. In both cases, two different types of strain paths were studied: the rolling and tensile directions were normal and

parallel to each other. G. Vincze et al. [14] have employed reversal tests at large strains on an AA1050 Aluminum alloy and a low carbon steel in simple shear. Also, the forward and reverse loadings were performed either at room temperature or at -120℃ to investigate the macroscopic and microscopic temperature effects. J.J. Gracio et al. [14] have performed rolling at, 0°, 45° and 135°, respectively, from the initial rolling direction (IRD), on AA1050 aluminum sheet, followed by further shear in a direction parallel to the IRD. H. Paul et al.[15] employed high purity copper single crystals with Goss {110} <001> initial orientation, pre-deformed in plane strain compression. New samples were sectioned to provide deformed crystals of Goss {110} <001>, brass {110} <112>, M {110} <111> and hard {110} <001> orientations. The first three samples were then compressed a further ~10%, while the hard {110} <001> orientation was only compressed for ~3% because the intense shear banding in this crystal promoted early shear failure.

Ghosh and Backofen [16] have developed a two-stage strain path test, identifying two kinds of mechanical behavior (the ferritic and nonferritic type) relating biaxial pre-strain to subsequent uniaxial tensile curves. Due to the limit [17] of the Ghosh and Backofen's two-stage test [16], an inplane plane strain followed by uniaxial tension in coaxial or noncoaxial tests were developed later on for the aluminum-killed steel (see Figure 4) [18],[19]. An inplane plane-strain tension test allows direct measurement of monotonic stress and strain, and with subsequent uniaxial tensile tests, also allows two-stage stress-strain measurement [18].

Table 5. The illustration of different loading paths for the multiaxial fatigue test (Adapted from [12]).

Loading path	**Proportional**	**Circle**	**Ellipse**	**Square**	**Rectangle**
Ratio of ($\sqrt{3}\tau$:σ)	1:1	1:1	1:2	1:1	1:2
Control waveform	Sinusoidal	Sinusoidal	Sinusoidal	Trapezoidal	Trapezoidal
Phase different (θ)	0°	90°	90°	90°	90°

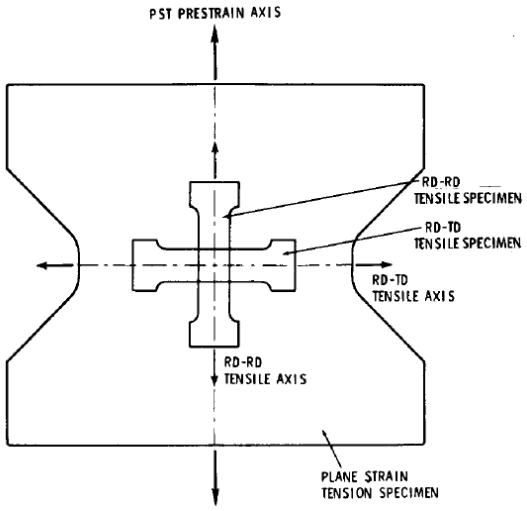

Figure 4. The configuration of second-stage tensile specimens (coaxial or noncoaxial) relative to the plain strain tension (PST) pre-strain specimen. [19]

2.2.3 **Difficulties in predicting strain path change effects**

The formability of metallic sheets is often described by the Forming Limit Diagram (FLD) introduced by Keeler and Backofen [20]. The FLD is normally determined from monotonic deformation, along almost proportional straining paths.

Laboratory punch stretching tests produce nearly linear strain paths, and consequently laboratory FLDs match the one step forming operations [21]. However, during many industrial forming operations, the straining path is non-proportional, which means that the material is first deformed (or pre-strained) on a given direction, and then deformed on another direction. Examples of this are pre-strains due to cold-rolling prior to a forming operation or the two-stage deep drawing and ironing process during the production of beverage cans. This means that the standard FLD cannot be used to predict the uniform elongation of materials undergoing non-proportional strain paths. This fact has been widely recognized. Laukonis and Ghosh [21] have reported that biaxial pre-strain can result in a lowering of the FLD. Hutchinson et al. [22] have found that a two stage tensile deformation, where the two sequential tensile tests are made perpendicular to one another, results in a significant loss in stable elongation. Lloyd and Sang [23] reported similar results on AA1100-0 and AA3003-0 when the materials were deformed 90° to the pre-strained direction. An enhanced flow stress and decrease in ductility resulted. However, the flow stress was reduced and ductility enhanced in a fine grained experimental Al-Fe-Ni alloy. In the case of AA2036-T4 and AA5182-0 the pathways were unaffected. The results showed that the forming limit diagram should be used with care when dealing with non-proportional strain paths and triggered further experimental work.

2.3 Microstructure and microtexture after strain path change

It is proposed that plastic anisotropy is responsible for the strain path change effects observed. It is suggested that plastic anisotropy originates from different sources at different length scales [24],[25]. At the microlevel, slip asymmetry and intrinsic anisotropy effects are active. At the mesolevel, dislocation substructures and shear bands are dominant. At the macrolevel, texture development [26] in polycrystalline metals is most relevant.

2.3.1 Texture

Sheet texture is expressed by both the crystallographic plane, (hkl), oriented parallel to the rolling direction and the crystallographic direction, [uvw], parallel to the rolling direction. Thus, the rolling texture is described by the notation (hkl) [uvw]. In the more complex cases, the texture can be described as consisting of a number of components of different severity

$$\text{Overall texture} = \sum \lambda_i \cdot \{hkl\}_i < uvw >_i \qquad \text{(Equation 2-4)}$$

where λ_i is a weighting factor to allow for the relative intensities or strengths of the various components.[27]

For FCC materials, copper (112)[111], brass (110)[112] and S (123)[634] orientations are the major components of the deformation texture, while the cube (001)[100] is the major component of the recrystallization texture. Figure 5 shows the four components in (111) pole for rolled austenite.

The crystallographic texture is related with the staking fault energy. The typical FCC material, such as brass, possesses low stacking fault energy. Their major texture is (110) [112], which is referred to as brass texture. For materials such as copper, aluminum, and nickel, that possess intermediate or high SFE, the major texture components are called the copper textures, *i.e.* (123) [412], (146) [211], and (112) [111].

The crystallographic texture is also portrayed by the pole figure, a stereographic projection showing the distribution of one particular set of {hkl} poles in orientation space.

Due to their heterogeneity, materials can exhibit significant plastic anisotropy during strain path change. It has been proved that the mechanical anisotropy presented by the material is related to the deformation textures [26]. To analyze the texture evolution associated with different strain path changes, Gracio et al. [26] have carried out a rolling-shear test on pure AA1050, with the shear direction making angles of 0°, 45°, and 135° with respect to the rolling direction. N. P. Gurao et al. [28] have investigated the effect of strain path change during rolling of copper and nickel. They have employed four different strain paths. They found that after the strain path change, the cross rolled samples showed weaker texture of α-brass (Bs) {110} <112> and B_{ND} {110} <111>. For the samples which had undergone parallel rolling, unidirectional rolling, and reverse rolling, exhibited strong S {123} <634> and Cu {112} <111>. They have also indicated that cross rolling has a higher number of octahedral slip

activity, which has accounted for the weaker texture in Bs {110} <112> and B_{ND} {110} <111>.

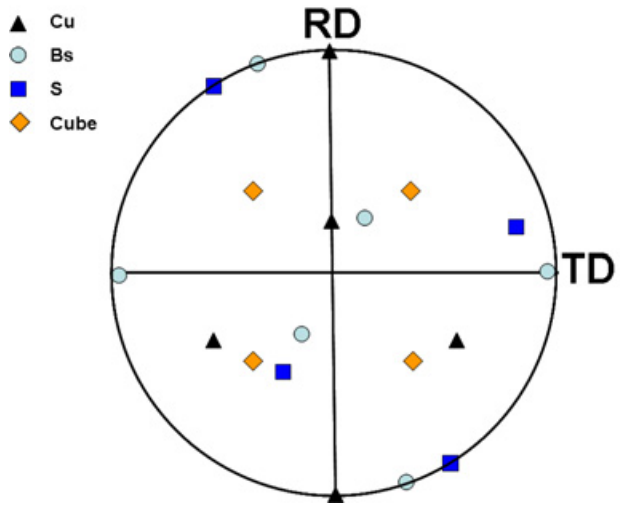

Figure 5. The copper, brass, S and cube components in (111) pole for rolled austenite.[27]

2.3.2 **Shear bands**

Shear bands, in the form of non-crystallographic band-like regions of concentrated plastic flow, are characterized by massive collective dislocation activity in a narrow local deformation zone, while the abutting matrix undergoes comparably homogeneous flow [29]. In the past few decades, there have been various studies focused on shear band formation and the related texture evolution. In some early works [30],[31],[32], the shear bands formed because of load instability, which were caused by geometric softening. The criterion for instability is $d\sigma/d\varepsilon < 0$, where σ denotes the equivalent true stress and ε the equivalent true strain. Later, other simulation studies assumed that shear bands originate from unstable perturbations of the lattice orientation in a rigid-plastic single crystal [33].

It is reported that the formation of shear bands is often associated with a sudden

drop in the local flow stress. The stacking fault energy (SFE), which can influence the formation of strong obstacles, plays an important role [29], [34] in shear band formation. In FCC materials with high or medium SFE, typical band-like dislocation substructures of elongated cells are formed. Shear bands in such materials are called Copper-type shear bands, whose related crystallographic texture are {112} <111> (Copper), {123} <634> (S) and {011} <100> (Goss). In the case of low SFE materials, shear bands are preceded by the blockage of dislocation slip by twin-matrix lamellae at an early stage of deformation. For these materials, shear bands are classified as Brass-type, whose corresponding textures are characterized by Goss and {011} <211> (Brass). In both cases, shear banding is initiated by a mechanical instability.

Various studies have been carried out to study the shear bands during strain path changes. It has been widely reported that the change of deformation path can result in the change of flow stress. Paul et al. [15] have reported that when applying a change of strain path, for the orientations where the flow stress increased by Taylor factor hardening, it is then decreased by intense macroscopic shear bands (MSB) formation. The Taylor factor, M, is normally used to relate the yield stress, σ_y, of polycrystals of cubic metals to the critical resolved shear stress (CRSS), τ_o, of a reference single crystal, as follows [35].

$$\mathrm{M} = {}^{\sigma_y}/_{\tau_o} \qquad \text{(Equation 2-5)}$$

Figure 6 shows the MSB formed after the change of strain path in different orientations, and Figure 18 is their corresponding stress-strain curve. For the “hardest”

H orientation, the traces of two intersecting families of highly localized MSB were observed (see Figure 6 (d) & (f)). In softer brass orientation and in the absence of Taylor factor hardening, more diffused MSB formation occurred (see Figure 6(b)). Korbel et al. [36] have carried out the cyclic deformation of aluminum at high strain to study the formation of shear bands. They have found that shear bands can form at high strains in FCC materials, which is independent of the mode of deformation (monotonic or cyclic). They have also indicated that shear bands form as a result of local structural softening and development of internal stresses, which are necessary for SB to nucleate and propagate through a polycrystalline material. Later, Wong et al. [37] have reported that the formation of shear bands, which causes severe strain localization, can shorten the fatigue life of ultrafine-grained Al. Also, TEM studies have shown that the shear band, in which the strain-stress field is very high, is a thin sheet of tangled dislocations having different Burgers vectors.

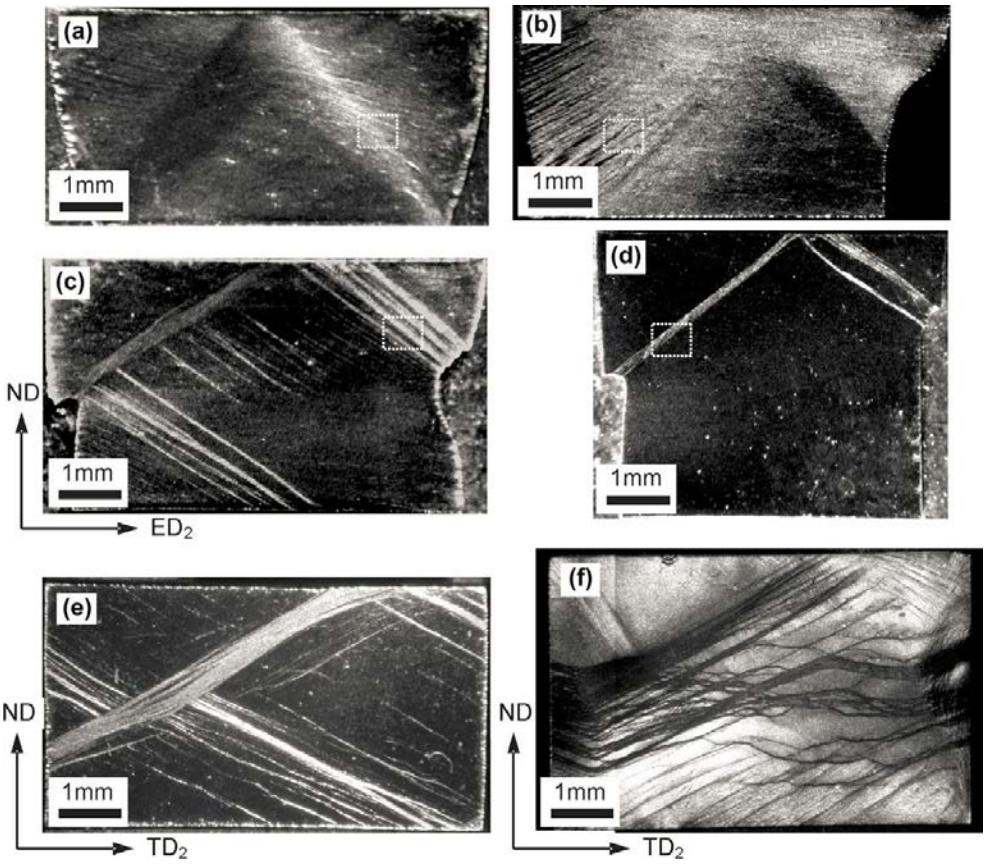

Figure 6. Macroscopic shear band formation in: (a) continuously deformed Goss {1 1 0}<0 0 1>(true strain: 0.9 + 0.1) oriented samples then after changing strain path; (b) brass{1 1 0}<1 1 2>(0.9 + 0.1); (c) M{1 1 0}<1 1 1> (0.9 + 0.08); (d) hard{1 1 0}<0 0 1> (0.9 + 0.03) orientations. Optical images in ongitudinal ND–ED2 planes (of 2nd deformation). Macroscopic shear bands in (e) M{1 1 0}<1 1 1> and (f) hard{1 1 0}<0 11 > orientations observed in the plane perpendicular to ED2. Areas marked in (a-d) show locations of more detailed investigated by TEM and FEG–SEM–EBSD [15].

2.3.3 **Grain Orientation**

It has been already proven that microstructure displays differently in the grains with different orientations after monotonic loading [38], [39]. Li and Bate [40] have stated that the orientation of the tensile axis of the pre-strain produces an influence on

the strain path change effect. Bacroix et al. [41] have studied the texture evolution in low-carbon steel sheets during reverse and orthogonal strain path change. They have indicated that grain orientation (geometrical factor) may have a significant influence on the experimental work-hardening characteristics. They used both texture evolution, which is strongly influenced by the heterogeneity of plastic deformation, and microstructural changes, which is depend on the initial and deformation-induced grain orientations, to explain the strain path change effect.

Latter, Nesterova et al. [11] showed that the stable and unstable crystal orientations for an imposed deformation mode produce different dislocation structures when they studied the microstructure and texture evolution under strain-path changes in low-carbon interstitial-free steel. In the case of reverse strain paths, a fragmentation of grains of unstable orientations can slow down the work-hardening rate. After the orthogonal deformation, there is a strong localization of plastic flow within the microband, which occurs within some grains with certain orientations and also within some grains containing well-developed pre-strain dislocation boundaries.

2.3.4 **Dislocation cells**

The distribution of dislocations after plastic straining in metal is generally heterogeneous. As shown in Figure 7, there are some regions of high dislocation density and region of low dislocation density. When the high density regions are isolated, they are called tangles. With the progression of deformation, the tangles link up with the tendency to extend into the third dimension normal to the slip plane.

Under the influence of changes in strain path, the tangle walls, *i.e.* dislocation cells (Fourie et al. [42]), are metastable structures that tend to rearrange themselves into lower energy configurations (such as subboundaries of dipole walls) [43]. This is the origin of heterogeneities in dislocation structures [44]. There is the polarity organizing attribute of tangle cell walls, which is all dislocations of one side of the cell wall (*e.g*. Figure 7, region B1) and all dislocations of the other sigh at the other side (*e.g.* Figure 7, region B2) [44].

After monotonic loading, due to the polarity of the tangled wall, the internal stress inside the wall tends to be in the same direction as the previously applied stress, *i.e.* “forward”. To balance the forward internal stress inside the cell wall, there must be a “backward” internal stress which acts to move in the direction opposite to the previously applied stress outside the cell wall, *i.e.* in the cell interior, the free-glide area [44]. The dislocation structure is composed of one or two sets of dense dislocation walls (DDWs), whose number and orientations depend on the grain orientation. B. Gardey et al. [45] have found that dual-phase steel is mainly composed of a stable and unstable orientation. When deforming in the stable orientation, TEM, Figure 8, observations show one set of DDWs developed parallel to the loading direction; while for an unstable orientation, a single set of DDWs are normal to the loading axis. In the case of intermediate orientation, there are two sets of DDWs formed, as shown in Figure 9. However, as shown in Figure 10, equiaxed cell formation was observed in aluminum polycrystalline sheet specimen deformed in

uniaxial tension to the contrary[23], [46], [47].

As for reverse loading, the microstructure is similar to that after monotonic loading, which consists of one or two sets of dislocation dense walls as shown in Figure 11. The dislocation walls are more diffused when compared to the monotonic case, which may indicate the partial dissolution of pre-existing walls. During unloading and at an early stage of reverse loading, there is an unpiling process of dynamic pile-ups formed in the cell interior during pre-straining. At the later stages of reverse loading, from a structural viewpoint, the rearrangement of dislocation characteristic is the untangling of the cell walls, which gives rise to the disintegration of the cell wall. From the viewpoint of stress-strain behavior, it is the stagnation of strain hardening. After the first dislocation has left the periphery, the dislocation which is next to the periphery becomes eligible and its stability against moving backwards has slightly decreased through the departure of the first dislocation. Additionally, the backward-moving dislocations themselves may trigger further untangling. This can be explained by the Bauschinger effect where the strain-hardening rate during reverse straining tends to become smaller than that in the previous straining at the same stress levels [44].

The orthogonal change of strain path leads to the activation of slip systems that were inactive during the pre-strain. Rao et al. [19] have studied dislocation substructure of aluminum-killed steel undergoing orthogonal strain path change. They have indicated that dislocation cell structures of the pre-strain becomes unstable and

tend to dissolve, whereas it is stable and reinforced if the tensile axis is parallel to the pre-strain axis. Due to the formation of microbands or traces of localized shearing inside the grains, the stress flow of low carbon IF steel can show a transient regime [11],[43]; while, on the contrary, the dual-phase steel will not [45]. In the case of low carbon IF steel, where the microbands formed in some grains with particular orientations, dislocation boundaries after the pre-stain are also well-developed (see Figure 12) [11]. As shown in Figure 12 (b) and (c), the interaction between microbands and pre-strain dislocation boundaries result in bending. With the increase of subsequent straining, most of the dislocation walls generated during the pre-strain tend to disappear to the benefit of the structure imposed by the last deformation. [44]

E.F. Rauch et al. [43] have also studied the dislocation substructure in mild steel performing simple shear in the 45° and 135° orientations to the pre-strain. If the second deformation mode is close to pre-strain (*e.g.* α= 45°) no peculiar behavior will be observed. When α = 135°, the yield stress is lowered; then a stagnation of the hardening occurs, which has shown to be related to dissolution of dislocation walls. In fact, the features are typical of reverse loading, and most of the active glide systems during shear were active during pre-strain but in the opposite direction. From the TEM observation in Figure 13 for AA1050-O, which were developed after plastic deformation in TD uniaxial tension and followed by simple shear at (a) 45°, (b) 90°, and (c) 135° to the TD, elongated dislocation substructure were observed in Figure 13(a) and (b), while cell dissolution were observed in Figure 13 (c).

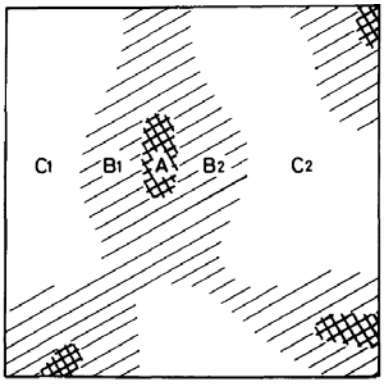

Figure 7. Three types of area in the slip plane of a deformed metal: A, B and C correspond to the core of a tangled cell wall, the whole wall, and the cell interior, respectively. [44]

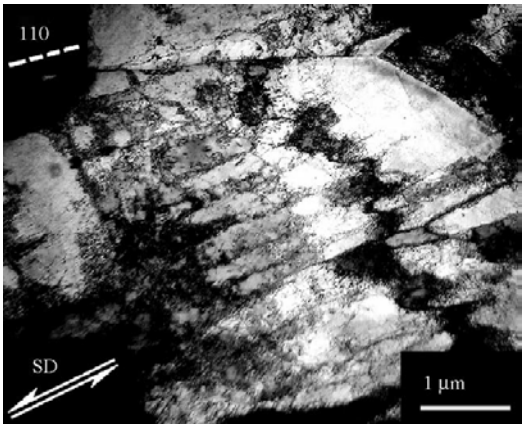

Figure 8. Intragranular dislocation structure of dual-phase steel resulting from 34% shear strain along the RD in a grain close to the stable orientation. [45]

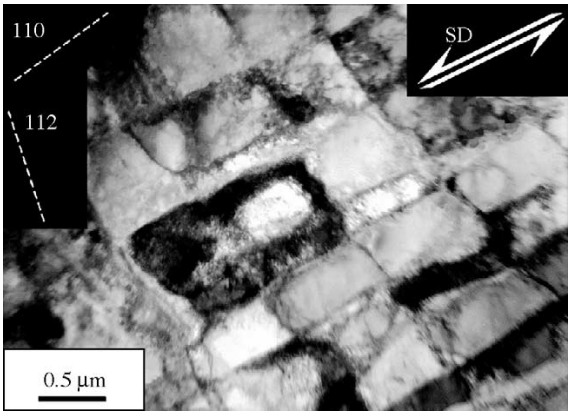

Figure 9. Intragranular dislocation structure of dual-phase steel resulting from 30% shear strain along the RD in a {1 0 0}<0 1 1> grain (intermediate orientation). [45]

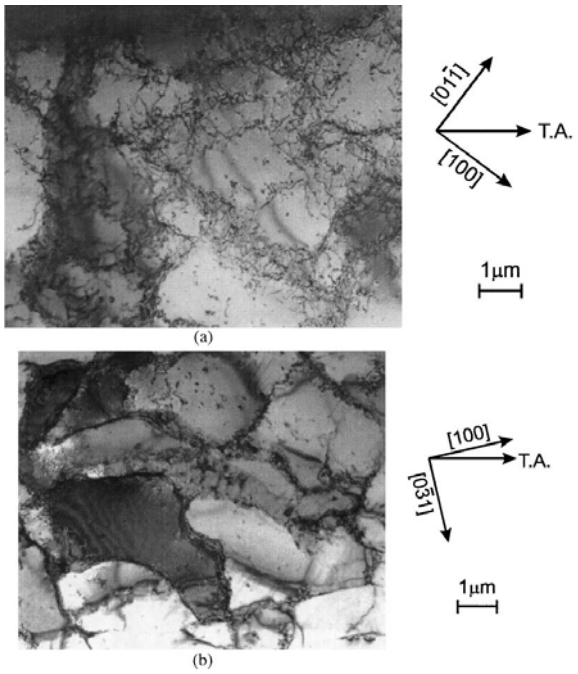

Figure 10. The TEM observation of dislocation structures developed in a grain with <011> axis normal to the AA1050-O sheet plane after uniaxial tension in the RD at strain of (a) 0.06 and (b) 0.12 (TA is the tension axis). [47]

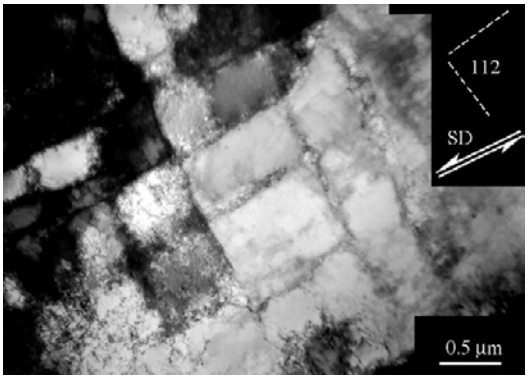

Figure 11. Intragranular dislocation structure of dual-phase steel resulting from 30%, 30% forward and reverse shear strain along the RD in a grain of intermediate orientation.[45]

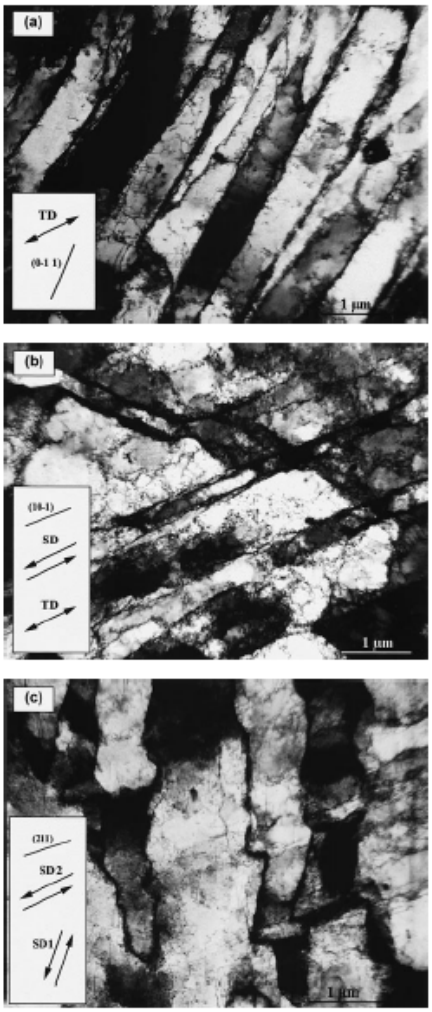

Figure 12. TEM observations of microstructures in IF steel after (a) 20% uniaxial tensile strain along RD; (b) 10% uniaxial tensile strain along RD, followed by 20% shear strain long RD; (c) 10% shear strain along RD, followed by 20% shear strain at 135° from RD. [11]

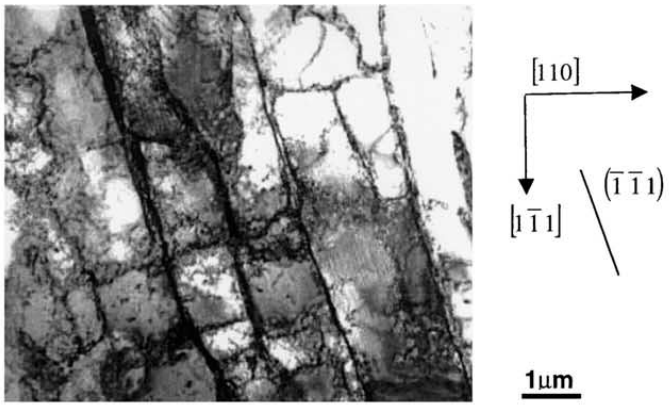

(a) TD tension – 45° simple shear. Reoganization

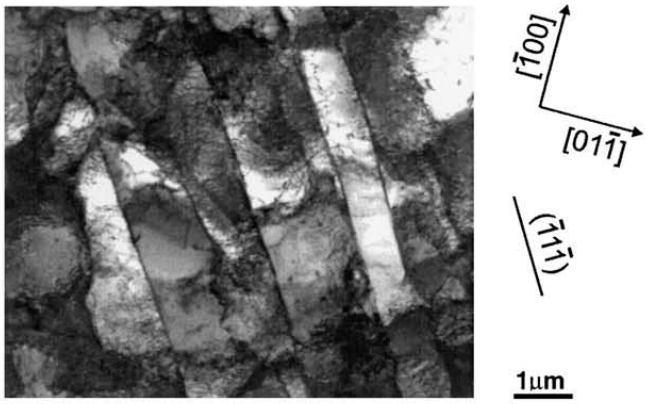

(b) TD tension – 90° simple shear. Superimposition

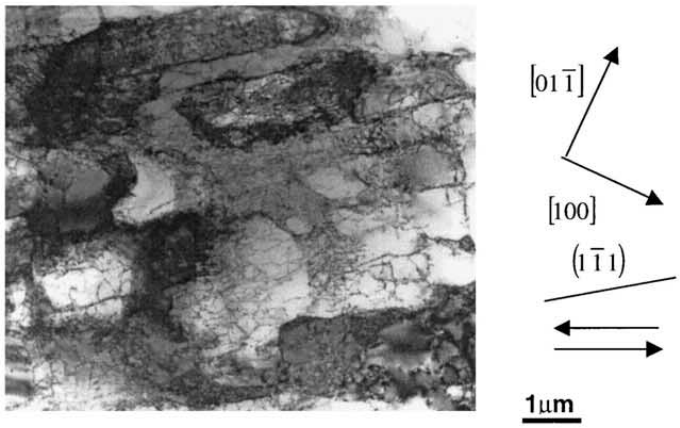

(c) TD tension – 135° simple shear. Dissolution

Figure 13. TEM observations of straight dislocation structures developed after plastic deformation in TD uniaxial tension up to a strain of 0.14, followed by simple shear up to a strain of 0.15 in different directions; (a) 45° , (b) 90° and (c) 135° shears. [48]

2.3.5 **Slip System**

Plastic slip anisotropy is one of the important micromechanical aspects of the mechanical behavior after strain path change [49]. There are various experimental results that have shown that a change in the deformation mode causes a change of active slip system set [50],[51],[52]. Experimental results [52] have shown that the second deformation commences by fine slip within the cell structure produced by the first deformation, which depends markedly on the cell size, at lower strains; while, at higher strains, coarse slip bands form. This is due to the mutual annihilation of piled-up groups of positive and negative dislocations on opposite sides of cell walls.

Latent hardening is closely related with the activation of new slip systems with the second deformation direction [49]. J.H. Schmitt et al. [50] have studied the slip systems after the strain path change in the copper sheet. They have indicated that the increase in reloading yield stress after strain path change is closely related with the activation of new slip systems. Figure 14 shows the optical observations of slip lines developed during monotonic uniaxial tension. At lower strains, one slip line direction is predominant in most of the grains. New slip line directions, which are mainly restricted near the grain boundary area, are observed for the strain value equal to or greater than 0.2 (Figure 14 (c) & (d)). Also, some bending lines can be seen when the strain is 0.3, which is related to the amount of rotation in some areas or with roughness development. During sequential tensile tests with the direction of 15°, 45° and 90° to the previous path, new slip lines are clearly observed when α=45° (Figure

15) and 90° (Figure 16), but not when α=15°. Also, they compared the slip lines with the stress-strain behavior after the strain path in different angle. When α=15°, due to the fact that the same set of slip systems are active in most of the grains for both strain paths, it has a weak evolution of the reloading yield stress. The number of new slip systems is increasingly active when the value of α is increased to 45° because the value of the reloading yield stress is maximum. When the value of α is increased from 60° to 90°, the number of new slip systems remains stationary, and the direction of the slip is even inversed in some of the new slip systems. Moreover, a more homogeneous dislocation substructure appears for α>15° as a result of the interactions between the mobile dislocation on the new active slip systems and the previous dislocation walls. Basinski et al. [53]–[55] also have a similar explanation. When the major slip system is changed, because of the second deformation, the obstacles are now relatively thin on the new primary plane. Hence the stresses produced by the dislocations meeting the obstacles can be relieved by further slip on the same system initiated on the far side of the obstacles.

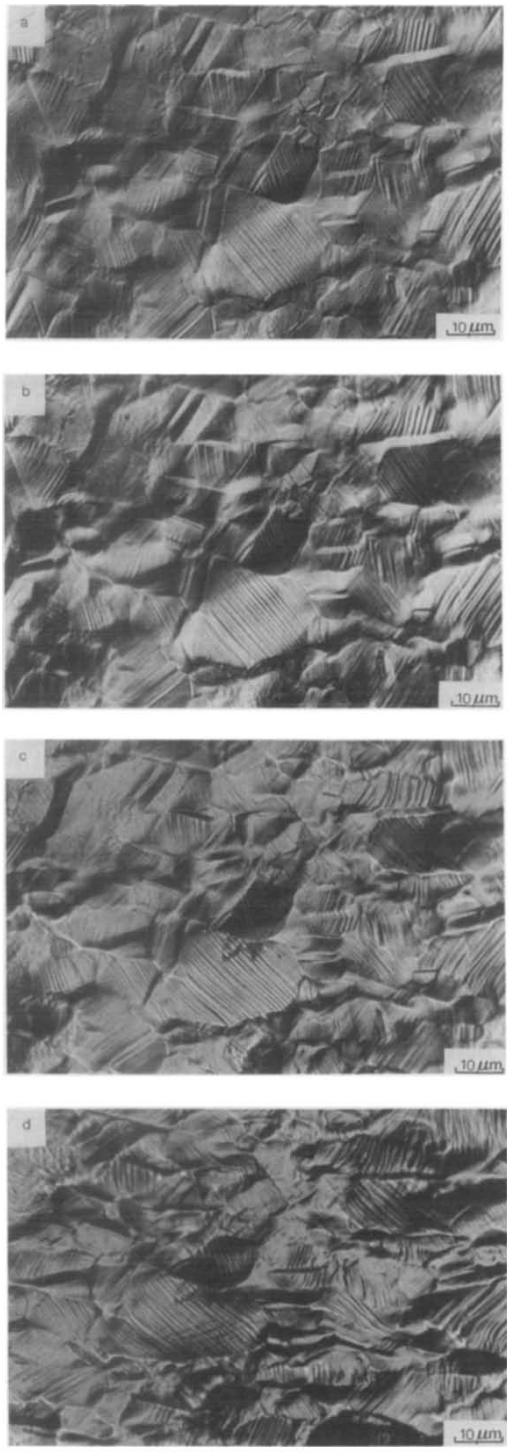

Figure 14. Optical observations of slip lines on copper developed during monotonic uniaxial tension along the reference direction (horizontal in the figure) at increased strain values of (a) 0.05, (b) 0.1, (c) 0.20 and (d) 0.30. [50]

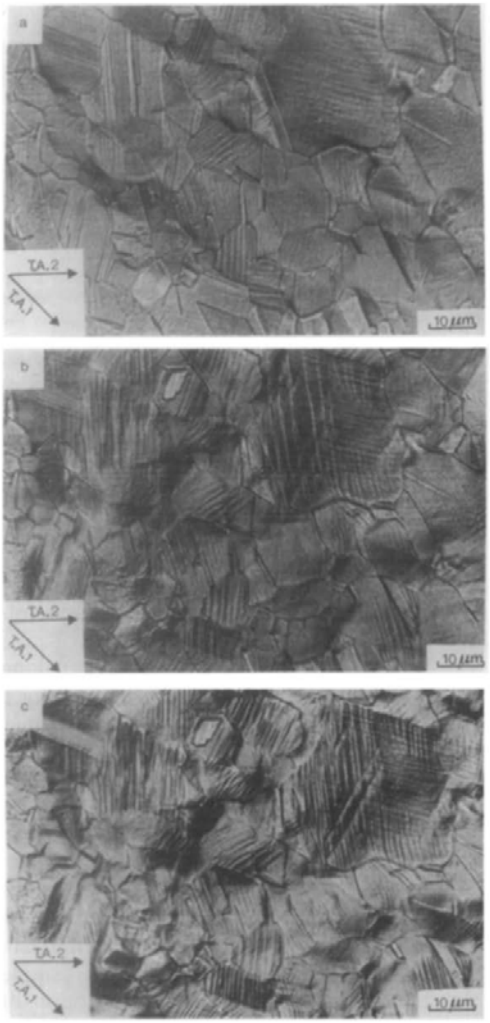

Figure 15. Optical observations of slip lines on copper developed (a) after a pre- strain of ε_p=0.12, and during the subsequent tension parallel to the reference direction at strain values of (b) 0.05 and (c) 0.15. The angle between the two tensile axes is α=45°.[50]

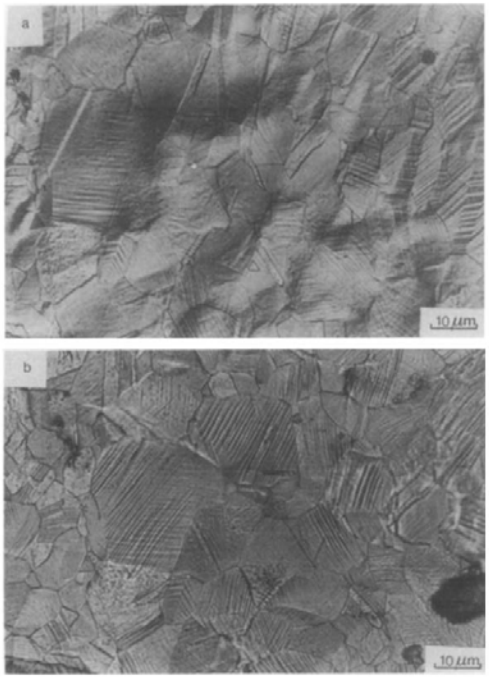

Figure 16. Optical observations of slip lines on copper developed (a) after a pre- strain of ε_p=0.12, and (b) during the subsequent tension parallel to the reference direction at a strain of 0.15. The angle between the two tensile axes is α=90°.[50]

2.4 Mechanical properties after strain path change

A change of strain path can change the mechanical properties of materials. Previous research [56] has proved that the mechanical behavior during subsequent loading appears to be only weakly affected by the first loading mode. It is mainly dependent on the magnitude of the strain path change [56].

2.4.1 Stress-strain behaviors

Transient reduction or increase in work-hardening rate occurs with a change in deformation path.

The ratio of σ_{be}/σ_r (σ_{be} is the reloading yielding stress and σ_r is the reference stress during pre-straining) can be used to characterize the evolution of reloading stress with the assumption, which is valid for low strain (less than 0.18)，that the texture evolution is weakly dependent on the tensile direction during the pre-strain [56]. During the monotonic tension, the flow stress can be expressed as the product of the average Taylor factor (M_r) and the effective resolved shear stress $\tilde{\tau}$ [57]:

$$\sigma_r = \langle M_r \tau \rangle = \langle M_r \rangle \tilde{\tau} \qquad \text{(Equation 2-6)}$$

The reloading yield stress σ_{be} can be expressed as

$$\sigma_{be} = \langle M_{be} \tau_{be} \rangle = \langle M_{be} \rangle (\tilde{\tau} + \Delta\tilde{\tau}) \qquad \text{(Equation 2-7)}$$

where $\langle M_{be} \rangle$ is the average Taylor factor along the reloading direction and $\tilde{\tau} + \Delta\tilde{\tau}$ is the effective reloading shear stress. Since σ_{be} and σ_r are defined at the same "equivalent strain" (*i.e.* for the same plastic work), the value of $\tilde{\tau}$ is the same for σ_{be} and σ_r. The ratio σ_{be}/σ_r can be calculated as

$$\frac{\sigma_{be}}{\sigma_r} = \frac{\langle M_{be} \rangle}{\langle M_r \rangle} + \frac{\langle M_{be} \rangle}{\langle M_r \rangle} \frac{\Delta\tilde{\tau}}{\tilde{\tau}} \qquad \text{(Equation 2-8)}$$

$\langle M_r \rangle$ and $\langle M_{be} \rangle$ are almost equal because of the assumption of a weak dependence on the textural evolution of the tensile direction during the pre-strain. The (Equation 2-8) becomes

$$\frac{\sigma_{be}}{\sigma_r} = 1 + \frac{\Delta\tilde{\tau}}{\tilde{\tau}} \qquad \text{(Equation 2-9)}$$

J.H. Schmitt et al. [50] have also carried out an experiment on the evolution of the reloading yield stress with respect to the angle α between the two successive tension axes with different percentages of pre-strain for copper, as shown in Figure 17. The

result has indicated that the larger the pre-strain amount, the greater the effect is. The value of normalized reloading stress increased when the angle α increases and reaches the maximum when the angle α is between 45° to 60°. Above 60°, a drop in normalized reloading stress follows. The result is in qualitative agreement with what was obtained in low carbon steel with similar experiments [58].

H. Paul et al. [15] have found that the change in strain path on copper, with subsequent deformed in four different orientations, exhibited significant differences in flow stress level in the general order: hard> M> Goss> brass, as it shown in Figure 18. The average Taylor factor can be used to define the “hard” and “soft” of the samples. The highest M_t is at H orientation, 4.9, followed by M, 3.67. Brass and Goss demonstrated $\sqrt{6}$.

As shown in Figure 19, for the complex loading history, reverse (tension-compression) or orthogonal (tension-shear) paths have exhibited pronounced differences on the material macroscopic behavior. For example, from the reverse shear loading proceeded by large shear pre-strain, in case 3 in Figure 19, a significant hardening can be observed, followed by stagnation and then resumed hardening [59]. It is first reported for Hasegawa and Yakou (1975) [46] that the “length” of the strain hardening stagnation effect, to some extent, increases with the amount of pre-strain. For the orthogonal change of loading path directions (tension-shear), as it shown in Figure 19, when loading in the orthogonal direction, a cross-hardening effect (increase of yielding followed by the work-softening rate then resumption of

work-hardening) can be observed. The transient regime is related to microband formation [11]. However, for dual-phase steel no cross-hardening effect can be observed after an orthogonal loading [60].

Ghosh and Backofen [16] have developed a two-stage strain path test, which has identified two kinds of mechanical behavior relating biaxial pre-strain to subsequent uniaxial tensile curves. The ferritic type (*e.g.* aluminum-killed steel) shows a higher subsequent tensile yield stress after biaxial straining, and this differential increases for larger pre-strains. The nonferritic type (*e.g.* 70/30 brass) shows premature yielding in subsequent tension, with the effect enhanced at larger pre-strains. Commercially pure aluminum, 1100-0, was intermediate, showing only small effects of strain path changes.

Later, a tensile deformation, coaxial or non-coaxial, following a pre-strain in plane strain tension, was performed on the aluminum-killed steel [18], [19]. The stress strain behavior, as shown in Figure 20, exhibits increases in yield. This is an earlier onset of strain localization and less work-hardening than it would exhibit had it been subjected to an equivalent uniaxial pre-strain. The effects are generally larger if the tensile axis is nonaxial [19].

However, as shown in Figure 21, when the uniaxial tension in TD was conducted for AA1050-O with interrupted deformation with unloaded specimens for 2 days, the stress was lower than the monotonic loading, which indicated that static recovery occurred [48]. Also, as shown in Figure 22, they observed that lower reloading yield

stress when AA1050-O was pre-strained in 45° and 90° than the monotonic loading. In Figure 22 (a), lower stress was observed after it was pre-strained in 45° to the previous deformation, while for the strain path change angle is 90°, higher stress was observed than the monotonic loading after yielding as shown in Figure 22 (b).

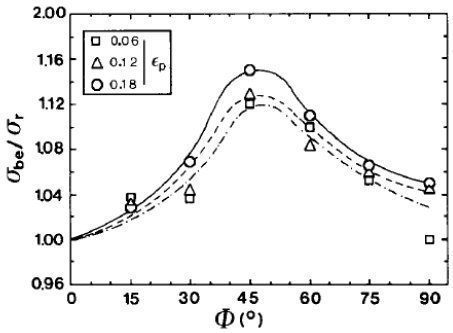

Figure 17. Evolution of the normalized reloading stress σ_{be}/σ_r with the angle α between the two successive tension axes of copper [50].

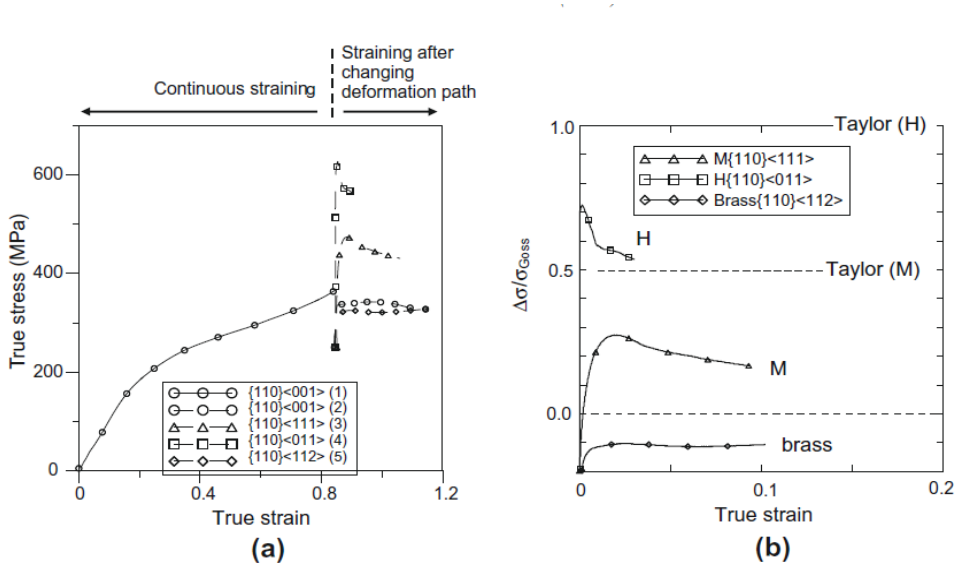

Figure 18. (a) True stress-true strain curves for pre-strained samples and deformed after strain path change; (b) stress-strain curves of crystals during restraining relative to Goss crystal [15].

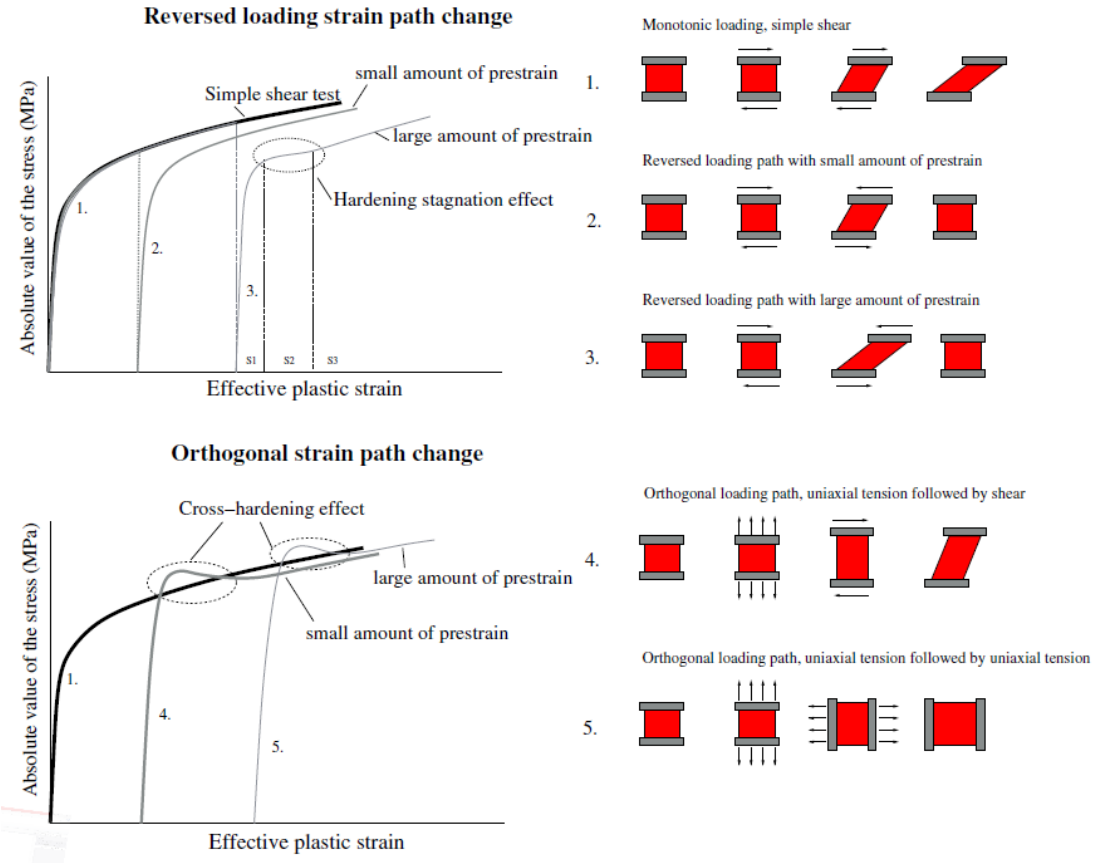

Figure 19. The stress-strain curve for different loading paths of monotonic, reversed and orthogonal strain paths [59].

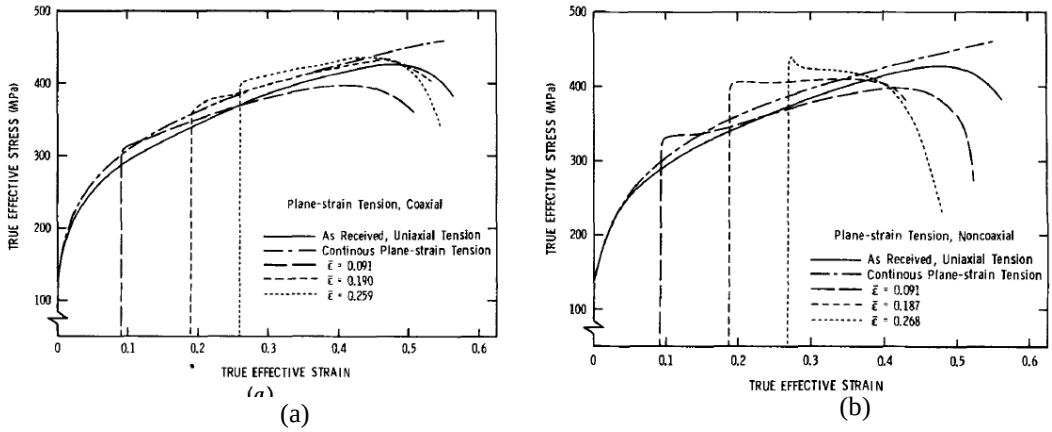

(a) (b)

Figure 20. Uniaxial tension stress-strain curve of aluminum-killed steel after pre-strain in plane strain tension. (a) coaxial, and (b) noncoaxial. [18]

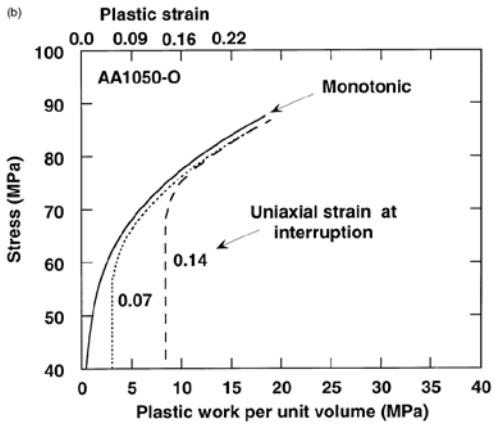

Figure 21. The stress vs. plastic work curves obtained in TD uniaxial tension and interrupted deformation with unloaded specimens for 2 days at the strain of 0.07 and 0.14. [48]

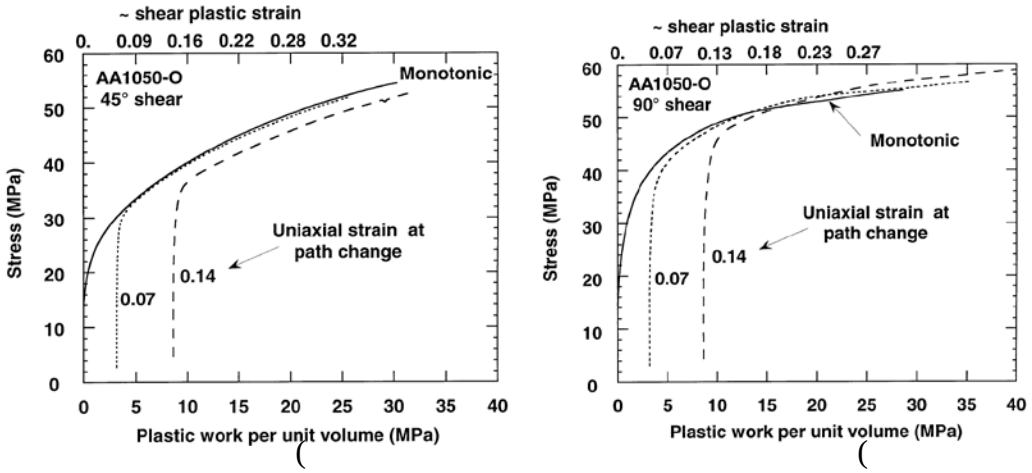

Figure 22. The stress vs. plastic work curves obtained in TD uniaxial tension of 0.0, 0.07 and 0.14 followed by (a) 45° and (b) 90° simple shears. [48]

2.4.2 **Work-hardening rate**

As mentioned before, large changes in strain path caused the dislocation cell structures generated in the first mode of deformation to become unstable. In the early stages of the second mode of deformation, the original cell structures were disrupted and appeared to be progressively dissolved and then, in continued second stage deformation, a new cell structure was built up [44], [46]. Relative to the

work-hardening rates developed in the monotonic deformation, the first phase of the dislocation rearrangement appeared to coincide with a reduction in hardening rate and the formation of a new cell structure with a recovery in hardening rate towards that characteristic of monotonic deformation [59].

There are two types of changes in work-hardening rate which is caused by the reorganization [61]. The first kind tends to increase hardening rates in the early stages of the second deformation when compared to the one in the monotonic deformation, which is influenced strongly by the effects of reorientations of directional components of the internal stresses which are generated in the first deformation. At the early stages of the second deformation, reorientation of directional internal stresses which are inherited from the pre-strain is a source of increase in hardening rate which is absent in continued monotonic deformation [61], [62]. The changes of second one, which is tend to cause transient reductions in the hardening rates, are considered to cause due to the dislocation barriers which were generated by dislocation interactions during the pre-strain stage are unstable in the second mode [61].

Figure 23 shows the work-hardening rate and stress vs strain for AK steel which strain path change angle is (a) 45° and (b) 90°. As shown in Figure 23, the changes in strain path were accompanied with substantial increases in the initial flow stress with the pre-strains more than ~0.1 [62]. Also, transient reductions in work-hardening rate were clearly developed after 0.05 pre-strain after strain path change. However, as shown in Figure 24, there is no transient reduction can be observed for air-cooled

AA2014-A300 stretched at 90° to the RD after pre-strains in RD [61]. The absent of the transient reduction is due to dynamic strain ageing (DSA),which is related with PLC effect [61]. They believed there is a large directional internal stressed developed in the dispersion-hardened microstructure, which leads to the positive contributions are dominant the changes in work-hardening caused by large changes in strain path. As a result, the limits of the effective uniform elongation are improved by the changes in strain path [61].

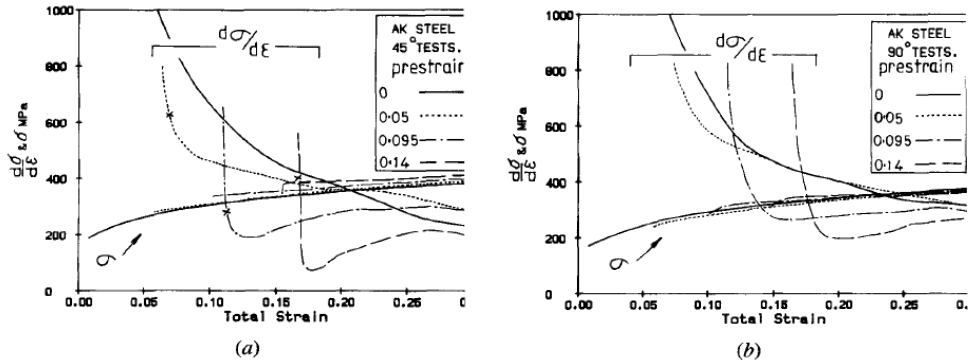

Figure 23. Stress and work-hardening rate as a function of total effective strain for AK steel pre-strained in uniaxial tension in RD. Tested after (a) a 45° change in strain path and (b) 90° change in strain path. [62]

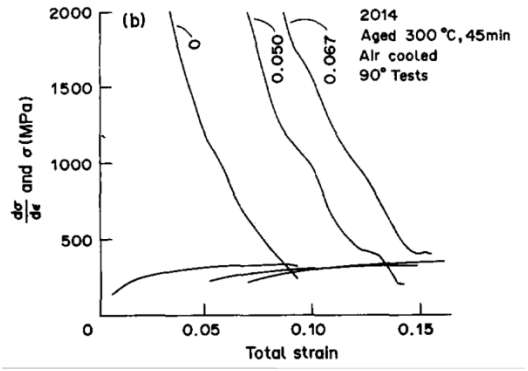

Figure 24. Stress and work-hardening rate as a function of total effective strain for air-cooled AA2014-A300 stretched at 90° to the RD after pre-strains of 0, 0.050 and 0.067 in the RD.[61]

2.4.3 **Forming Limits Diagram**

The formability of metal sheet is usually characterized with the principal strains which are produced during the sheet metal forming operations. The Forming Limit Diagram (FLD), introduced by Keeler and Backofen [20], is often used to predict the behavior of sheet material. It is generated by plotting the major strain and minor strain values on the plane of sheet materials in 2D strain space in monotonic proportional strain paths. The major (ε_1) and minor strains (ε_2) correspond with the rolling and transverse sheet directions (RD and TD). As shown in Figure 25, the FLD of the low carbon steel. The Forming Limit Curve (FLC) in Figure 25 represents the boundary between the safe regions and the onset of necking. The area below the curve is where the sheet does not exhibit visible necking, and the area above the curved is the region where the material will form visible necking (local necking) or failure. The FLDs are strongly influenced by the mechanical properties of materials, such as hardening behavior, plastic anisotropy, and strain rate sensitivity [63].

The Forming Limit Diagram is based on nearly linear strain path experiment. However, during many industrial forming operations, the straining path is non-proportional, which means the materials often are pre-strained in one direction and the following deformation on another direction. Experiments on Al 2008-T4 using two-stage strain paths have shown that changes in strain path have exerted a large influence on the forming limits [64]. The result [64] (Figure 26) shows that pre-straining in biaxial tension can lower the forming limits for the entire FLD, while

pre-straining in uniaxial tension (Figure 27) raises the limits on the right-hand side of the FLD major strain axis, without much effect on the left-hand side. Pre-straining in plane-strain tension (Figure 28) raises both sides away from the minimum. Also, it was found that, after pre-straining, the amount of the additional plane-strain deformation depends on the effective strain during pre-strain, regardless of the original strain path.

Later, an anisotropic constitutive model, which is based on texture and dislocation structure, and applied in conjunction with the Marciniak-Kuczynski [65] analysis of the forming limit strains, was applied to predict the forming limit diagrams (FLDs) by Shunji Hiwatashi et al. [63]. It has been shown that for proportional straining, limit strains near equibiaxial stretching are significantly influenced by the initial texture, back stress and slip systems, Figure 29. Also the effect of strain path changes was studied for the following two-stage strain paths:

1. $\alpha = -0.5$ to $\alpha = 1$, *i.e.* axisymmetric tension followed by equibiaxial stretching;
2. $\alpha = -0.5$ to $\alpha = 0$, *i.e.* axisymmetric tension followed by plane strain stretching;
3. $\alpha = 1$ to $\alpha = -0.5$, *i.e.* equibiaxial stretching followed by axisymmetric tension;
4. $\alpha = 1$ to $\alpha = 0$, *i.e.* equibiaxial stretching followed by plane strain stretching.

The authors could reproduce the experimental tendencies with the developed model, but they could not be predicted by the conventional model. This is related to the occurrence of transient hardening in Figure 30.

Furthermore, the effect of first strain magnitude and the combination of the first and second strain modes on the limit strains were discussed [63]. It was suggested that transient hardening significantly reduces the forming limit strain for a strain-path

change from equibiaxial stretching to uniaxial tension. Finally, it was found that for more accuracy other factors such as texture evolution, damage, and strain rate sensitivity should be taken into account.

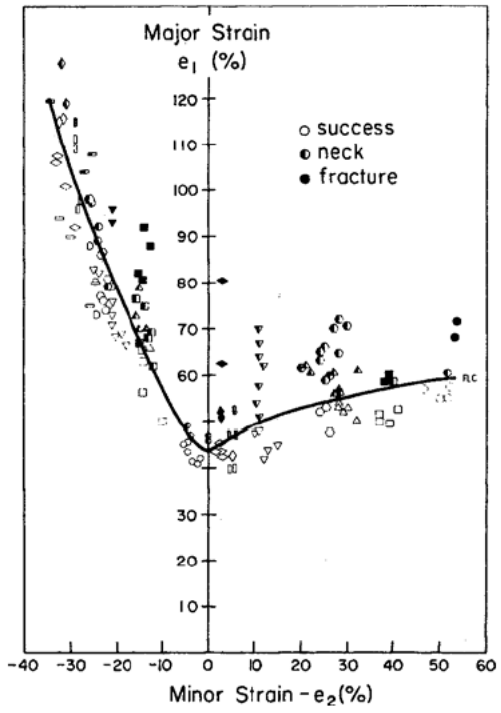

Figure 25. Forming limit diagram for low carbon steel. The strains below the curve are acceptable but those above the curve correspond to failure or necking [66].

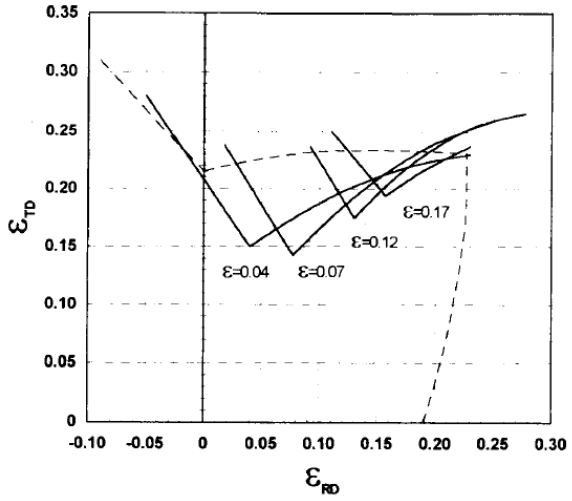

Figure 26. FLDs normal to RD after pre-straining in equibiaxial tension [64].

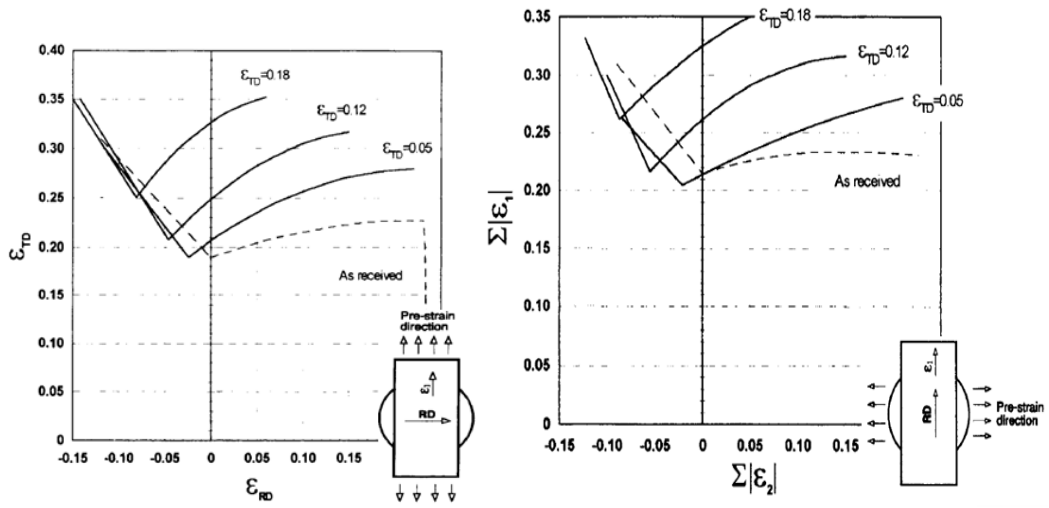

(a) (b)

Figure 27. FLDs (a) normal and (b) parallel to RD after pre-straining in uniaxial tension [64].

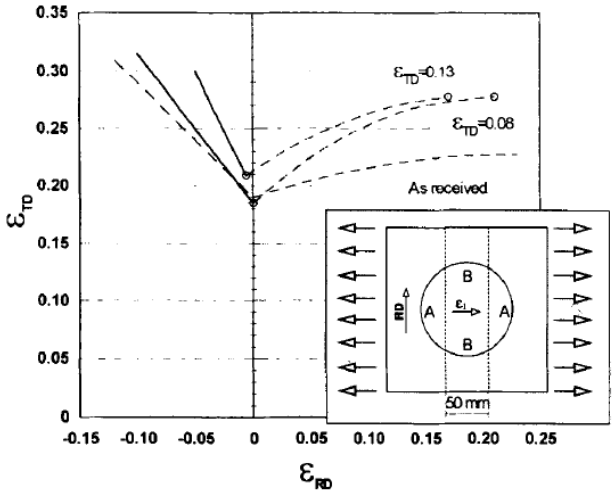

Figure 28. FLDs normal to RD after pre-straining in near plane strain tension normal to the RD [46].

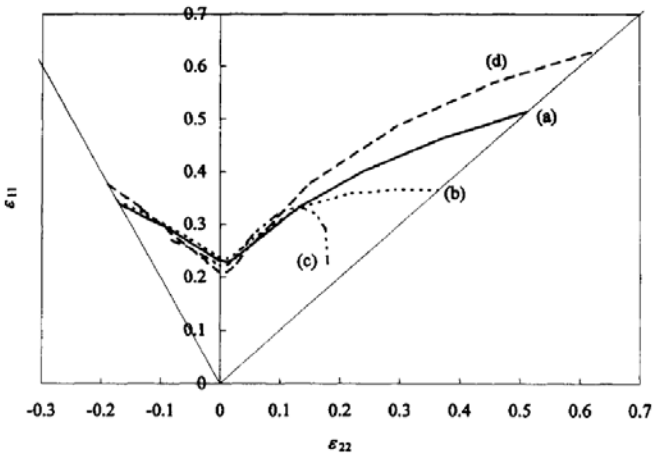

Figure 29. Forming limit curves for proportional straining predicted by (a) an anisotropic hardening model with a yield locus of mild steel where BCC type slip systems are assumed, (b) an anisotropic hardening model with a yield locus of a random-texture material where BCC type slip systems are assumed, (c) an anisotropic hardening model with a yield locus generated from the mild-steel texture where FCC type slip systems are assumed, and (d) an isotropic hardening model with the same initial yield locus as (a) [63].

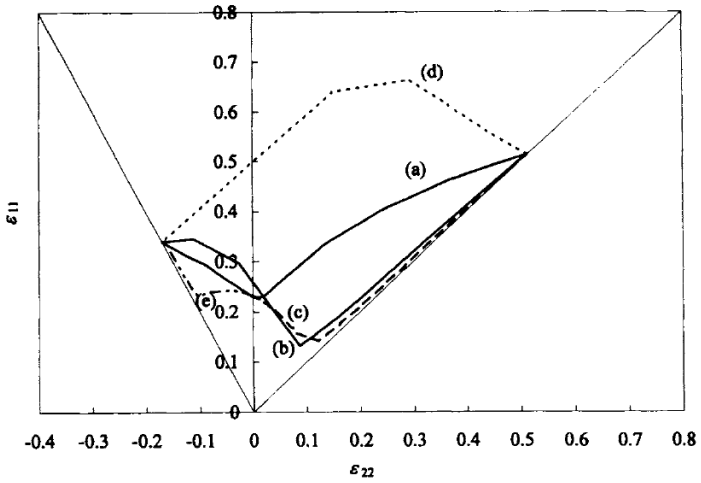

Figure 30. FLD for several strain paths. It is predicted with an anisotropic hardening model. Forming limit curves correspond to (a) proportional straining, and two-stage strain paths (b) from p = 1 to -0.5, (c) from p = 1 to 0, (d) from p = -0.5 to 1, and (e) from p = -0.5 to 0. The curves for non-proportional straining are generated by changing the amounts of the first strain [63].

2.4.4 **Fracture**

In some previous works of the effects of strain path changes on sheet metal formability, the failure is usually dictated by the onset of localized necking [21], [23], [67]. However, the forming limit diagrams fail to provide information on the influence of strain history on tensile failure [68].

Generally, ductile fracture may be divided into three stages [69]:

Stage 1 Void nucleation caused by debonding between inclusions and matrices or cracking of particles.

Stage 2 Void growth due to plastic deformation under triaxial stress states.

Stage 3 Coalescence of voids, representing the initiation of a microcrack, due to local necking among growth voids.

Although the ductile failures can be divided into the three stages above, it is hard to identify each stage due to the time intervals among these stages that may be too

short and that they probably occur simultaneously [70]. Hancock et al.[71] defined the initiation of ductile fracture as when the maximum tensile load point is reached in the load-displacement curve, the load starts to decrease gradually. The onset of necking is defined as intersection of true stress strain curve and the work-hardening rate θ ($=d\sigma/d\varepsilon$) curve as below.

$$d\sigma/d\varepsilon = \sigma \qquad \text{(Equation 2-10)}$$

where σ and ε are the true stress and true strain respectively.

During this load decrease a sudden sharp change of the downward slope occurs in the curve, which is defined as 'point S' (the point of ductile fracture initiation), see Figure 31.

From the Hollomon equation (Equation 2-2), one can get

$$d\sigma/d\varepsilon = \sigma = K\varepsilon^n \qquad \text{(Equation 2-11)}$$

Since the K and n are constant, the higher work-hardening rate leads to higher uniform elongation [72].

Also, Keitrao Enami [70] used the following equation, as the criterion for ductile fracture initiation, for the relationship between stress triaxiality and critical equivalent plastic strain, where γ and β are material constants.

$$\varepsilon_f = \gamma * exp\left(-\beta \frac{\sigma_m}{\sigma_e}\right) \qquad \text{(Equation 2-12)}$$

By applying the definition of the initiation of ductile fracture (Hancock et al. [71]) and the criterion for ductile fracture initiation, Keitrao Enami [70] studied the effect of both compressive and tensile pre-strain on ductile fracture initiation in two kinds of

steels and compared it with the numerical method. The results indicated that compressive pre-strain leads to cleavage cracking and reduces ductility.

J. Arndt et al. [73] studied the ductile failure of steel subjected to various load histories. Their researches concluded that the shape of voids and the triaxiality at initiation exhibit a strong influence on the initiation values. The failure strains are sensitive to strain history.

In Figure 32, Laukonis and Ghosh [21] plotted tensile elongations on uniform elongation and total elongation for (a) A-K steel and (B) AA2036-T4 as a function of balanced biaxial pre-straining. For steel, biaxial pre-straining cause the uniform elongation drop to almost zero when the effective pre-straining is around 0.08, while the total elongation does not decrease as fast beyond this point. This is because the elongation beyond the maximum load is controlled by strain-rate sensitivity, which is positive for A-K steel. As for the AA2036-T4, the elongation after the uniform elongation is small is due to the alloy has a negative strain-rate sensitivity. The strain-rate sensitivity is relatively unaffected by pre-strain.[21]

D. Chae et al.[68] studied the failure behavior of structural steel, HY-100, which has been pre-strained at a high stress triaxiality and subsequently failed at a lower stress triaxiality. Considering the change of triaxiality caused by the change of geometry during deformation at the notch [73], they have investigated the strain-path change loading sequence by employing a two-step loading sequence consisting of high stress triaxiality (D-notch) pre-strain followed by low stress triaxiality (B-notch)

strain to failure. The results showed that there is a decrease in the failure strain when compared to that deformed only at the lower stress triaxiality.

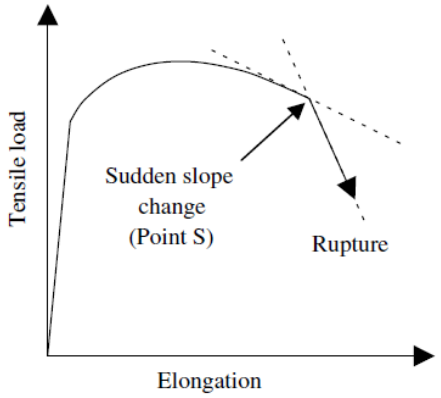

Figure 31. Schematic illustration of the load–elongation curve in the round notched tension test [70].

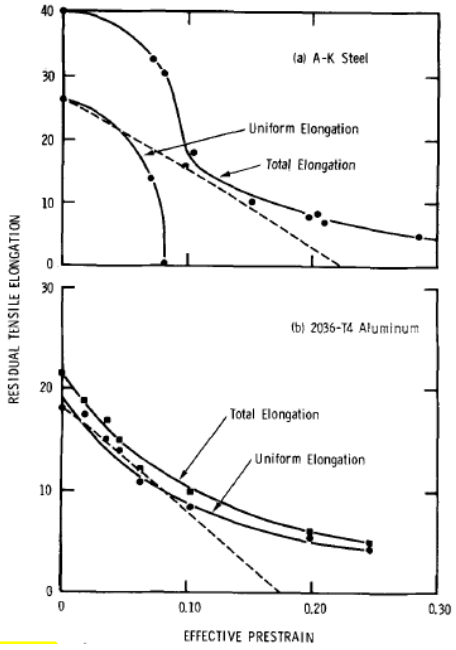

Figure 32. Uniform and total elongations in a tensile test (over a 50.8mm gage length) after biaxial pre-straining. (a) A-K steel, (B) 2036-T4 aluminum. (The dashed curves represent the expected behavior of uniform strain if pre-strain was uniaxial).[59]

2.5 Modeling approaches for predicting strain path changes

2.5.1 Marciniak-Kuczynski model

For the forming limit diagram, Marciniak (1965) and Marciniak and Kuczynski (1967)[74] have developed a limit curve prediction model on the basis of the experimental investigations concerning the strain location. This model is based on the hypothesis of the existence of imperfections in sheet metal. According to Marciniak's hypothesis, due to the manufacturing process, sheet metal has geometrical imperfections (thickness variation) and/or structural imperfections (inclusions, gaps). In the forming process these imperfections give rise to the necking of the sheet metal. The hypothesis has been experimentally shown by Azrin and Backofen (1970) [75]. This model has correctly predicts the influence of different process or material parameters on the limit strains. However, the prediction results are very sensitive to the constitutive equations used, as well as to the values of the non-homogeneity parameter.[76]

2.5.2 Microstructural model

As we known from previous literature that strain path change effects are due to the induced plastic anisotropy, which are resulting from prior deformation steps. The plastic anisotropy is originated from different sources at different length scales. However, the evolution of dislocation microstructures has been recognized as a main

driver triggering the observed anisotropic materials behavior [24].

Teodosiu and Hu [77] developed an elastic-plastic model with three internal variables showed the influence of the predeformation on the yield loci and on the subsequent work-hardening behavior of mild steel. Several intragranular deformation mechanisms, such as formation of dislocation structures under monotonic deformation, depolarization of preformed microstructural under stress reversal, and the interaction between preformed microstructure and microbands, had been taken into considerations when choosing the internal variables and their evolution equations. However, this model had only considered the contribution of dislocation structures and initial texture to the induced anisotropic work-hardening, which disregarded the dependence of dislocation structure and density on grain orientation [78]. In the case of large strain, the influence of texture evolution cannot be neglected.

Later, Peeters et al. [25], [79] attempted to address a method of incorporating dislocation ensembles in the crystal plasticity constitutive framework in strain path change, using a full-constraints Taylor model (see Figure 33). They have incorporated more details of the microstructure evolution at the grain boundary, where statistically stored dislocation densities in the cell interiors, cell-boundary dislocation densities, immobile dislocation densities, and directionally movable dislocation densities in the cell-block boundary, are taken as internal variables. The polarization of these structures during strain-path change was also discussed in the literature.

According to Mughrabi [80], a cell structure can be ideally regarded as a

two-component material, which is consisted of cell walls and cell interior. Yalcinkaya et al. [24] developed a composite dislocation cell model, which has combined the BCC crystal plasticity framework and the dislocation structure evolution to describe the strain path change effects (see Figure 34). This composite of cell substructure (see Figure 35) is characterized by wall thickness w, the cell wall r, the dislocation densities in the cell walls ρ^w, and the cell interiors ρ^c. Similarly, Viatkina et al. [81] developed a micromechanical model of dislocation cell structure to describe the strain path change effect of FCC metals, *i.e.* the induced anisotropy and its dependency on the amount of pre-strain. The FCC metal with a cell structure (see Figure 36) is idealized by compositing of four uniform components: the cell interiors and three mutually perpendicular sets of cell walls. Two types of dislocation are introduced into this model: geometrically necessary dislocations, which are related with the long-range internal stresses, and statistically stored dislocations, which influence the local deformation behavior by short-range interactions with gliding dislocations.

Fajoui et al. [82] applied a two-level homogenization approach for the micromechanical modeling of the elastoplastic material behavior during various strain-path changes. There is a two-scale transition approach, a micro-meso transition, which is based on a modified elastoplastic self-consistent approach by considering dislocation evolution and a meso-macro transition, which is used to deduce the macroscopic behavior of the polycrystal by a self-consistent model, which can be applied in both FCC and BCC metals containing a cell structure.

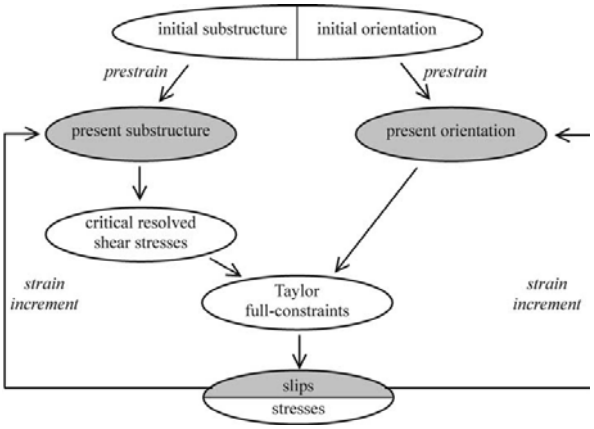

Figure 33. Implementation of microstructural model in a full-constraints Taylor model (Peeters et al. [79]).

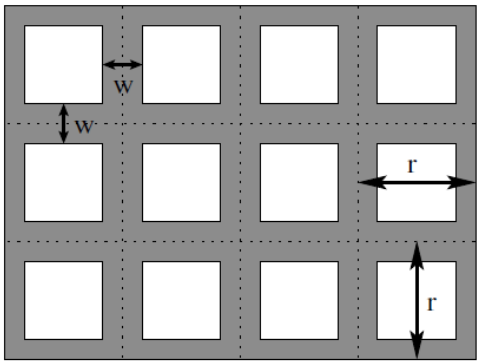

Figure 34. The composite of BCC cell substructure. [24]

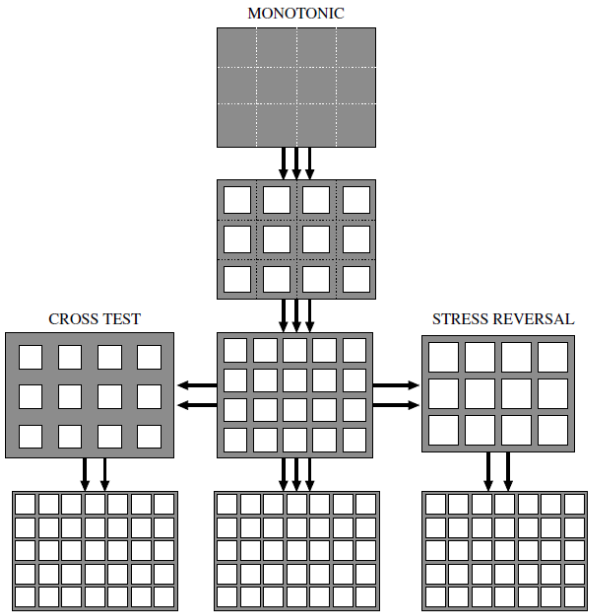

Figure 35. Schematic evolution of a BCC dislocation cell structure under strain path change. [24]

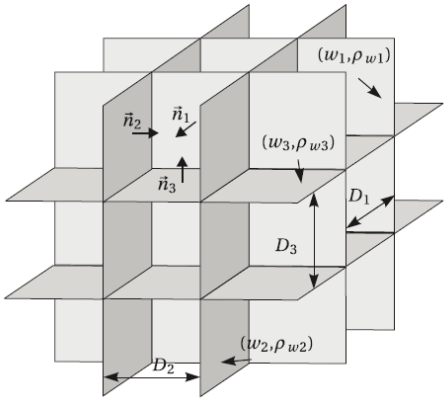

Figure 36. Model geometry of the FCC cell structure and its components [81].

2.5.3 **Kinematic hardening**

Various studies have been made to study the hardening behavior during the complex loading paths. For the monotonic loading, the isotropic hardening, introduced by Odqvist [83] has been widely used. However, strain path changes have induced more complicated phenomena. As it is mentioned before, Bauschinger effect is caused by the back stress. It is described by kinematic hardening. Since the Bauschinger effect is orientation dependent, kinematic stress is represented by a tensor, Stouffer and Dame. [84]

2.5.3.1 **Linear kinematic hardening**

Kinematic hardening leads to a translation of the loading surface, *i.e.* to a shift of the origin of the initial yield surface (see Figure 37(b)). If the initial yield surface can be described by a yield function of the form

$$f(\sigma) = F(\sigma) - \sigma_o \qquad \text{(Equation 2-13)}$$

the shifted surface is

$$\mathrm{f}(\sigma, \sigma_b) = F(\sigma - \sigma_b) - \sigma_o \qquad \text{(Equation 2-14)}$$

where σ_b is the back stress which represents the center of the shifted elastic domain, and plays the role of tensorial hardening variable. Melan[85] and Prager[86] have proposed a linear kinematic hardening law that governs the evolution of the back stress, which is called the Melan-Prager hardening rule.

$$\dot{\sigma_b} = \overline{H_K}\dot{\varepsilon_p} \qquad \text{(Equation 2-15)}$$

The proportionality factor $\overline{H_K}$ is directly related to the plastic modulus.

The consistency condition is

$$\frac{\partial \mathrm{f}}{\partial \sigma} : \dot{\sigma} + \frac{\partial \mathrm{f}}{\partial \sigma_b} : \dot{\sigma_b} = 0 \qquad \text{(Equation 2-16)}$$

And then the elastic stress-strain law ($\sigma = D_e : (\varepsilon - \varepsilon_p)$), where D_e is the elastic material stiffness tensor, flow rule ($\dot{\varepsilon}_p = \dot{\lambda} f_\sigma$) and hardening law are used to eliminate the unknowns except the rate of the plastic multiplier. Denoting again $\frac{\partial \mathrm{f}}{\partial \sigma} = \frac{\partial \mathrm{F}}{\partial \sigma} = f_\sigma$, and realizing that $\frac{\partial \mathrm{f}}{\partial \sigma_b} = -\frac{\partial \mathrm{F}}{\partial \sigma} = -f_\sigma$, the resulting equation can be written as

$$f_\sigma : D_e : (\dot{\varepsilon} - \dot{\lambda} f_\sigma) - f_\sigma : f_\sigma \overline{H_K} \dot{\lambda} = 0 \qquad \text{(Equation 2-17)}$$

From which

$$\dot{\lambda} = \frac{f_\sigma : D_e : \dot{\varepsilon}}{f_\sigma : D_e : f_\sigma + \overline{H_K} f_\sigma : f_\sigma} \qquad \text{(Equation 2-18)}$$

Later, Ziegler (1950)[87] proposed a modification of the Melan-Prager kinematic hardening rule. He found that if the original equation ($\dot{\sigma_b} = \overline{H_K}\dot{\varepsilon_p}$) is reduced to a subspace of the stress space (*e.g.* to the subspace corresponding to the plane stress), the yield surface does not always move in the direction of its normal at the current stress point.

Also he observed that the von Mises yield surface which followed by the Melan-Prager rule always moves in the direction of the vector connecting its center with the current stress point, and that this property holds in any subspace of the stress space. Therefore, he suggested a modified kinematic hardening law

$$\dot{\sigma_b} = \dot{\mu}(\sigma - \sigma_b) \qquad \text{(Equation 2-19)}$$

where $\dot{\mu}$ is a new multiplier. The consistency condition is

$$f_\sigma : \dot{\sigma} - f_\sigma : \dot{\sigma_b} = 0 \qquad \text{(Equation 2-20)}$$

After the usual substitution from the elastic stress-strain law, flow rule, and hardening law, there is only one equation with two unknowns, the plastic multiplier, $\dot{\lambda}$, and the multiplier from the hardening law, $\dot{\mu}$:

$$f_\sigma : D_e : \left(\dot{\varepsilon} - \dot{\lambda} f_\sigma\right) - \dot{\mu} f_\sigma : (\sigma - \sigma_b) = 0 \qquad \text{(Equation 2-21)}$$

The relationship between the stress rate and plastic strain rate remains unspecified. The supplementary condition,

$$\dot{\sigma} : f_\sigma = \overline{H_K} \dot{\varepsilon_p} : f_\sigma \qquad \text{(Equation 2-22)}$$

where $\overline{H_K}$ has the same meaning as in the Melan-Prager hardening rule.

Again, using the elastic stress-strain law and the flow rate, we obtain an equation with a single unknown,

$$f_\sigma : D_e : \left(\dot{\varepsilon} - \dot{\lambda} f_\sigma\right) = \overline{H_K} \dot{\varepsilon_p} : f_\sigma \qquad \text{(Equation 2-23)}$$

$$\dot{\lambda} = \frac{f_\sigma : D_e : \dot{\varepsilon}}{f_\sigma : D_e : f_\sigma + \overline{H_K} f_\sigma : f_\sigma} \qquad \text{(Equation 2-24)}$$

$$\dot{\mu} = \overline{H_K} \frac{f_\sigma : f_\sigma}{f_\sigma : (\sigma - \sigma_b) f_\sigma} \frac{f_\sigma : D_e : \dot{\varepsilon}}{f_\sigma : D_e : f_\sigma + \overline{H_K} f_\sigma : f_\sigma} \qquad \text{(Equation 2-25)}$$

Thus, for a prescribed strain rate, the rate of the back stress can be known.

2.5.3.2 **Nonlinear kinematic hardening**

In reality, modeling of engineering materials often requires nonlinear hardening laws. Armstrong and Frederick (1966)[88] have proposed a nonlinear kinematic hardening law by introducing a recovery term, which is proportional to the current back stress multiplied by the norm of the plastic strain rate, into the linear Melan-Prager rule. According to the Armstrong-Frederick rule, the evolution of the back stress is governed by the different equation

$$\dot{\sigma_b} = \bar{H}_K \dot{\varepsilon_p} - \gamma \sqrt{\frac{2}{3}} \|\dot{\varepsilon_p}\| \sigma_b \qquad \text{(Equation 2-26)}$$

where $\bar{H}_K$ and γ are constant material parameters. From the Figure 38(a), the back stress is still zero and gives the same response as the linear hardening law at the onset of yielding. As the back stress develops, the additional term becomes activated which slows down the rate at which the back stress grows, as long as the loading remains monotonic. Upon a load reversal, the back stress and its rate have opposite directions (in the sense that their scalar product is negative) and the additional term increases the plastic modulus.

For symmetric stress cycles, the response immediately stabilizers and the strain history becomes periodic. However, for stress cycles oscillating around a nonzero mean value, the net increment of plastic strain over one cycle is not zero (see Figure 38(c)). This phenomenon is called ratcheting [89].

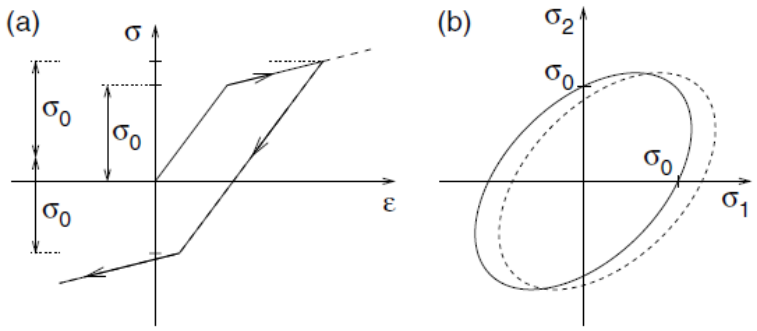

Figure 37. Kinematic hardening: a) uniaxial stress-strain diagram, b) evolution of the yield surface in the biaxial stress plane.[89]

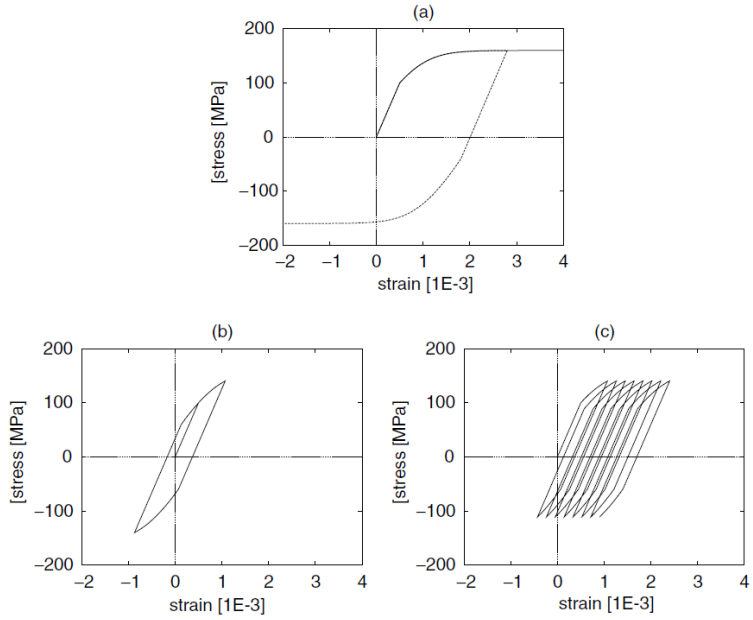

Figure 38. Stress-strain diagrams for a model with Armstrong-Frederick kinematic hardening: (a) Monotonic loading and load reversal, (b) cyclic loading with a zero mean stress, (c) cyclic loading with a positive mean stress. [89]

2.6 **Research Objectives**

Based on the literature it is evident that effort has been made into understanding the effect of strain path change through the study of plastic anisotropy, which originates from different sources at different length scales including shear bands,

grain orientation, and dislocation cells. However, since aluminum alloys generally exhibit smaller strain path change effects, previous research on strain path change in aluminum alloys is limited.

In this project, the effect of strain path change on AA3104 is studied using a non-proportional test sequence, which is achieved by a two-stage tensile test. The effects of pre-strains and strain path change angle are studied to determine how they affect the mechanical properties.

This is primary done through a two-stage tensile test, a plane strain tensile test and subsequent uniaxial tensile test at various strain path change angles, with Digital Image Correlation (DIC) to track the strain evolution during the test. Images are recorded during the tests using a digital camera (DSLR) and an optical microscope.

3 Experimental procedures

3.1 Choice of material

AA3104 aluminum alloy was chosen for this thesis because strain path change effects are pronounced in this alloy. The material was provided by Novelis Inc. This material was received as a 280 microns thick sheet.

The 3XXX series aluminum alloys are manganese based alloys, which are mainly used in can-packaging, such as deep draw cans and craned cans for fruit juices and fish products [90].

3.2 Sample preparation

3.2.1 Design and machining of specimen

- Plane strain tensile coupons

The proposed plane strain sample geometry is shown in Figure 39. The sample is 35mm long and 21mm wide at the ends of the sample. The gauge is 1mm long and 20mm wide. The sample, which is designed to have a large ratio of gauge width and length, is to be in the plane strain state in the center for some curtained pre-strained percentage. A large area for the grip sections was designed so that they can fit in the grips of tensile machines and prevent the specimen from slipping during the test.

- Uniaxial tensile coupons

The uniaxial tensile specimen geometry is shown in Figure 40. The sample is 16mm long and 2.9 mm wide at the ends of the sample. The gage is 1 mm long and

0.8 mm wide at the thinnest section (located at the center of the sample which contains a notch). The notch was employed to ensure that failure takes place at the center of the specimen. The long grip sections are used to fit within the grips of the tensile machine.

- Tensile coupons after pre-strain

After being pre-strained, the uniaxial tensile coupons were cut from the center of the plane strain specimen at 0^o, 45^o and 90^o to the pre-strain direction (see Figure 41). The tensile coupon has the same dimensions as the uniaxial tensile coupon.

The sample was machined via EDM (Electric discharge machining) (see Figure 42 and Figure 43) in the Mechanical Engineering machine shop at the University of Ottawa.

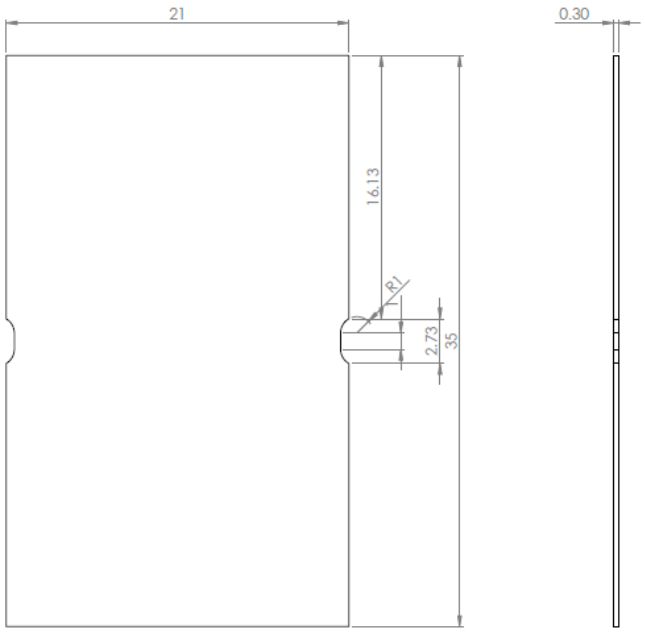

Figure 39. The drawing of the plane strain tensile specimen.

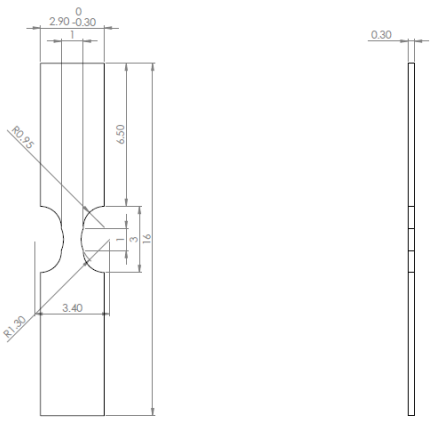

Figure 40. The drawing of the uniaxial tensile specimen.

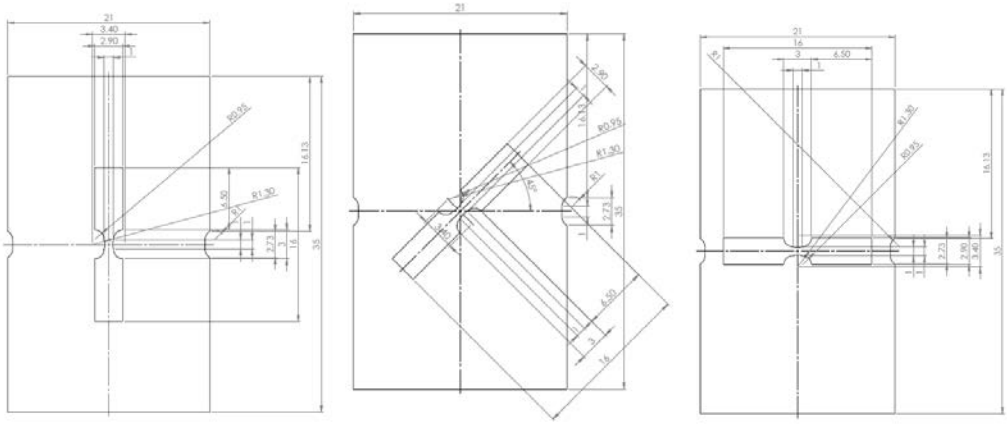

Figure 41. The drawing of the uniaxial tensile specimen which is (a) 0°, (b) 45° and (c) 90° to the pre-strained direction after pre-strained.

Figure 42. EDM (Electric discharge machining) at the Mechanical machine shop in the University of Ottawa.

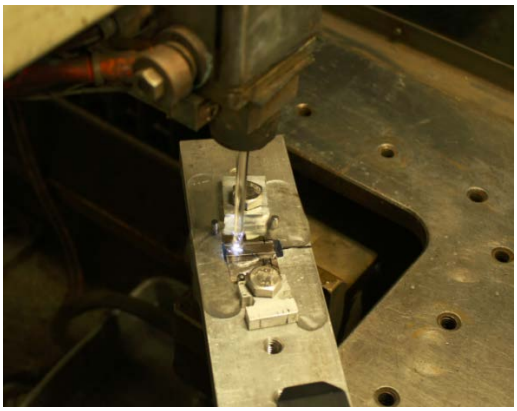

Figure 43. EDM (Electric discharge machining) cutting the tensile coupon from the pre-strained specimen which is 45° to the pre-strained direction.

3.2.2 **Heat treatment**

In order to better visualize inhomogeneities during deformation between and within grains, samples were annealed to obtain a large grain size before testing.

The specimens were annealed in an air furnace (see Figure 44) at 625°C for 2h, and the average grain size reached 35 μm (see Figure 45). The grain shape was found to be equiaxed and the heat treatment was sufficient to produce a complete recovery of the materials.

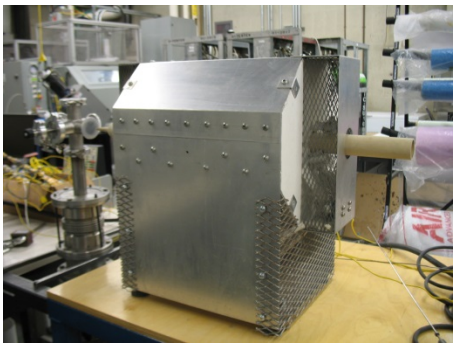

Figure 44. The furnace set-up used in this project.

Figure 45. Optical micrograph of the cross section of a specimen annealed at 625°C for 2 hours.

Electro-etching was employed to reveal the grain size of the specimen (see Figure 45). The method of electro-etching is shown in Table 6 and the set-up of electro-etching is shown in Figure 46.

Table 6. Electro-etching approach for AA 3104.

Sample	Solution	Anode (+)	Cathode (-)	Voltage	Time
AA 3104	5% HBF4 +wash by water	Specimen	Stainless Steel	30V	2-3 min

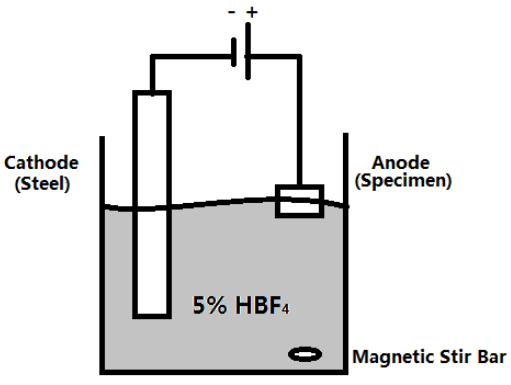

Figure 46. The set-up of electro-etching.

3.2.3 **Grinding and polishing**

Samples were polished in order to remove machining effects and oxidation from the annealing process. Also, in order to obtain randomly distributed speckles by electrodepositon (see section 3.3.1) for subsequent digital image correlation analysis, a mirror surface finish was required. Table 7 shows the polishing procedure to obtain the mirror finish, and Figure 47 and Figure 48 are the polishing apparatus used in this project.

Table 7. Summary of the polishing procedures.

Type of Cloth	**Grit size/polishing suspension**	**Lubricant**	**Time**
SiC paper	P2400	Water	Until the oxide deposition and machining texture are remove
	P4000	Water	3-4 minutes
MD-Mol cloth	3 micron diamond paste	Propylene glycol solution	2-3 minutes
MD-Nap cloth	1 micron diamond paste	Propylene glycol solution	2-3 minutes
MD-Chem cloth	Alumina 0.05 micron	Water	4 minutes
Vibratory polisher	Colloidal silica suspension	Water	8 hours

Figure 47. The Buehler Metaserv 2000 polishing apparatus used in this project

Figure 48. Buehler Vibromet 2 vibratory polisher

3.3 **Mechanical tests**

Prior to conducting the tensile tests, digital image correlation patterns need to be produced on the surface of the specimen in order to follow strain evolution during testing.

3.3.1 **Sample preparation for Digital Image Correlation**

Digital image correlation (DIC) is a computer-based process to obtain two-dimentional full field displacement informtaion by recording and tracking the motion of a speckle pattern deposited on the specimen surface during deformation of a body [91]–[93]. In other to track the displacement of all the points on the specimen surface, randon distributed speckle patterns should be produced on the surface. In this thesis, this technique was empoyed to study deformation inhomogeneities at the sample surface.

Two methods were employed in this project as follows.

- Airbrush technique

For the plane strain specimen, macroscale patterns were deposited using an Iwata airbrush (see Figure 49), which produced a black background with white speckles, having a speckle size of about 0.01 mm to 0.08 mm (see Figure 50 for a picture of a plane strain specimen with airbrush pattern).

Figure 49. Picture of Iwata airbrush used in this project.

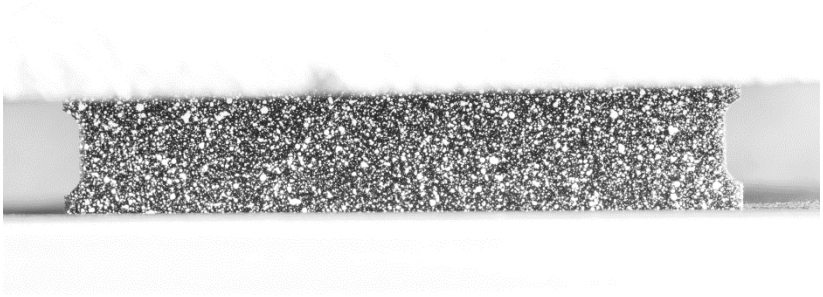

Figure 50. The plane strain specimen with airbrushed patterns.

- Electrodeposition

A random speckle pattern can be creatd by electrodeposition to obtain finer features. A copper rod was used as the anode while the sample was the cathode. A piece of Al sheet was used at the back of the sample, which helped produce a uniform pattern, especially in the gauge length. Copper sulfate ($CuSO_4$), 44g/L (Fisher Scientific), with 300ppm Poly ethylene glycol (PEG), was employed as the electrolyte.

Magnetic stirring was used to make the solution uniform. The power supply can deliver constant voltage in the range of 1 to 40 volts, which was necessary for electro-deposition. A pulsed electrodepositon technique was used as it produced finer feature distributed homogeneously compared to what would be obtained using continuous deposition. An oscilloscope was used to measure the pulse time and voltage, to make sure that the deposition is taking place under constant parameters. The relay to generate the pulse was manufactured by the Mechanical Engineering Department Workshop at the University of Ottawa. It is a switch controlled by a computer. It is able to deliver pulses that are 1ms in length short with an accuracy of about 0.2 ms. The setup allows a controlled change in voltage, pulse time, and number of pulses. It also provides means to measure and collect the data. This setup can increase the consistency and accuracy of the results.

Electrodeposition of copper particles occurs in three stages: particle nucleation, growth, and coalescence. The current density (voltage) is crucial to control the density of nucleation sites. Pulse electrodeposition is commonly employed to create nano-grained materials. By using pulses of current the circuit can control the growth of the particles. Also, due to the sensitivity of electrodeposition to changes in current distribution on the sample surface; scratch-free and clean surfaces can help develop randomly distributed patterns suitable for DIC.

According to Emekli et al. [94], by employing PEG in the copper sulfate electrolyte, an increase in the nuclei density can be observed, as well as a decrease in

particle size. The PEG, which acts as a suppressor, has a significant effect on the nucleation rate by increasing the overpotential, and impedes the growth of particles on the surface.

An interesting result was shown when the grains were revealed. After being polished in a vibratory polisher in a 0.05 micron alumina solution containing Copper ions for 8 hours, the deposition was preferential on certain grain orientations. As shown in Figure 52, some grains have higher copper deposit densities than others.

The procedure we settled upon was an applied voltage of 40V with an on-time of 1 ms and an off-time of 200 ms. The deposition had 70 pulses for uniaxial tensile specimens (see Figure 53), while 400 pulses for plane strain specimens were required due to the larger sample size. The size of the features ranged from 1 micron to 6 microns.

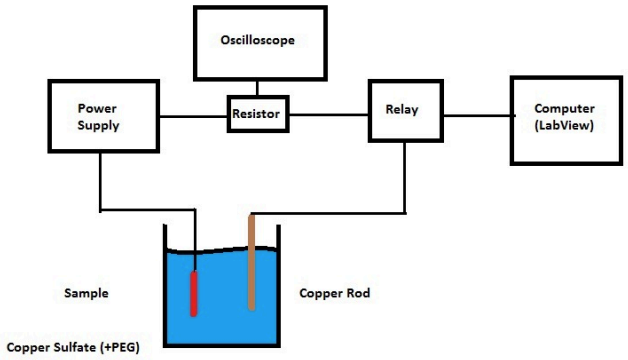

Figure 51. Electrodeposition set-up which is employed in this project.

Figure 52. Optical micrograph of aluminum showing preferential deposition of copper depending on the grain orientations.

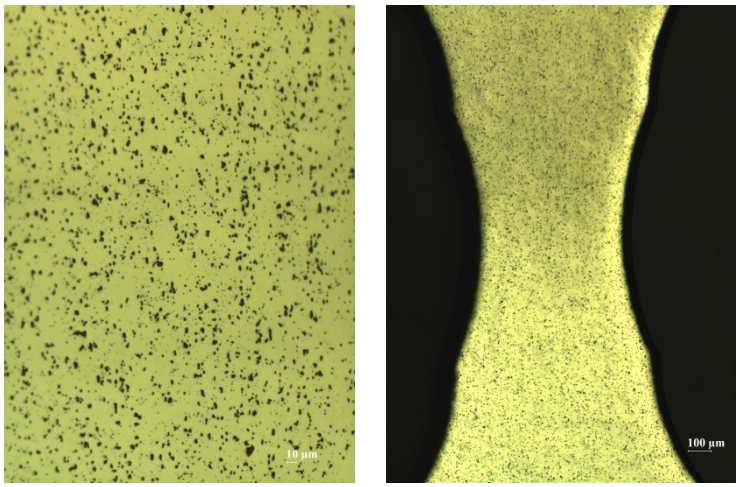

(a) (b)

Figure 53. Copper deposits on polished aluminum uniaxial tensile specimen via pulsed electrodeposition with the magnification is (a) 5X and (b) 20X magnification from which the patterns were in 40V, 1ms/200ms (ontime/offtime) and 70 pulses.

3.3.2 **Tensile test**

Plane strain and uniaxial tension was carried out for the first set of experiments, which was done to investigate whether different strain paths resulted in different local strain distributions in the sample. The second set of experiment, which was

non-proportional loading, was carried out to observe the strain path change effect. After the first deformation was applied in plane strain to various pre-strains, a subsequent deformation at 0^o, 45^o, and 90^o to the pre-strain axis was carried out in uniaxial tension up to failure.

- Plane strain tensile test

Since the closed plane strain tension can only be achieved in a sheet specimen with a very wide and short gauge section [95], it is difficult to prevent the sample from sliding or from failing in the gripping area [96]. According to Holmberg et al.[95], larger grip area can provide sufficient area for clamping to avoid fracture outside the plane strain region. The plane strain tensile grips (see Figure 54) were designed to have larger gripping area according to the dimension of the tensile machine. Also, in order to prevent the specimen from sliding, teeth were machined on the inside surface of the grips. The plane strain grips were machined by the Mechanical Engineering machine shop at the University of Ottawa (see Figure 54 and Figure 55).

The tensile machine used is shown in Figure 55 and Figure 56, and it is controlled by a MATLAB-based GUI. For the plane strain tensile tests, the tensile machine is placed under a Canon DSLR (digital single-length reflex) camera at the macroscale (see Figure 57), and a Nikon Optiphot 100 microscope with a 20X ULWD (ultra-long working distance) objective, connected to a PixeLINK camera (see Figure 58), which was employed to record the test at the microscale. The load cell used was 1000 lbs.

The strain rate used was around $0.001s^{-1}$. The DSLR camera with DSLR Remote Pro software took pictures of the sample every 2 seconds (maximum speed available), while the PixeLINK, Capture OEM software recorded snapshots every 0.5 seconds.

- Uniaxial tensile test

The uniaxial tensile test was carried out in the same tensile machine as the plane strain tensile test using the uniaxial tensile grips (see Figure 56). A 100 lbs load cell was used. The strain rate used was around $0.001s^{-1}$. A Nikon Optiphot 100 microscope was employed with a ULWD objective of 5X at the macroscle and 20X at the microscale. Images were recorded by the Pixelink camera every 0.5 seconds.

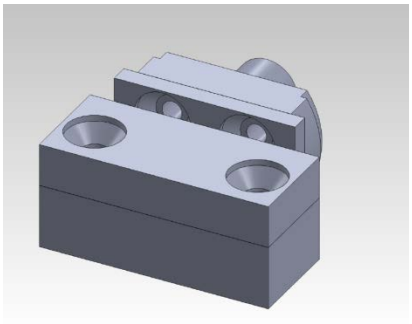

Figure 54. The design of the grips for plane strain tensile test

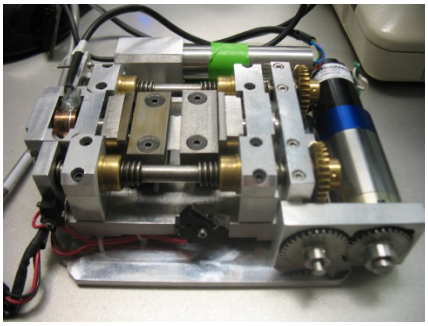

Figure 55. Picture of tensile machine with plane strain grips used in this project

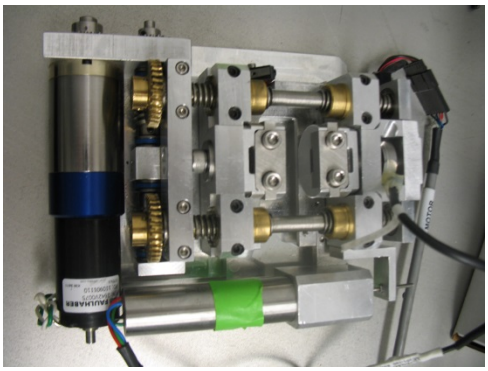

Figure 56. Picture of tensile machine with uniaxial tensile grips used in this project

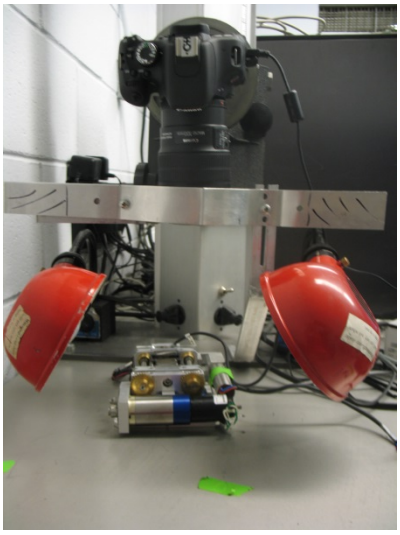

Figure 57. The set-up of the digital camera (DSLR) in this project.

Figure 58. Nikon Optiphot 100 microscope used during tensile tests

3.3.3 **Naming of specimens**

In order to better distinguish the specimen for the uniaxial tensile test, plane strain tensile tests, and the strain path change test, the specimen was named differently in this project.

For the uniaxial specimen, “TS_SX” was used. “TS” stands for tensile specimen, and “SX” is the test number. For example, “TS_S6” means the 6th tensile test specimen.

For the plane strain specimen, “PS_testXX” was used. “PS” means plane strain, and “testXX” is the test number. For example, “PS_test12” means the 12th specimen of the tensile test.

For the strain path change specimen, “PX1_X2_SX3” was used. “PX1” is the pre-strain, “X2” is the strain path angle, and “SX3” is the test number. For example, “P3_45_S2” means the second strain path change specimen at 45º with around 3% pre-strains.

3.4 **Digital Image Correlation analysis**

Digital image correlation (DIC) uses a digital CCD camera to capture the image during deformation and track the position of the same physical points shown in a reference image and a deformed image. To achieve this, a square subset of pixels is defined on the speckle pattern around a point of interest on a reference image and their corresponding location determined on the deformed image (see Figure 59). The maximum correlation in each window is related the displacement of the patterns, and

this gives the vector length and direction for each window.

Davis 8.1 software was employed in this project. Using the strain module in the program, images can be selected for strain analysis. In terms of software parameters, 3 seeding points, which are the points where the deformation calculations initiate, were chosen with one close to the center of the specimen. The subset size and step size are shown in Table 8, which is related with the speckle size and speckle density.

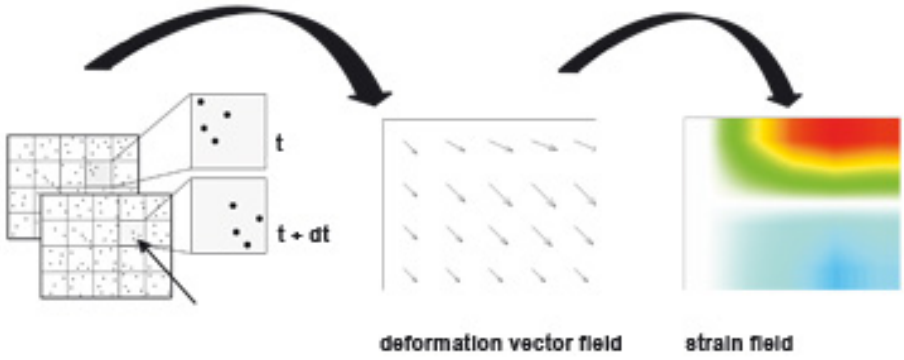

Figure 59. Digital Image correlation processes; strain evaluation (Image is taken from La Vision company website)

Table 8. The subset size and step size used in this project.

Test	Patterns	Subset size (pixels)	Step size (pixels)
Uniaxial tensile test	Electrodeposition (see Figure 53(b))	101	25
Plane strain tensile test	Airbrush (see Figure 50)	121	30

3.5 **Fracture surface analysis**

Fracture surface analysis in a Scanning Electron Microscope (SEM) was carried out to determine the final true strains at fracture (ductility) for 3104 aluminum alloy tensile specimens. For this purpose the JEOL JSM-5300 Scanning Electron Microscope (SEM) was utilized at a working voltage of 20 keV (see Figure 60).

Figure 60. JEOL JSM-5300 Scanning Electron Microscope (SEM); Resolution: 10-20 nm, Magnification: high vacuum mode 15x-200,000x and low vacuum mode 15x-50,000x, Acceleration voltage: 0.5-30 kV, Specimen size: up to 76 mm in diameter.

3.6 **Error bars**

For reproducibility purposes, multiple specimens were tested in each condition. The distribution of data values is represented by the mean values, and the overall distribution of the data is represented by the error bars.

To statistically describe uncertainty in the measurements, the standard error, the standard deviation of mean values, will be used. The standard error is calculated by dividing the standard deviation by the square root of the number of measurements that make up the mean (often represented by N). And then, the standard error are used to represent both the positive (+) and negative (-) values of error bars.

3.7 Extracting the true stress strain curve from DIC

At the macroscale, the strain distribution on the whole gauge length is analyzed by DIC. The Bridgman correction is used to correct for the higher stress triaxialitites found in the middle of the sample due to the notch introduced in the sample by machining. The true stress strain curve can then be obtained from these results as detailed below.

The stress-strain curve obtained during testing is the engineering stress vs. far field engineering strain curve. Using DIC, the average true strain in the analyzed area vs. the number of images can be extracted.

When plotting displacement vs. time during the tensile test, one can observe an initial plateau followed by a linear part followed by a nonlinear behavior close to the end of the test as seen in Figure 61. The initial plateau is due to the alignment of tensile machine and is discarded. The nonlinearity at the end of the test is due to the fact that the tensile machine cannot maintain a constant speed at high loads. The region of interest is the middle linear section.

The number of pictures n_{Linear} in the linear middle section can be found by using the following equation:

$$\frac{n_{Linear}}{n_{tension}} = \frac{t_{Linear}}{t_{tension}} \quad \text{(Equation 3-1)}$$

$$n_{Linear} = \frac{n_{tension} \times t_{Linear}}{t_{tension}} \quad \text{(Equation 3-2)}$$

where $n_{tension}$is the number of pictures during the tensile test, t_{Linear} is the time

when the time vs. displacement curve is in the middle linear section of the stress strain curve, and $t_{tension}$ is the total duration of the tensile test (see Figure 61).

The true strain in the tensile direction (ε_{yy}) and transverse direction (ε_{xx}) vs. the linear number of picture can be known from the strain analysis in the DaVis software. The area from which ε_{xx} and ε_{yy} were extracted is shown in Figure 62. One can then obtain the true strain in the thickness direction ε_{zz} assuming volume conservation as follows:

$$\varepsilon_{zz} = -(\varepsilon_{yy} + \varepsilon_{xx}) \quad \text{(Equation 3-3)}$$

The current sample thickness can then be obtained as follows:

$$L = L_0 * \exp(\varepsilon_{xx}) \quad \text{(Equation 3-4)}$$

$$t = t_0 * \exp(\varepsilon_{zz}) \quad \text{(Equation 3-5)}$$

where L_0 is the initial gauge width, L is the instantaneous gauge width, t_0 is the initial thickness of the specimen, and t is the instantaneous thickness of the specimen (see Figure 63).

The instantaneous area of the specimen *A* can be obtained:

$$A = Lt \quad \text{(Equation 3-6)}$$

$$A_0 = L_0 t_0 \quad \text{(Equation 3-7)}$$

where A is the current cross-sectional area and A_0 is the initial cross-sectional area.

Then, the displacement per picture (D_{pic}) can be found

$$D_{pic} = n_{pic} \times \frac{D_{Linear\ total}}{n_{Linear}} \quad \text{(Equation 3-8)}$$

where n_{pic} is the picture number, n_{Linear} is the total number of pictures in the linear

part of the test, and $D_{Linear\ total}$ is the total displacement in the linear part of the test.

When comparing D_{pic} with D_{Linear}(the original displacement in the linear part), similar values can be found, which in turn gives the corresponding load (P_{corrs}). The true stress can be easily known from

$$\sigma_{True} = \frac{P_{corrs}}{A} \qquad \text{(Equation 3-9)}$$

The true strain (ε_{True}) is equal to the strain in the tensile direction from the DIC analysis ε_{yy}.

The true strain (ε_{True}) and true stress (σ_{True}) curve can then be obtained.

Since there is a reduction in the cross sectional area for the uniaxial tensile specimens (see Figure 40), the stress distribution is not uniform. In order to correct for the higher stress triaxialitites found in the middle of the sample, Bridgman (1952) proposed the following equation:

$$\sigma_{corrected} = \sigma_{measured}\left[\left(1+\frac{2R}{a}\right)\ln(1+\frac{a}{2R})\right]^{-1} \qquad \text{(Equation 3-10)}$$

where *R* is the radius of the external neck and *a* is the minimum cross sectional radius of the sample (see Figure 64). The true stress strain curve after Bridgman correction is shown in Figure 65.

Using the software Origin, a curve can be fitted to the true strain (ε_{True}) and true stress (σ_{True}) curve to obtain the parameters of the Hollomon equations ($\sigma = K\varepsilon_p^n$ where σ is the stress, K is the stress index, ε_p is the plastic strain and n is the strain hardening exponent).

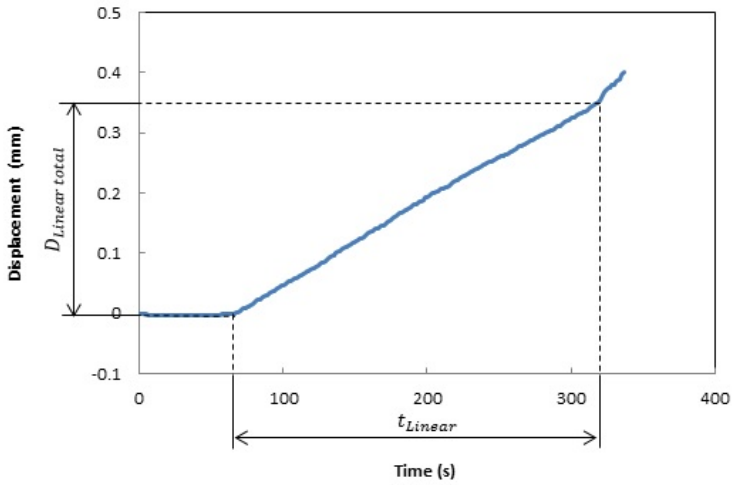

Figure 61. Time vs. displacement for uniaxial tension (P3_45_S2), which indicates $t_{tension}$ and $D_{Linear\ total}$.

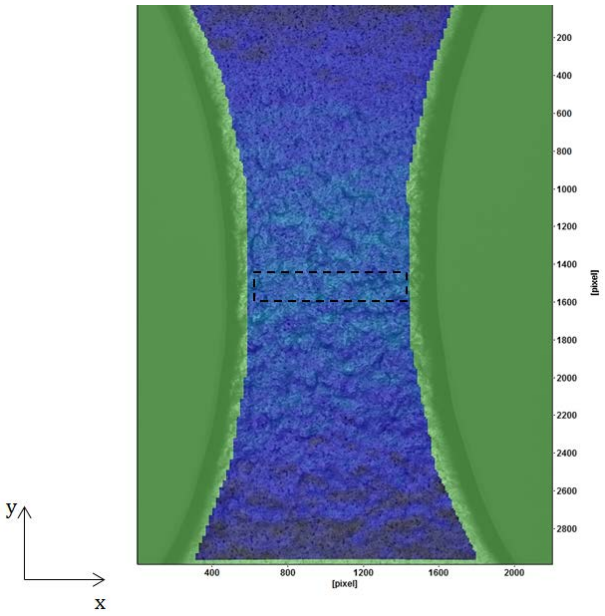

Figure 62. A schematic to show the area where ε_{xx} and ε_{yy} are extracted.

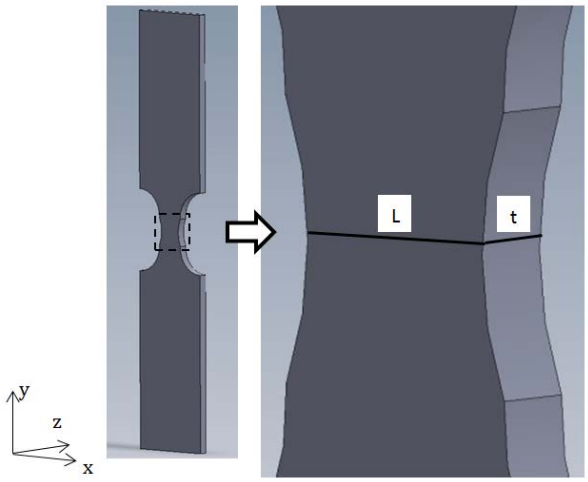

Figure 63. A schematic to show the gauge width L and the initial thickness of the specimen t.

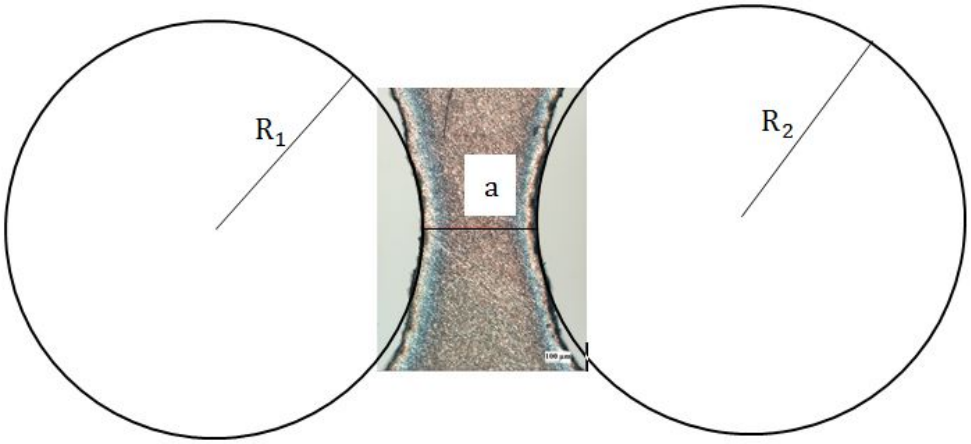

Figure 64. A schematic to show the measurement of the radius of the external neck (R) and the minimum cross sectional radius (a) of the sample for Bridgman correction.

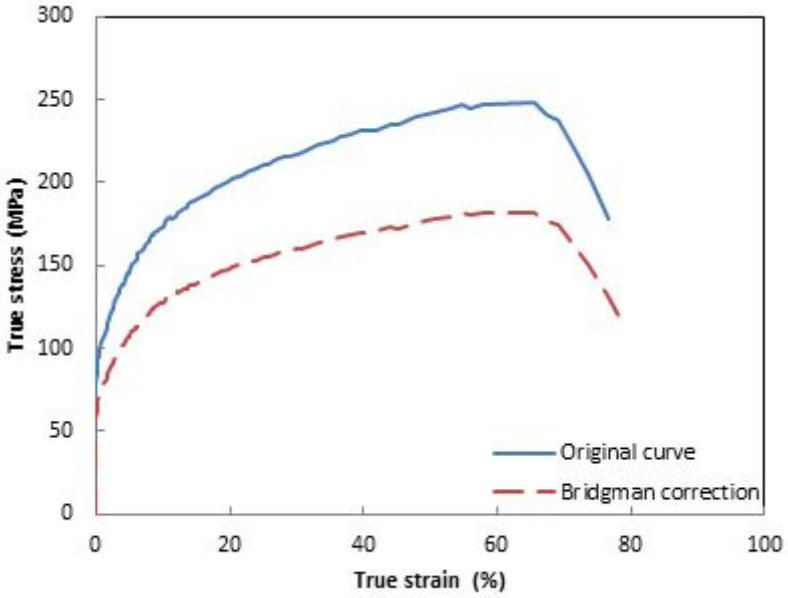

Figure 65. The true stress strain curve extracted from DIC and using the Bridgman correction (Equation 3-10) for the uniaxial tensile specimen (TS_S6).

4 Experimental Results

4.1 Introduction

This chapter mainly deals with detailing the results of experimental work, along with the relevant information.

The experimental results will first start with the true stress strain curve. In this section, the true stress strain curve based on DIC analysis for proportional loading and non-proportional loading will be presented. The yield stress, the work-hardening rate, ultimate tensile strength (UTS) and necking strain are then extracted from the true stress strain curve.

The strain distribution at the sample surface will then be presented and related to the stress strain curve results.

We will finish this section by extracting the final true strains from fracture surface images taken with the scanning electron microscope.

4.2 True stress strain curve

At the macroscale, the strain distribution on the whole gauge length is analyzed by DIC. The Bridgman correction is used to correct for the higher stress triaxialitites found in the middle of the sample due to the notch introduced in the sample by machining. The true stress strain curve can then be obtained from these results, followed by the yield stress, the work-hardening rate, ultimate tensile strength (UTS) and necking strain are then extracted from the true stress strain curve.

4.2.1 True stress strain curve for proportional loading

4.2.1.1 Uniaxial tension

Figure 66 shows the true stress strain curve of a uniaxial tensile test in the rolling direction. As shown in Figure 62, the strains in the tensile direction (ε_{xx}) and in the transverse direction (ε_{yy}) are extracted from the area where the specimen fails. One can see that the test is reproducible. The yield stress, UTS, and effective necking strain for the uniaxial tensile specimens are shown in Table 9.

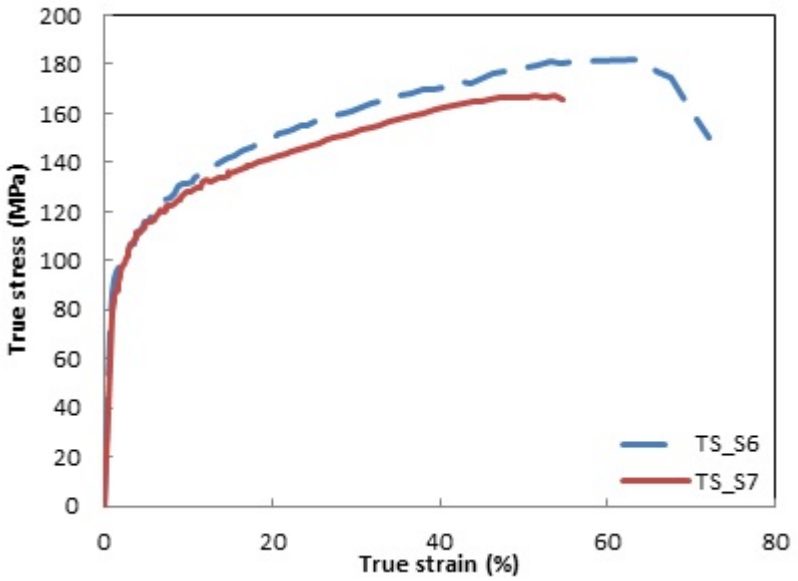

Figure 66. The true stress strain curve for the uniaxial tensile test.

Table 9. Yield stress, UTS and effective necking strain for uniaxial tensile specimen.

Specimen	Yield stress (MPa)	UTS (MPa)	Effective necking strain (%)
TS_S6	93.87082	152.3657	23.53966
TS_S7	84.84778	133.9561	20.3684

4.2.1.2 Plane strain

The true stress strain curve for the plane strain AA 3104 specimens is shown in Figure 67. One can see that there is some variation between different tests which is

probably due to some sample misalignment in the tensile machine. In Figure 68, the local strain is extracted from the center of the plane strain specimen from an area of about 1cm by 1 cm.

According to Wagoner et al. [97], a specimen can be considered under plane strain condition when $\left|\frac{\varepsilon_{Transverse}}{\varepsilon_{Rolling}}\right| < 10\%$. Table 10 shows the ratio $\left|\frac{\varepsilon_{Transverse}}{\varepsilon_{Rolling}}\right| < 10\%$ at different local strain levels, which verifies that our set-up and sample geometry is able to create a plane strain condition.

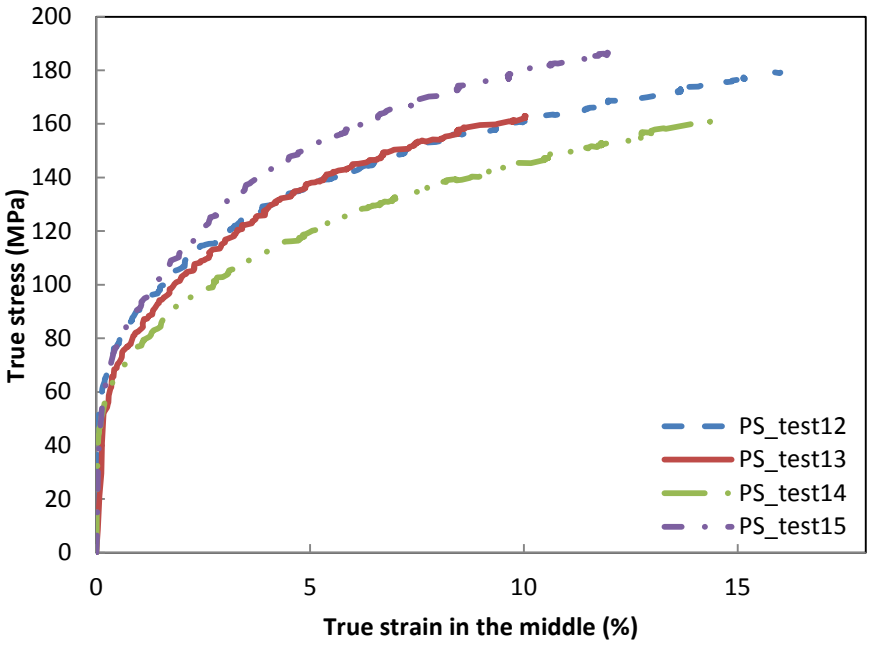

Figure 67. True stress strain curve for the plane strain tests

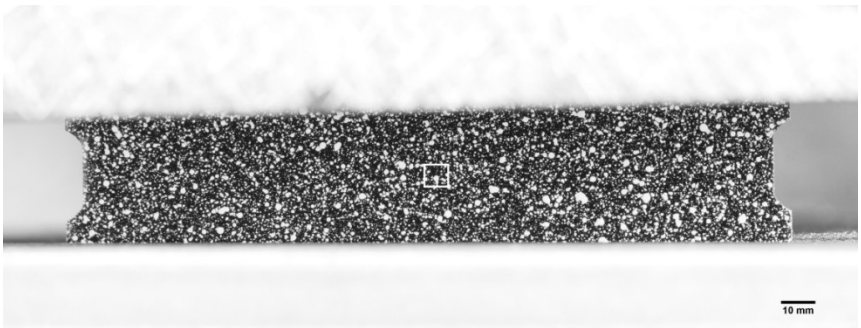

Figure 68. Location of the area used to extract the true local strain

Table 10. Evaluation of the plane strain condition at different local strain levels

Specimen	True yielding stress (MPa)	True UTS (MPa)	Effective true necking strain (%)	Strain (%)	Exx/Eyy (%)	Strain (%)	Exx/Eyy (%)	Strain (%)	Exx/Eyy (%)
PS_test12	79.12	164.48	7.99	3.00	-2.60	6.02	-2.31	9.08	-5.17
PS_test13	69.781	151.73	6.74	3.03	1.20	5.99	-1.10	9.11	-2.59
PS_test14	79.87	169.23	10.74	3.00	-0.89	5.92	-3.82	8.96	-5.08
PS_test15	67.49	176.67	8.89	3.07	-0.03	6.02	-1.11	8.97	-2.40

4.2.1.3 Comparison between uniaxial tensile test and plane strain tensile test

Figure 69 shows the true stress strain curve of uniaxial tensile test (TS_S6) and the plane strain test (PS_test12). One can see that the uniaxial specimen has a lower yield stress and higher elongation than that of plane strain specimen.

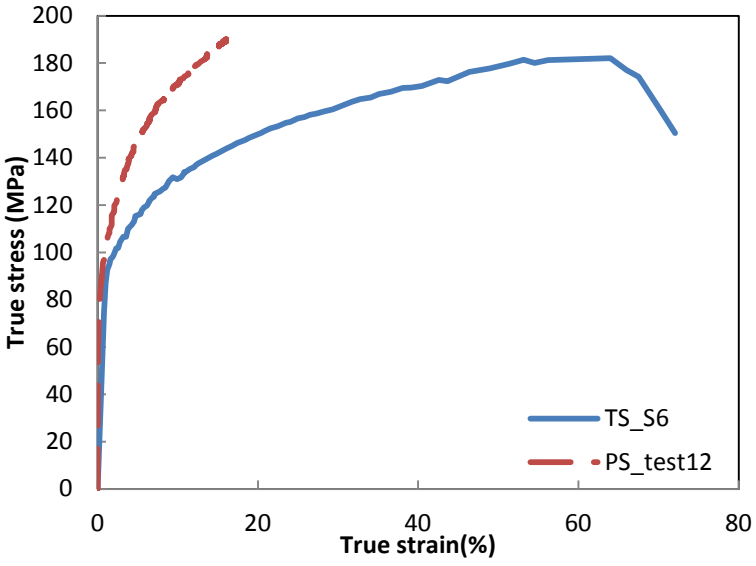

Figure 69. The true stress strain curve of uniaxial tension (TS_S6) and plane strain tension (PS_test12).

4.2.2 Pre-strained samples

4.2.2.1 True stress strain curves after strain path change

4.2.2.1.1 Effect of pre-strain on true stress strain curves

The plane strain specimens were pre-strained at around 3%, 6% and 9% in the RD direction, which was followed by uniaxial tension at 0°, 45°, and 90° to the pre-strain direction. The true stress strain curve which is based on the DIC analysis is presented in Figure 70. The true stress strain curve for all strain path change tests are shown in Appendix B.

From Figure 70 (a), (c) and (e), one can see the stress strain curves are fairly similar at the early stages of reloading, but differ significantly when necking and fracture take place. This is because it is hard for the DaVis software to track features on the sample surface at high strains and due to the sample going out of focus at high strains. In all cases, the flow stress after strain path change is higher than the one without pre-strains. Figure 70 (b), (d) and (f) also show that the reloading yield stress is lower than the unloading stress.

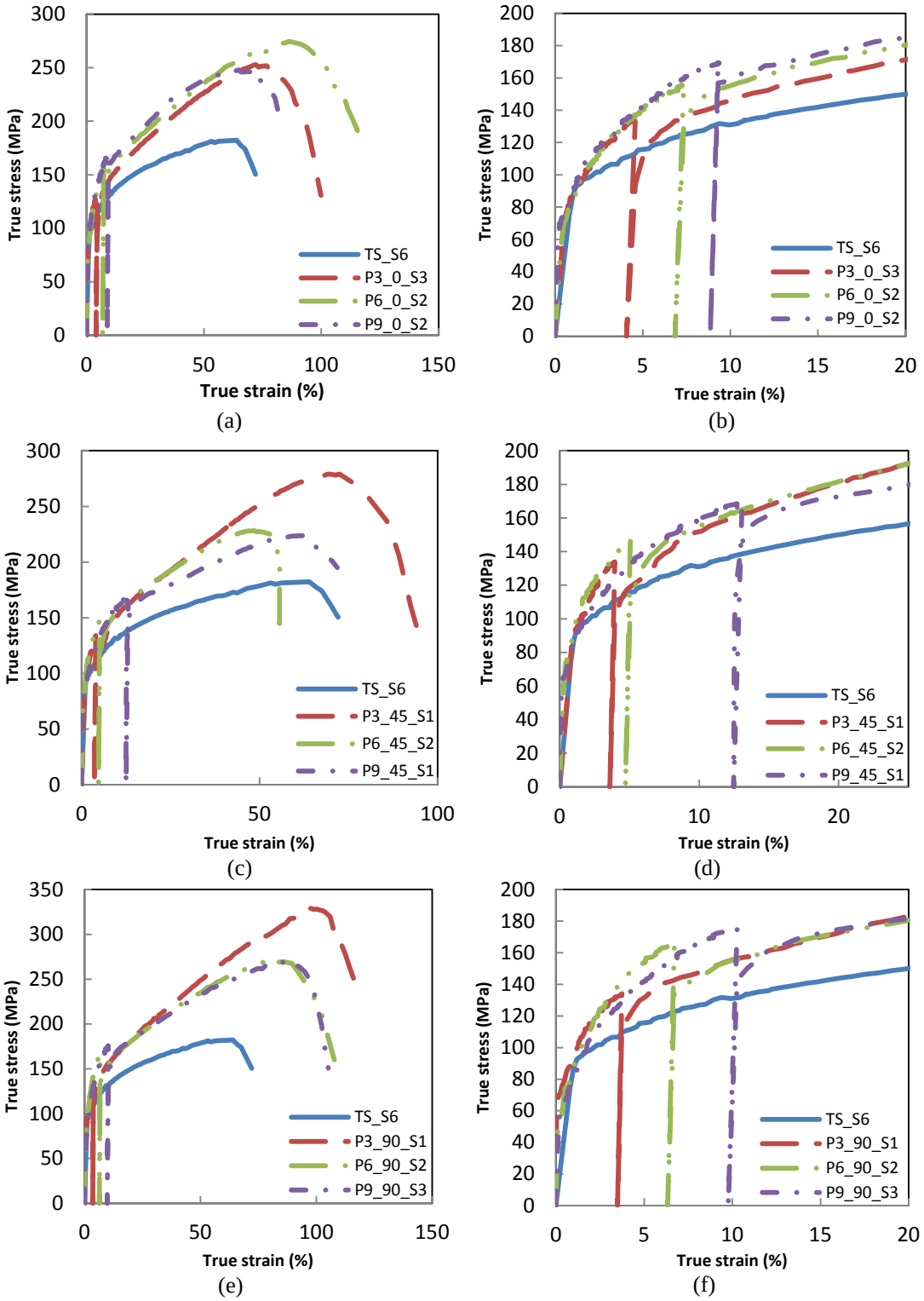

Figure 70. The reloading true stress strain curve at various pre-strains in (a), (b) 0°; (c), (d) 45°; and (e), (f) 90° to RD directions. (b), (d) and (f) are cropped from the true stress strain curve of (a), (c) and (e).

4.2.2.1.2 Effect of strain path change angle on true stress strain curve

The plane strain specimens were pre-strained to around 3%, 6% and 9% in the RD direction, which was followed by uniaxial tension at 0°, 45°, and 90° to the pre-strain directions. The true stress strain curve which is based on the DIC analysis is shown in Figure 71.

From Figure 71 (b), (d) and (f), the reloading yield stress at 0°, 45° and 90° are similar at a given pre-strain. From Figure 71 (a), (c) and (e), the flow stress after yielding is similar for three strain path change angles with similar pre-strains at around 3% and 6% (see Figure 71 (a) and (c)), while it is different at around 9% pre-strains (see Figure 71 (e)).

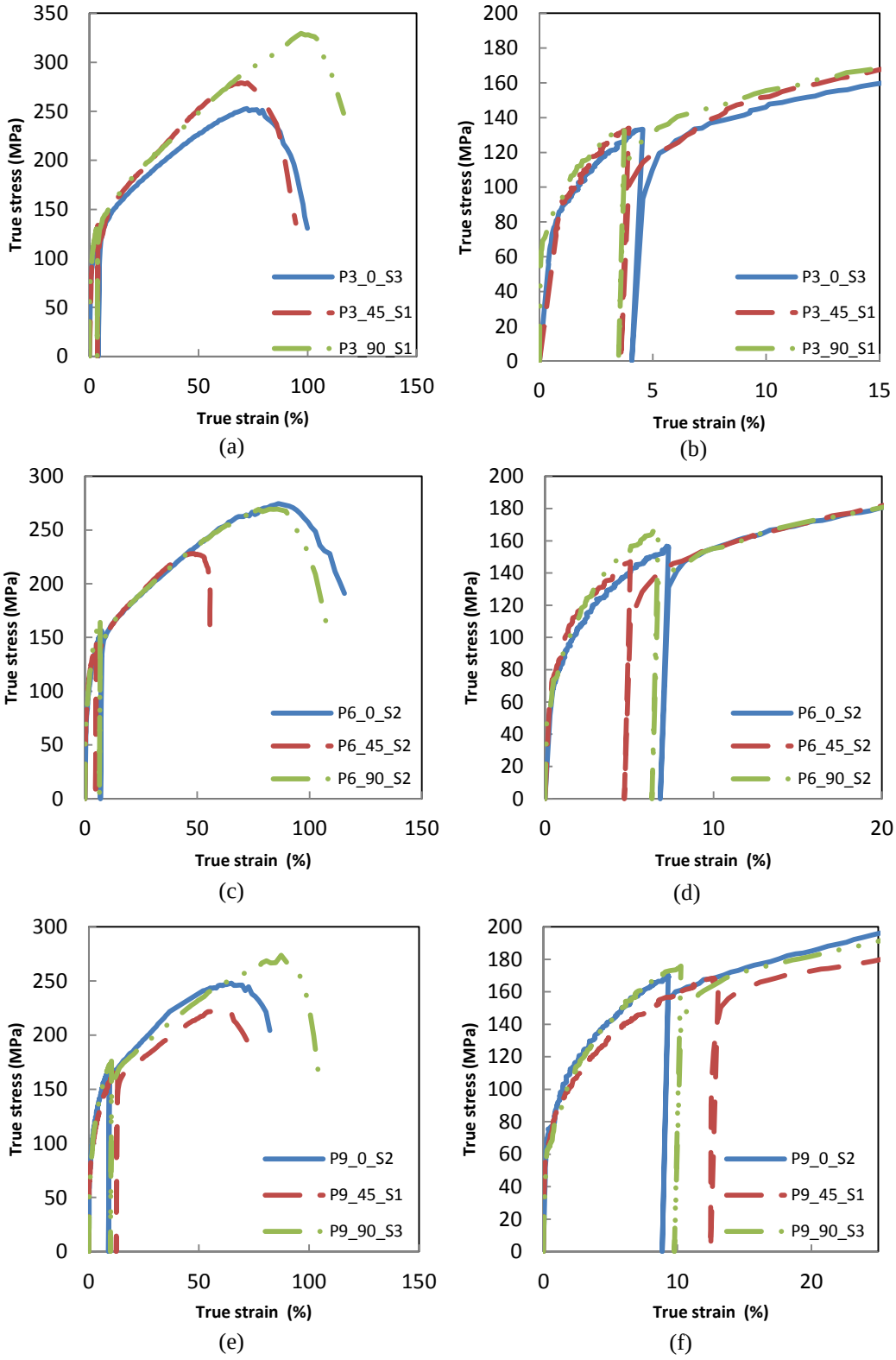

Figure 71. Plot of true stress strain curve after loading in 0°, 45°, and 90° to the pre-strain tensile direction (RD direction) for the pre-strain amount around (a), (b) 3%; (c), (d) 6%; and (e), (f) 9%. (b), (d) and (f) are cropped from the true stress strain curve of (a), (c) and (e).

4.2.3 **Reloading yield stress**

In this section, reloading yield stress after the strain path change will be analyzed. It will be compared to the various pre-strains and various strain path change angles.

The definition of the reloading yield stress σ_{be}, unloading stress σ_{un} and reference stress σ_r are shown in Figure 72. The yield stress is conventionally defined as the flow stress at 0.2% plastic strain.

In order to understand the differences in flow stress between the various pre-strains stage (plane strain tension and subsequent uniaxial deformation after the pre-strain), the reloading yield stress divided by the unloading stress (σ_{be}/σ_{un}) are calculated.

Also, to understand the differences in the stress-strain behaviors between the monotonic deformation without pre-strain stage and the subsequent deformation after strain path change, a normalized reloading stress (σ_{be}/σ_r) is measured. As shown in Figure 72, a reference curve is defined as the stress-strain curve obtained from uniaxial tension without pre-strain, and a reference stress σ_r is estimated as the stress value in the reference curve (uniaxial tensile specimen) which is equal to the amount of pre-strain ε_p. A macroscopic reloading yield stress σ_{be} is measured at 0.2% plastic strain off-set after reloading (ε_{be}).

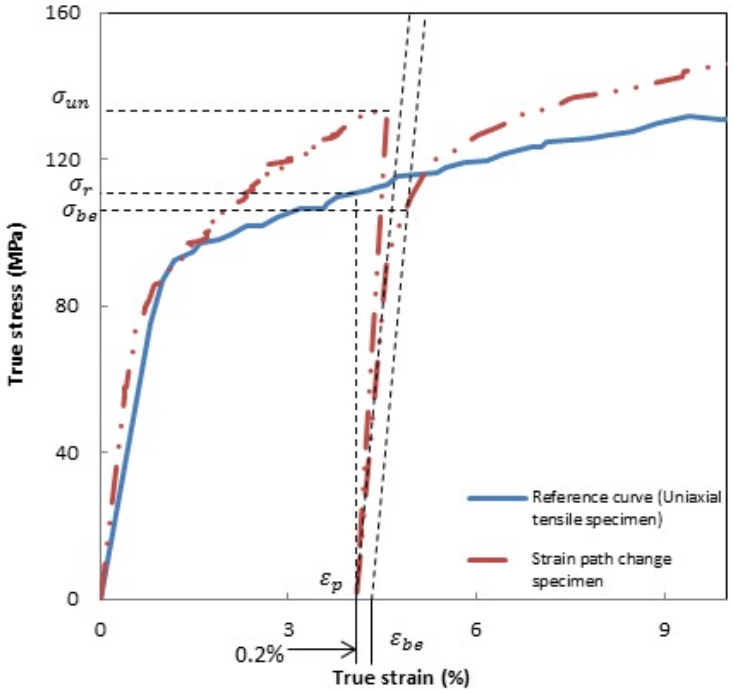

Figure 72. The definition of the reloading yield stress (σ_{be}), reloading yielding strain (ε_{be}), unloading stress (σ_{un}), reference stress (σ_r), and pre-strain (ε_p).

4.2.3.1 **Effect of pre-strain on reloading yield stress**

The average reloading true yield stresses at different average pre-strains are shown in Figure 73 for the various strain path angles of 0°, 45° and 90°. For reproducibility, each condition was tested at least two to three times. As shown in Figure 73, with increasing pre-strain, the average reloading yield stress increases.

Figure 74 shows the average reloading yield stress divided by the unloaded stress (σ_{be}/σ_{un}). In Figure 74, all values are smaller than 1, which means that reloading yield stress after strain path change is lower than the unloading stress. At 45° and 90°, the average reloading yield stress divided by unloading stress decreases with increasing pre-strain. However, at 0°, the value increases with increasing pre-strain at

lower pre-strain, followed by a decrease at higher pre-strain.

In Figure 75, a normalized reloading stress ($^{\sigma_{be}}/_{\sigma_r}$) with pre-strain at strain path change angles of 0°, 45° and 90° are plotted. Most of values are higher than 1 which means that the yield stress after pre-strain is higher than the yield stress that would be obtained without pre-strain. As shown in Figure 75, at 0° and 90°, the trends are similar with a peak at around 6% pre-strain. At 45° a decrease trend can be observed with increasing pre-strain.

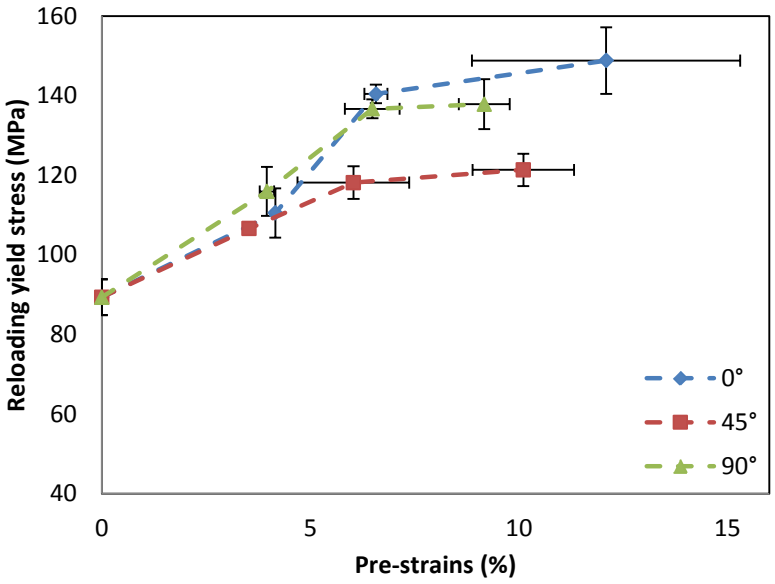

Figure 73. Average reloading yield stress at different average pre-strains for different strain path change angle (0°, 45° and 90°).

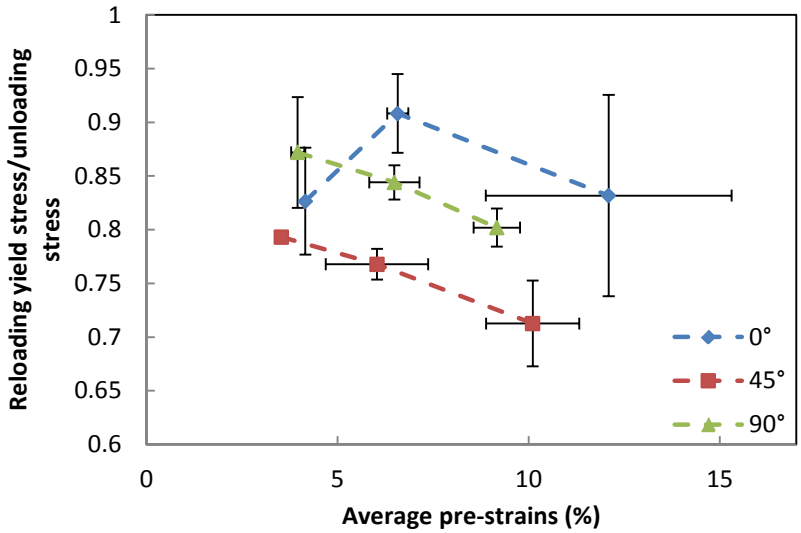

Figure 74. Average reloading yield stress /unloading stress at different average pre-strains for different strain path change angle (0°, 45° and 90°).

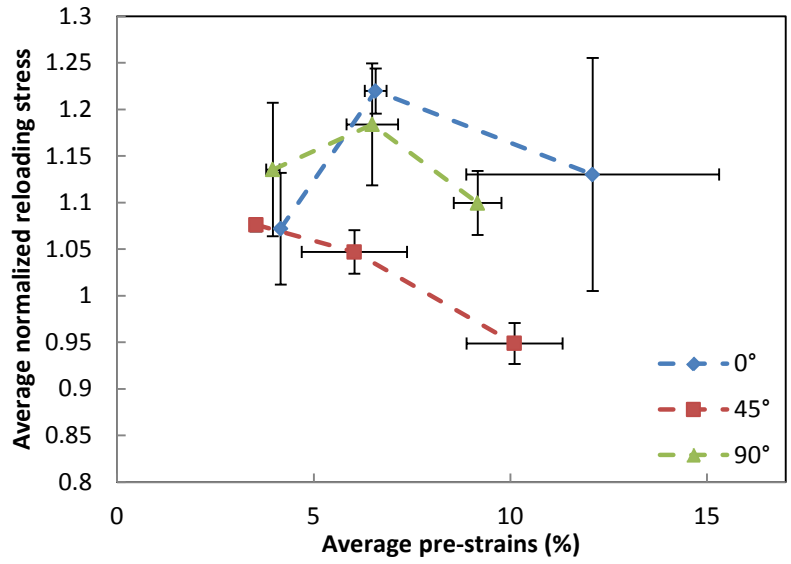

Figure 75. Evolution of the average normalized reloading stress $^{\sigma_{be}}/_{\sigma_r}$ at different average pre-strains for different strain path change angle (0°, 45° and 90°).

4.2.3.2 Effect of strain path change angle on reloading yielding stress

Figure 76 presents the average true yield stress measured in uniaxial tension after

strain path change at 0°, 45° and 90° to the RD for approximately 3%, 6% and 9% pre-strain. At 3% pre-strain, similar values are observed at three strain path change angles. At 6% and 9% pre-strain, similar trends are observed with the smallest one sitting at 45°. In order to compare the reloading yield stress at 45° and 90° to the one along the RD, the reloading yield stress at 45° and 90° is divided by the one along the RD with similar pre-strain level, as shown in Figure 77. At 3% pre-strain, the reloading yield stress is highest along TD, followed by the one along RD, with the lowest one at 45°. Similar trends are observed at 6% and 9% pre-strain, which are lowest at 45° also. However, the highest reloading yield stress is along RD.

Figure 78 shows the average reloading yield stress/unloading stress and Figure 79 presents the evolution of the normalized reloading stress σ_{be}/σ_r with the angle between two successive deformation axes at various pre-strains. The value along the RD is higher than TD, but a little higher than that along 45° at 6% and 9% pre-strain. At 3% pre-strain, the values are similar at different strain path change angle.

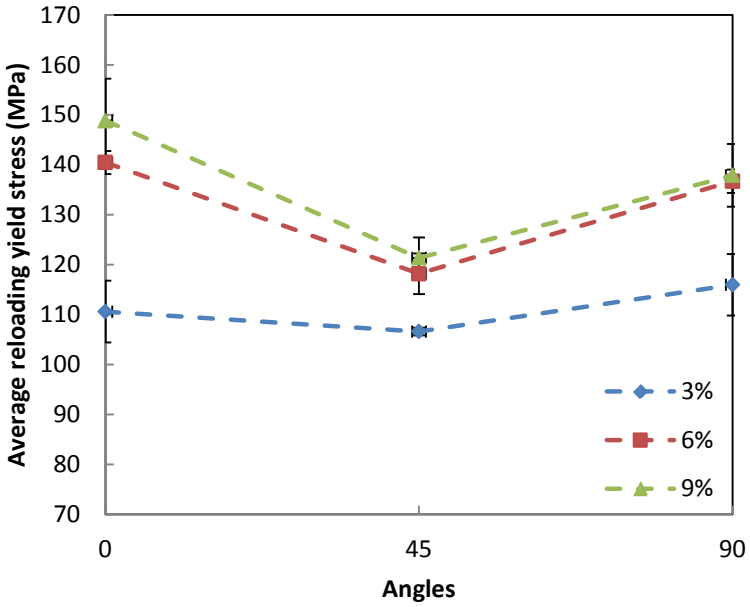

Figure 76. The average true reloading yield stress at various strain path change angles for approximately 3%, 6% and 9% pre-strains.

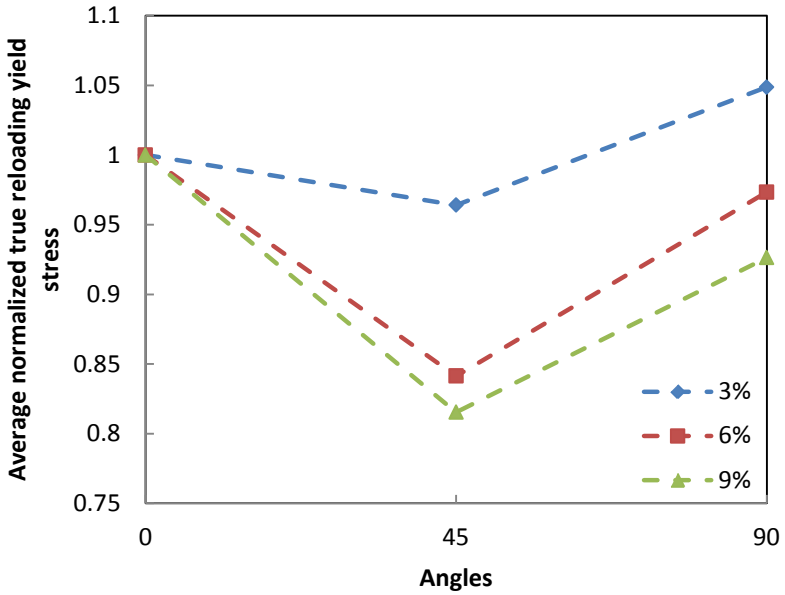

Figure 77. The average normalized true reloading yield stress at various strain path change angles for approximately 3%, 6% and 9% pre-strains.

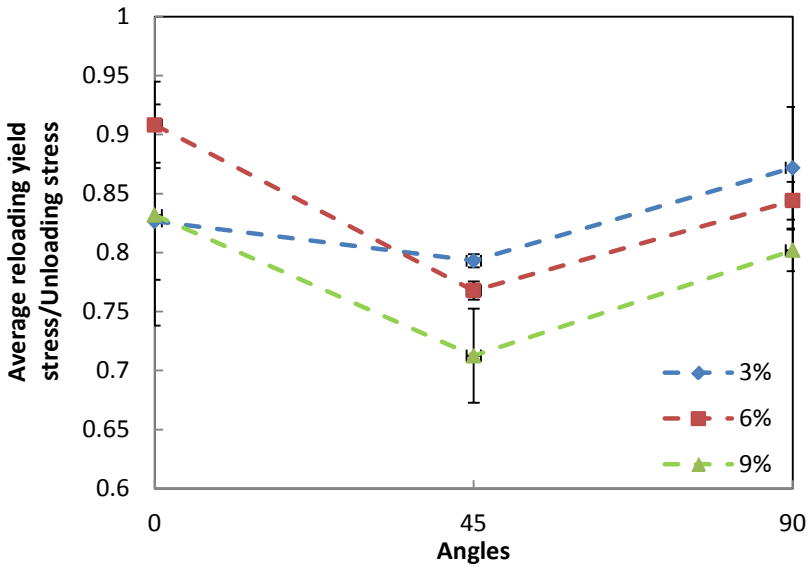

Figure 78. The average true reloading yield stress/ unloading stress at various strain path change angles for approximately 3%, 6% and 9% pre-strains.

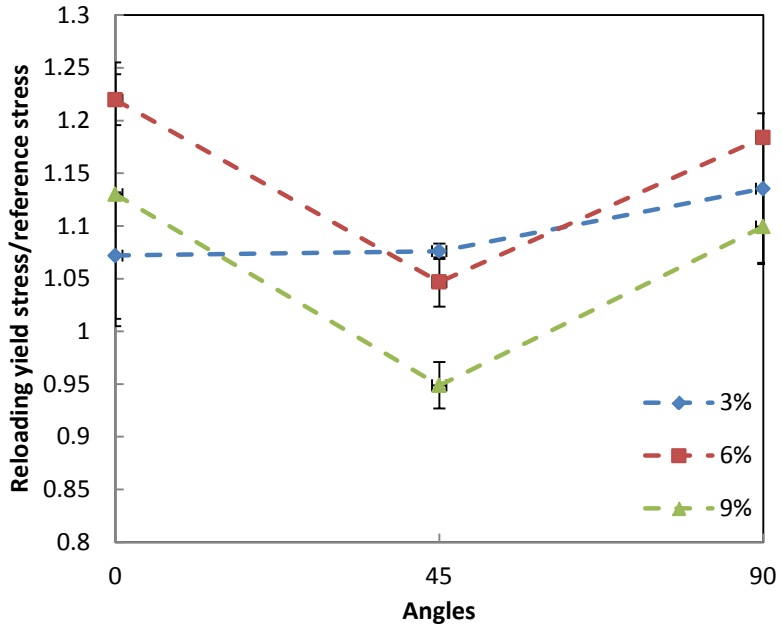

Figure 79. Evolution of the normalized reloading stress $^{\sigma_{be}}/_{\sigma_r}$ with the angle between two successive deformation axes.

4.2.4 **Work-hardening rate**

In this section, the work-hardening rate θ ($=^{d\sigma}/_{d\varepsilon}$) will be compared at various

pre-strains and strain path change angles. The work-hardening rate can help to understand the hardening behavior after yielding. Also, it can help to extract the ultimate tensile strength (UTS) and necking strain.

4.2.4.1 **Effect of pre-strain on work-hardening rate**

Figure 80, Figure 81 and Figure 82 show a plot of the true stress strain curve from DIC analysis and the work-hardening rate θ ($=^{d\sigma}/_{d\varepsilon}$). The intersection of the work-hardening rate curve with the stress strain curve indicates the onset of necking. Necking results from the balance between the cross-sectional area reduction and work-hardening of the increasing tensile plastic strain [98].

In Figure 80, after a strain path change at 0º, although the work-hardening rate is higher than the one without pre-strain (TS_S6), all work-hardening rates after strain path change are similar independently of pre-strain. In Figure 81 and Figure 82, when the strain path change angle is 45º and 90º, the work-hardening rate is higher than the one in monotonic loading after strain path change at low pre-strains (3% and 6%). With increasing pre-strain, the work-hardening rate decreases, and it is even lower than the one with monotonic loading.

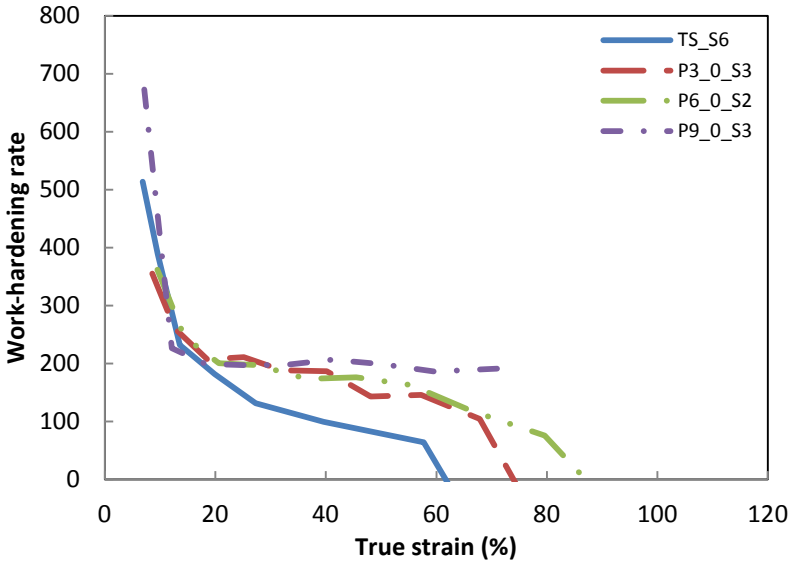

Figure 80. The plot of the work-hardening rate for uniaxial tension in the RD (TS_S6) after the change of strain path at 0° in 4.16% (P3_0_S3), 6.83% (P6_0_S2), and 15.3% (P9_0_S3).

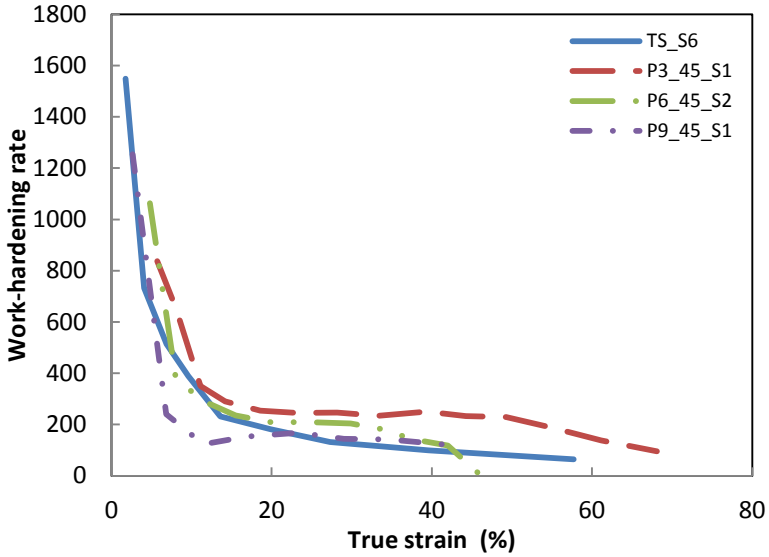

Figure 81. The plot of the work-hardening rate for uniaxial tension in the RD (TS_S6) after the change of strain path at 45° in 3.40% (P3_45_S2), 4.69% (P6_45_S2), and 9.31% (P9_45_S3).

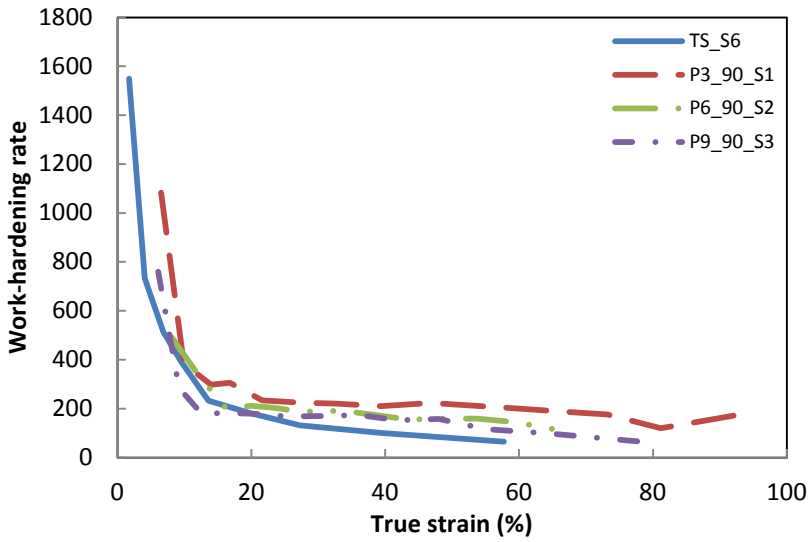

Figure 82. The plot of the work-hardening rate for uniaxial tension in the RD (TS_S6) the change of strain path at 90° in 3.73% (P3_90_S1), 5.43% (P6_90_S1), and 9.77% (P9_90_S3).

4.2.4.2 **Effect of strain path change angle on work-hardening rate**

Figure 83, Figure 84 and Figure 85 show the evolution of the work-hardening rate θ ($=^{d\sigma}/_{d\varepsilon}$) after strain path change at 0°, 45° and 90° with pre-strains of 3% (Figure 83), 6% (Figure 84), and 9% (Figure 85). As shown in Figure 83, Figure 84 and Figure 85, there are not significant differences in work-hardening rate that can be observed with similar amounts of pre-strain at different strain path change angles.

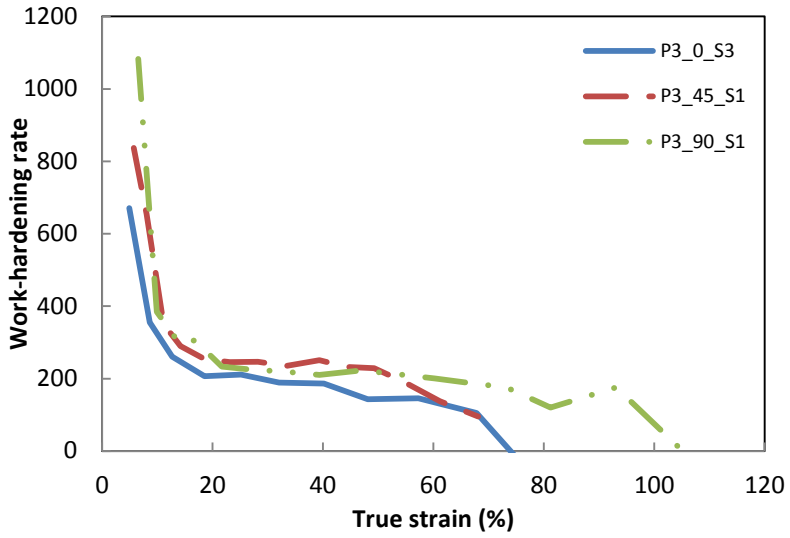

Figure 83. The plot of the work-hardening after pre-strain at 0° (P3_0_S3), 45° (P3_45_S2), and 90° (P3_90_S1) to the pre-strains axis for around 3% pre-strains.

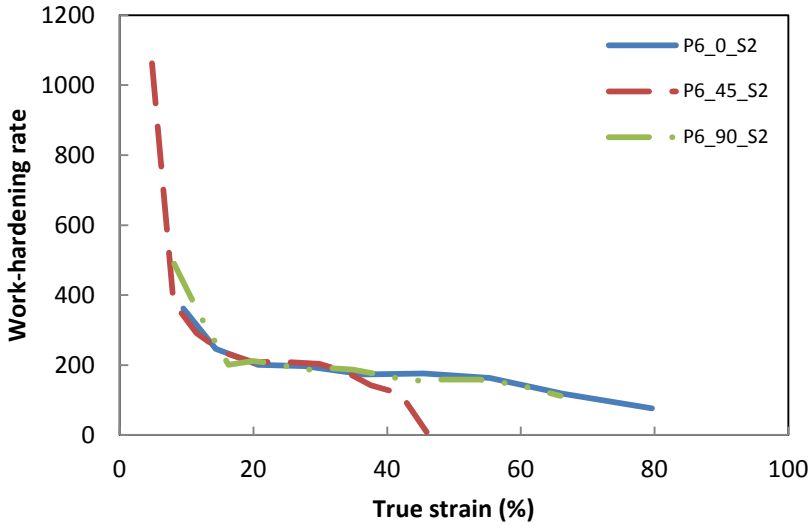

Figure 84. The plot of the work-hardening rate after pre-strain at 0° (P6_0_S2), 45° (P6_45_S2), and 90° (P6_90_S1) to the pre-strains axis at around 6% pre-strains.

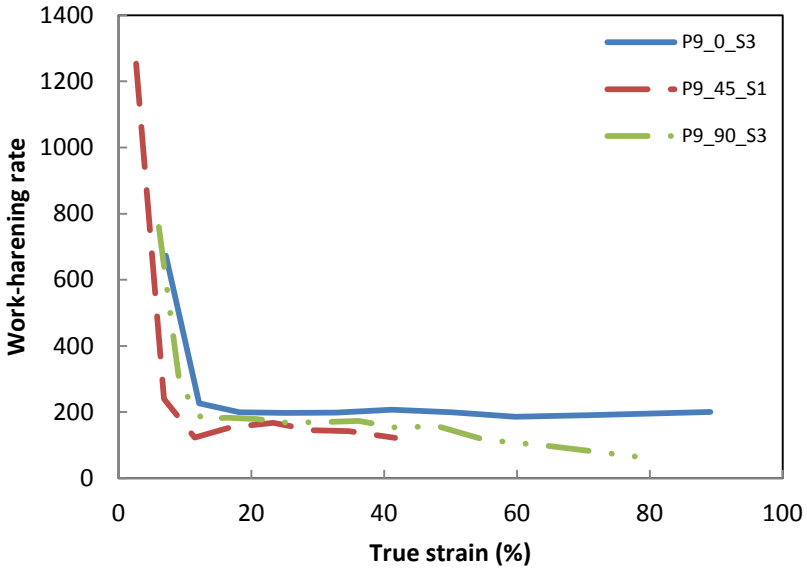

Figure 85. The plot of the work-hardening rate (a) and the true stress strain curve (b) after pre-strain at 0° (P9_0_S3), 45° (P9_45_S3), and 90° (P9_90_S3) to the pre-strains axis at around 9% pre-strains.

4.2.5 **UTS and effective necking strain**

In this section, the onset of necking defined as the intersection between the true stress strain curve and the work-hardening rate θ ($=^{d\sigma}/_{d\varepsilon}$) curve, will be presented. The definition of ultimate stress (σ_{UTS}) and necking strain ($\varepsilon_{necking}$) at this intersection is shown in Figure 86.

In order to study how the strain path change affects the necking strain, the total effective necking strain vs. pre-strains are calculated. The total effective necking strain ($\varepsilon_{total\ necking}$) is the total of effective necking strains after strain path change ($\varepsilon_e = \varepsilon_{necking} - \varepsilon_{be}$) and effective pre-strains ($\varepsilon_{ep} = \varepsilon_p - \varepsilon_y$), and is defined as follows.

$$\varepsilon_{total\ necking} = \varepsilon_e + \varepsilon_{ep} = \varepsilon_{necking} - \varepsilon_{be} + \varepsilon_p - \varepsilon_y \qquad \text{(Equation 4-1)}$$

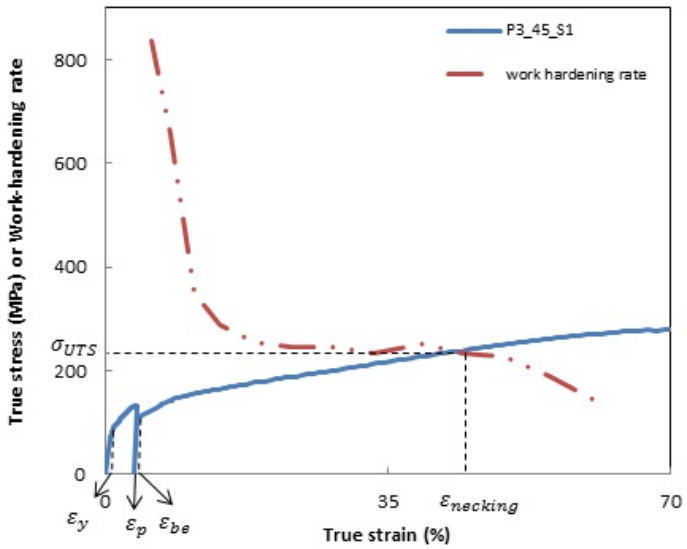

Figure 86. The definition of ultimate stress (σ_{UTS}) and necking strain ($\varepsilon_{necking}$).

4.2.5.1 **Effect of pre-strain on UTS and effective necking strain**

Figure 87 shows the average UTS with increasing pre-strain at various strain path change angles. One can see that the average UTS after strain path change is higher than the one without pre-strain. After strain path change at 45° and 90°, the average UTS decreases with increasing pre-strain. However, after strain path change at 0º, the average UTS are similar.

Figure 88 shows the average total effective necking strain at various pre-strains after strain path change at different angles. The general trend shows a peak in necking strain at about 3% pre-strain. Only the 0º shows a higher necking strain at high pre-strains.

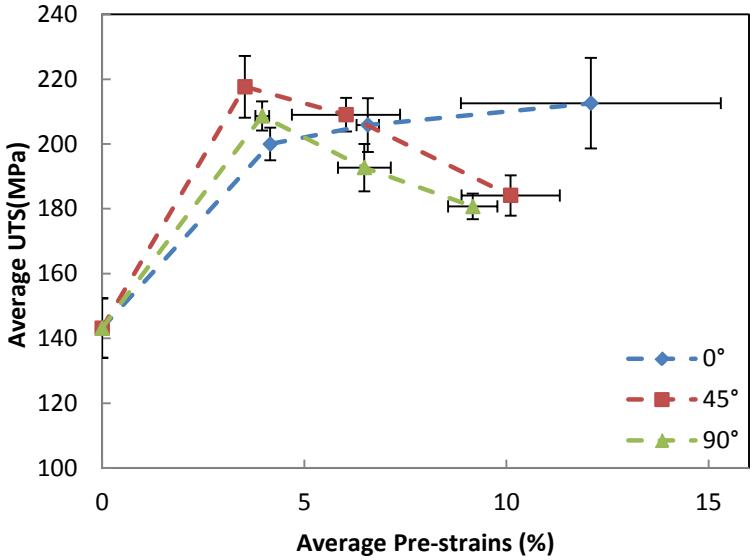

Figure 87. Average true UTS at various average pre-strains after the changes of strain path at 0°, 45° and 90°.

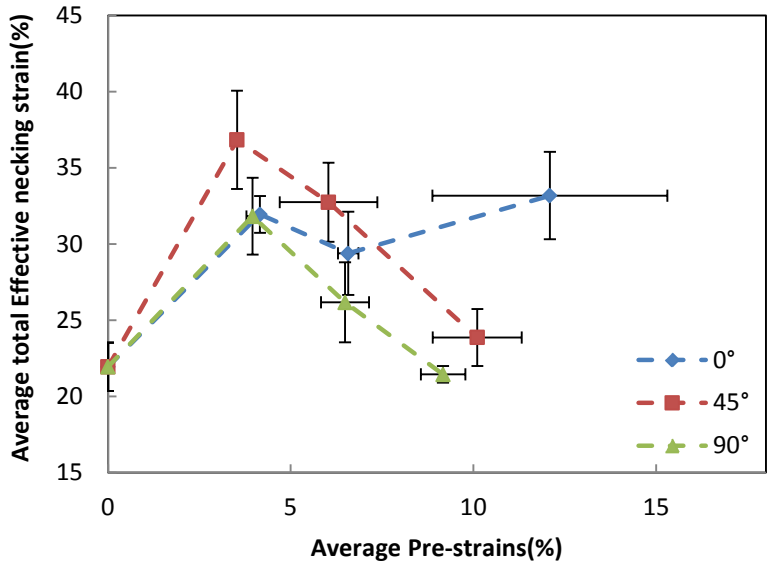

Figure 88. The average total effective necking strain at various average pre-strains after strain path change at 0°, 45° and 90°.

4.2.5.2 **Effect of strain path change angle on UTS and effective necking strain**

Figure 89 presents the average true UTS and Figure 90 is the total effective

necking strain measured in uniaxial tension at 0°, 45° and 90° to the RD after pre-strains of approximately 3%, 6% and 9% in plane strain along the RD. The UTS and necking strains are obtained by finding the intersection between the true stress strain curve and the work-hardening rate curve as described in section 4.2.6.

In Figure 89, when the pre-strains are around 3% and 6%, the highest average true UTS is found at the strain path change angle of 45°. At 6% pre-strain, similar values are observed at 0° and 90°, while the lowest one is at 0° with 3% pre-strain. At 9% pre-strain, the highest value is at 0°, followed by similar ones at 45° and 90°.

In Figure 90, similar trends can be observed at around 3% and 6% pre-strains. The average effective true UTS strain at 45° is higher than that along the TD and much higher than that along the RD. When the pre-strain amount is around 9%, the trend is similar to what has been observed for the true UTS.

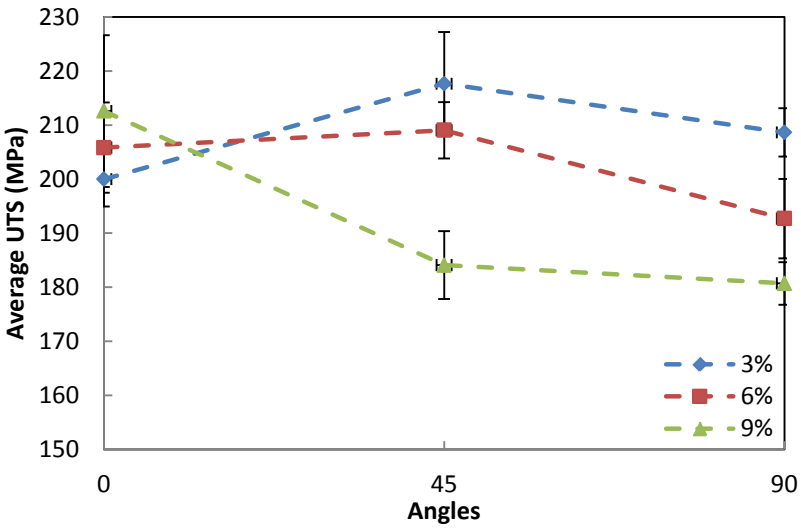

Figure 89. The average UTS at various orientations for approximately 3%, 6% and 9% pre-strains.

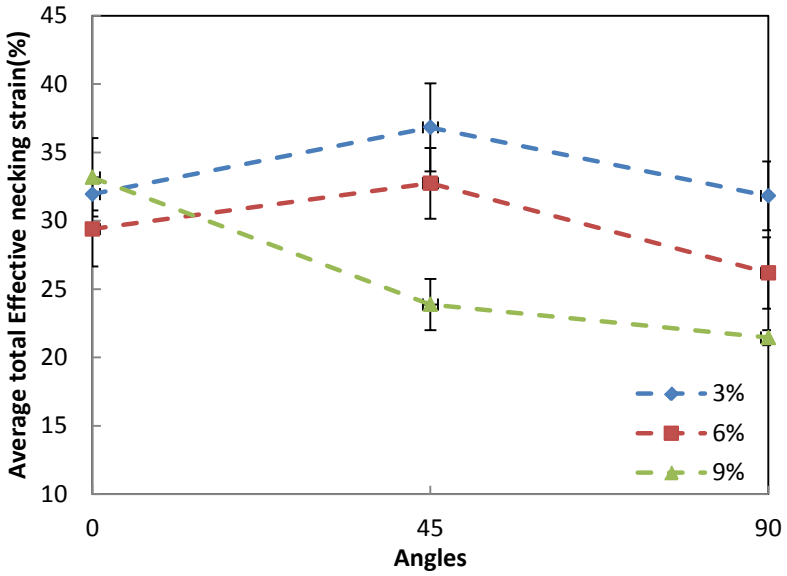

Figure 90. The average total effective necking strain at various orientations for approximately 3%, 6% and 9% pre-strains.

4.3 Strain distributions

4.3.1 Strain distribution in plane strain specimens

Figure 91 shows the strain distribution in the tensile direction of a plane strain sample after various amounts of strain calculated in the center of the sample (the location where the uniaxial tensile specimen will be later on extracted). In Figure 91 (a), there is a higher strain region appearing at the bottom left corner, which is the result of a stress concentration coming from a slight misalignment of the two grips of the tensile machine. The grip on left-hand side is closer than that on the right-hand side. At higher strains, a shear band can be observed across the gauge area, which is around 45° to the tensile direction.

When comparing the strain distributions with other plane strain specimens with

similar tensile strains in the center, as shown in Figure 91 (j) PS_test12 (10.00%), and Figure 92 (a) PS_test13 (9.94%), (b) PS_test14 (9.98%), and (c) PS_test15 (10.06%), one can see that the strain distributions are different. In Figure 92 (a), there is no obvious band observed across the specimen. This indicates that the strain distributions rely on how well the grips were tightened and how well the samples are aligned.

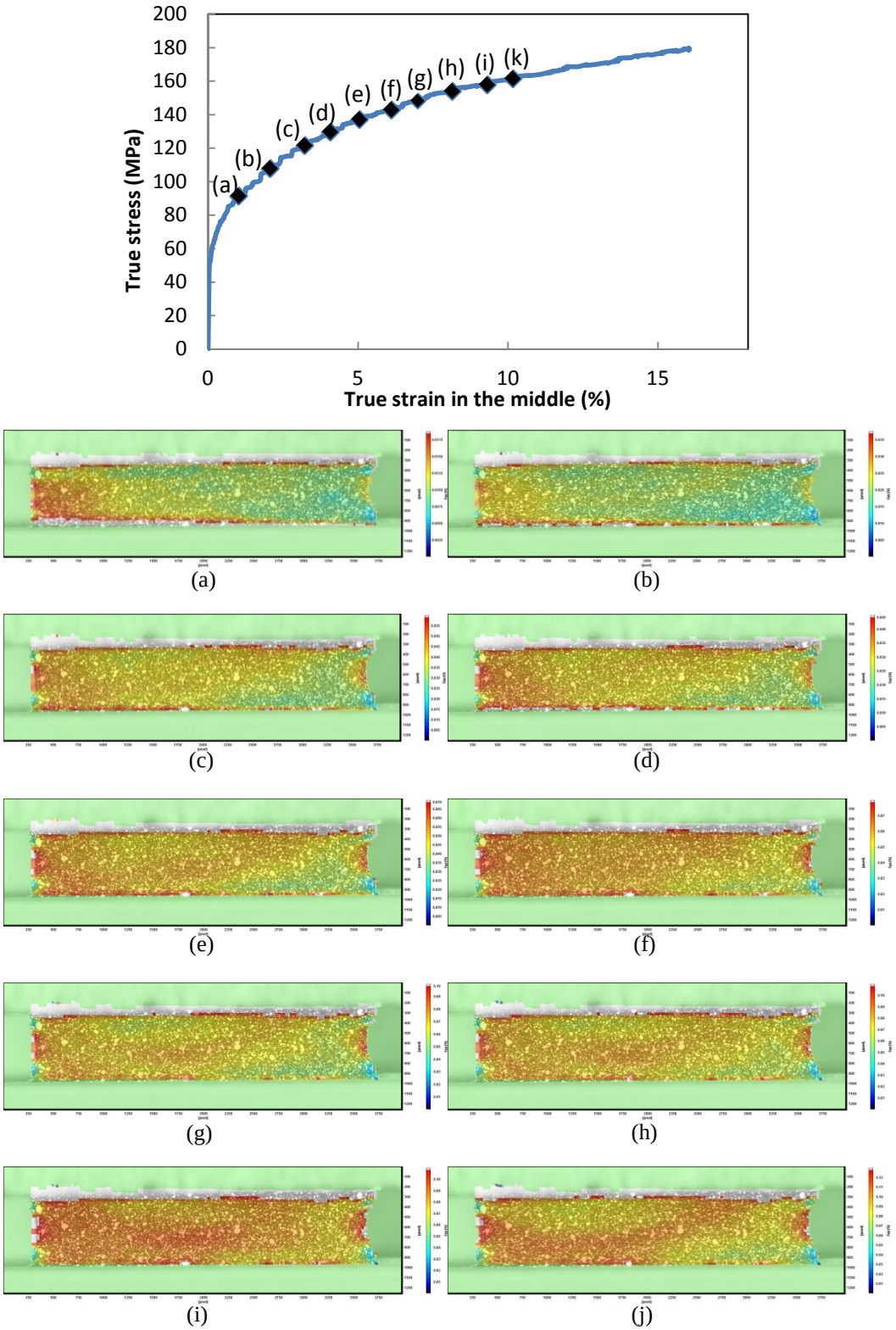

Figure 91. Stress strain curve of plane strain test (PS_test12) and its strain distributions in tensile direction for (a) 1.01%, (b) 2.06%, (c) 3.00%, (d) 3.99%, (e) 5.05%, (f) 6.02%, (g) 7.13%, (h) 8.08%, (i) 9.08% and (j) 10.00% in the center.

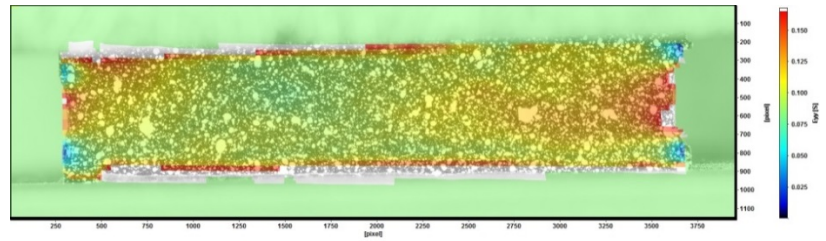

(a)

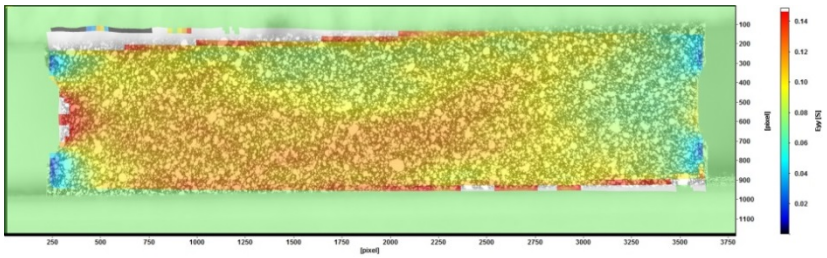

(b)

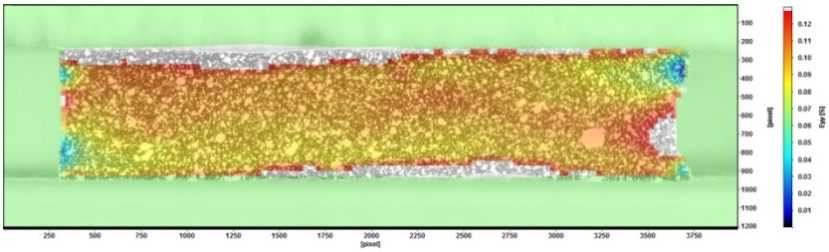

(c)

Figure 92. Strain distributions of plane strain tension in tensile direction (a) specimen PS_test13 when strain is 9.94%, (b) specimen PS_test14 when strain is 9.98%, and (c) specimen PS_test15 when strain is 10.06% in the center.

4.3.2 **Strain distributions of tensile specimens**

Figure 93 shows the strain distributions in tensile specimens at various true strains. As shown in Figure 93 (a), when the specimen is at the yield stress, strains develop in the center of the specimen because of the reduction in the gauge width which creates a stress concentration. The strain then propagates from the center of the gauge towards the grips region as the sample is loaded further.

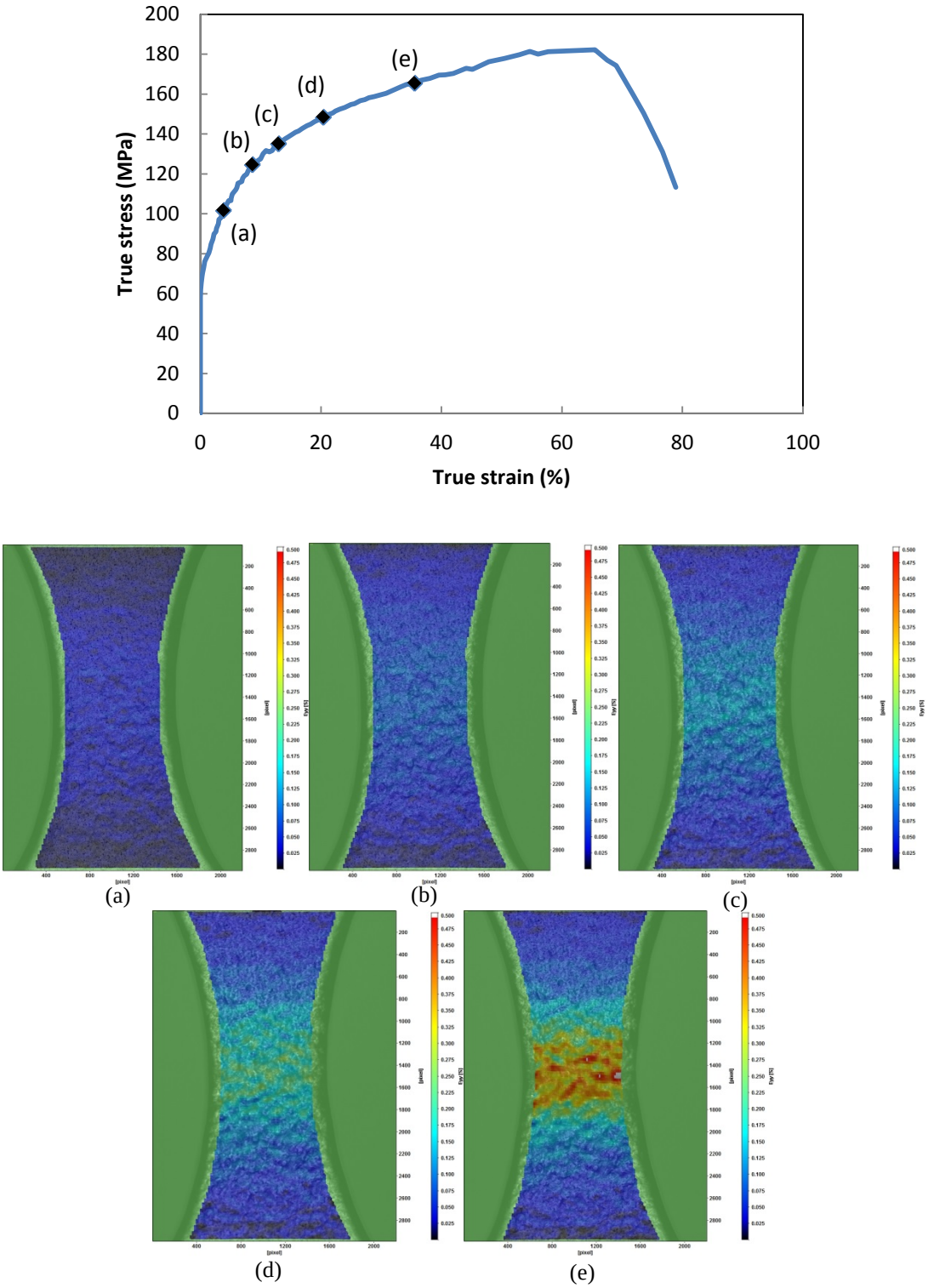

Figure 93. Strain distribution of uniaxial tension without pre-strains at the true strain of (a) 3.73%, (b) 8.24%, (c) 12.71%, (d) 20.623%, and (e) 35.68%.

4.3.3 **Strain distribution after strain path change**

Table 11 shows a summary of the direction of the figures where strain distribution after strain path change are presented. To make it more clear and simple, Figure 94, Figure 95 and Figure 98 show the strain distributions in the tensile direction of strain path change specimens at 0° with around 3%, 6% and 9% pre-strains, respectively. Figure 95, Figure 96 and Figure 97 show the strain distributions of strain path change specimens at 0°, 45°, and 90°, respectively, in the tensile direction with around 6% pre-strain. The rests of the figures after strain path change are shown in Appendix C.

In the pre-strain stage, the strain distribution is similar to that of the plane strain specimen. A random band can be observed which is related to the tightening and alignment of the grips as mentioned in 4.3.1 when unloading (see Figure 94(c), 95 (e), 96 (d), 97 (e), and 98 (f)).

After reloading, the effect of pre-strain and strain path change angle on the strain distribution are not very different. The strain distribution during reloading is similar to that of uniaxial tension in 4.3.2. Strains develop in the center of the specimen because of the reduction in the gauge width, and then propagate from the center of the gauge towards the gripped region as the sample is further loaded.

Table 11. The direction of figures showing the strain distribution of strain path change specimens.

Pre-strain/strain path change angle	**0º**	**45º**	**90º**
3%	Figure 94	Figure 112 (in Appendix C)	Figure 113 (in Appendix C)
6%	Figure 95	Figure 96	Figure 97
9%	Figure 98	Figure 114 (in Appendix C)	Figure 115 (in Appendix C)

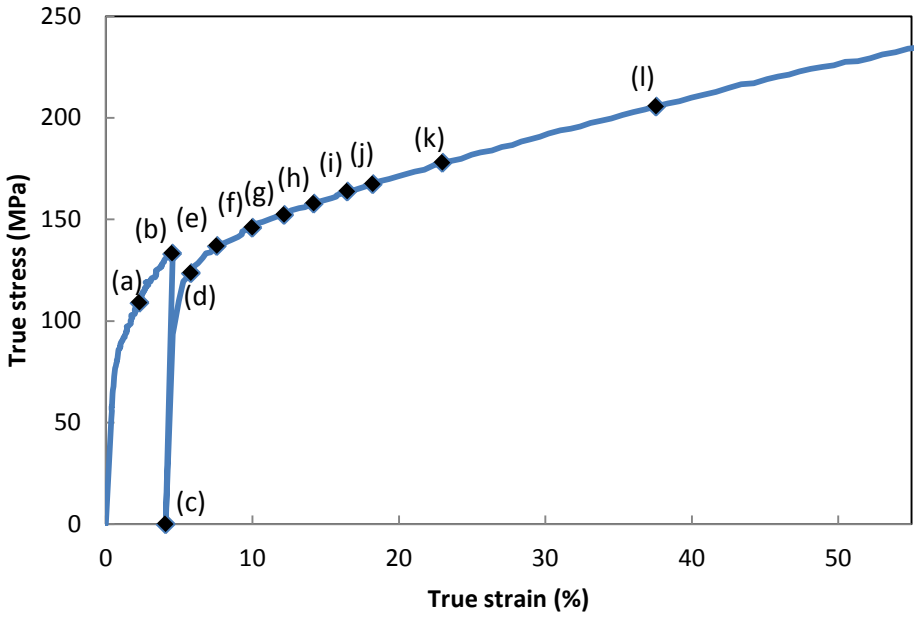
250
200
150
100
50
0
True stress (MPa)
0
10
20
30
40
50
True strain (%)
(a)
(b)
(c)
(d)
(e)
(f)
(g)
(h)
(i)
(j)
(k)
(l)

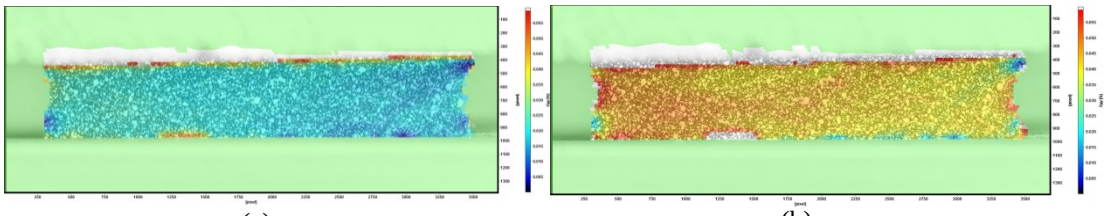

(a) (b)

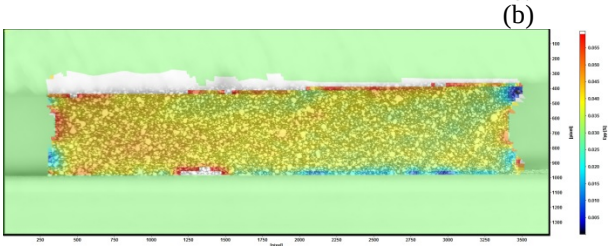

(c)

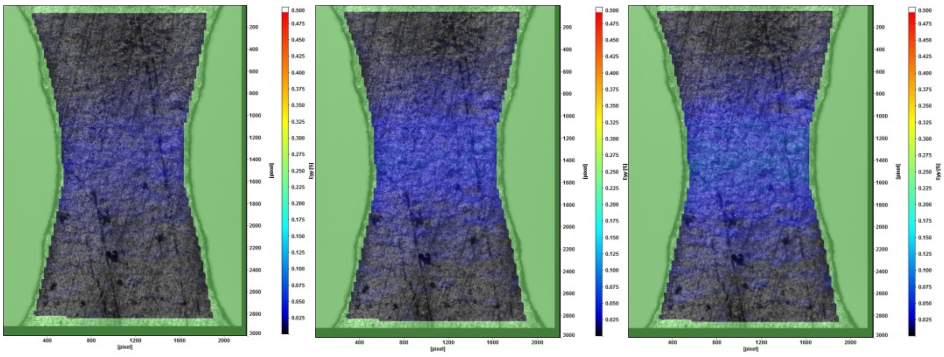

(d) (e) (f)

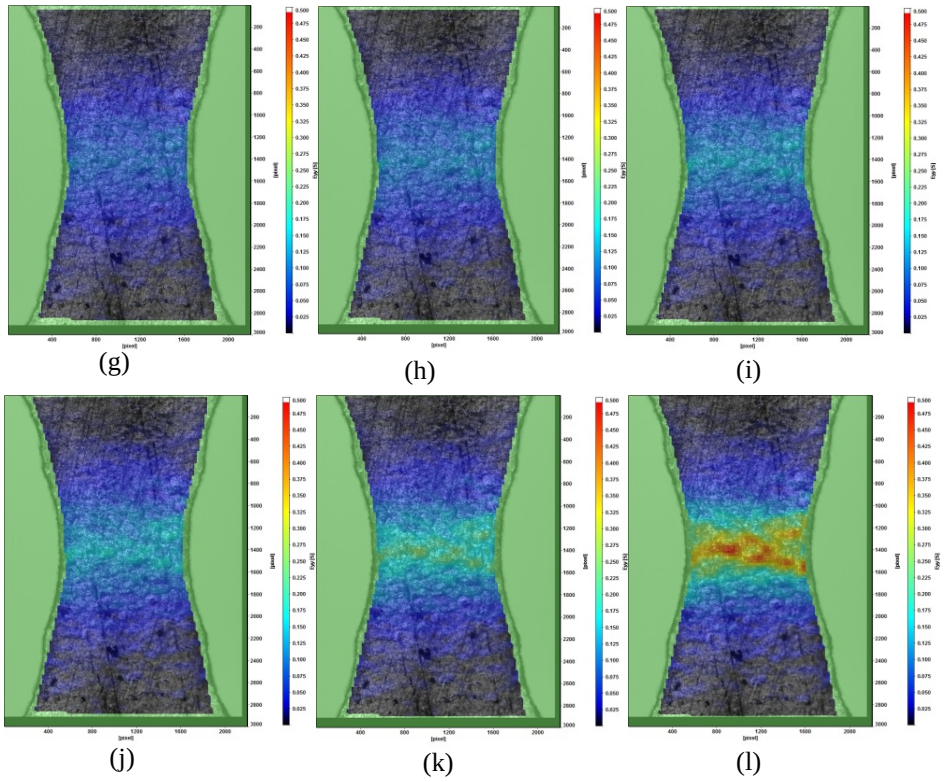

Figure 94. Stress strain curve of strain path change test (P3_0_S3), which is pre-strained for around 3% and at 0°, and its strain distributions in tensile direction for (a)2.03%, (b) 4.52%, (c) 4.07%, (d)6.09%, (e) 8.07%, (f) 9.93%, (g)12.17%, (h) 14.09%, (i) 16.31%, (j) 17.91%, (k) 23.87%, and (l) 37.69%. (a), (b) and (c) are in the pre-strain stage.

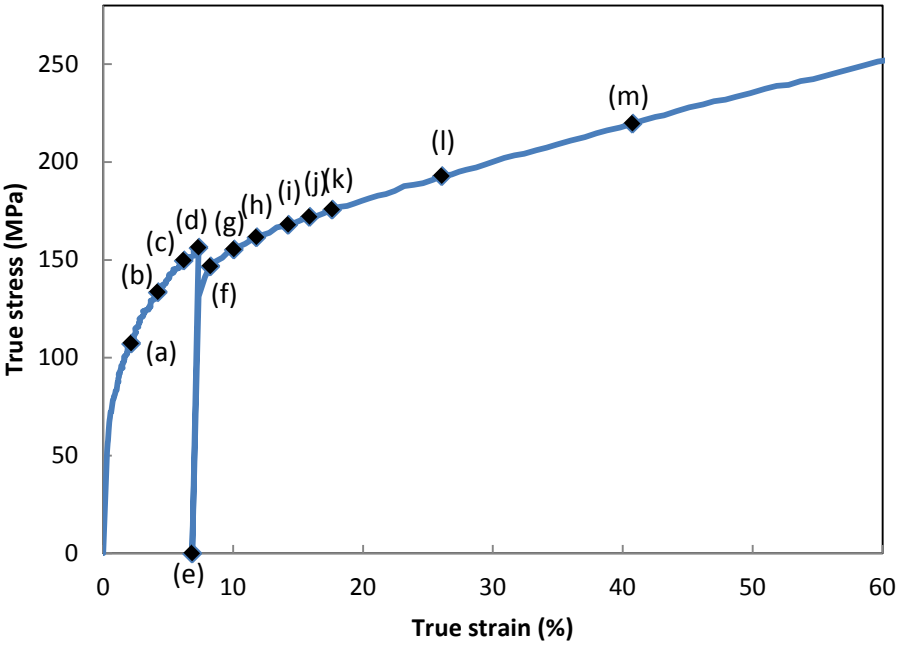
True stress (MPa)
True strain (%)
0
50
100
150
200
250
0
10
20
30
40
50
60
(a)
(b)
(c)
(d)
(e)
(f)
(g)
(h)
(i)
(j)
(k)
(l)
(m)

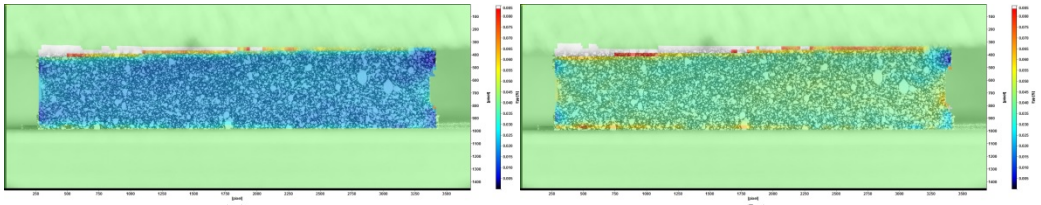

(a) (b)

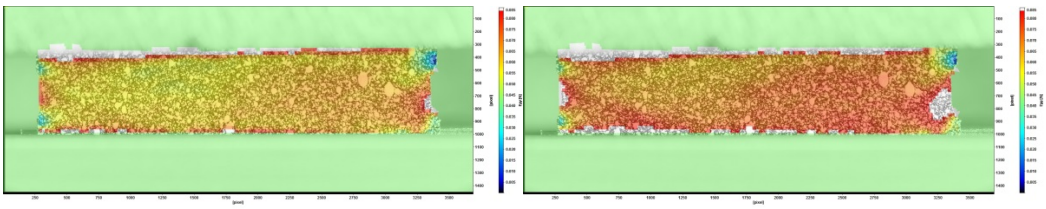

(c) (d)

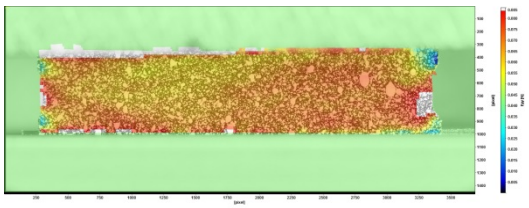

(e)

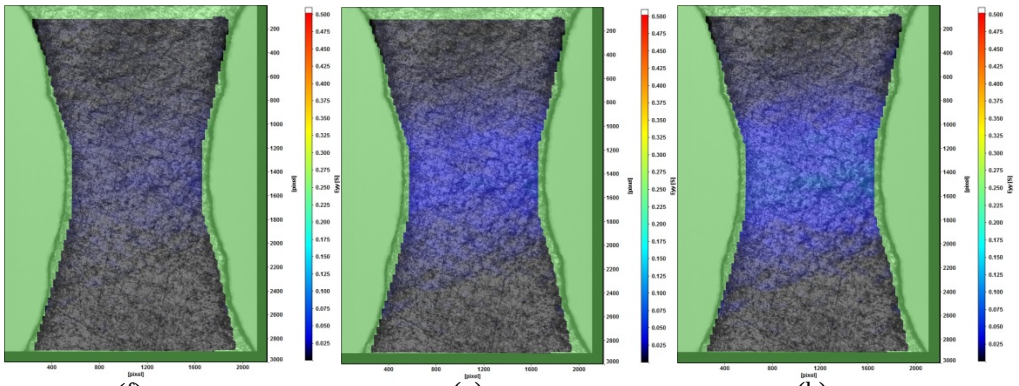

(f) (g) (h)

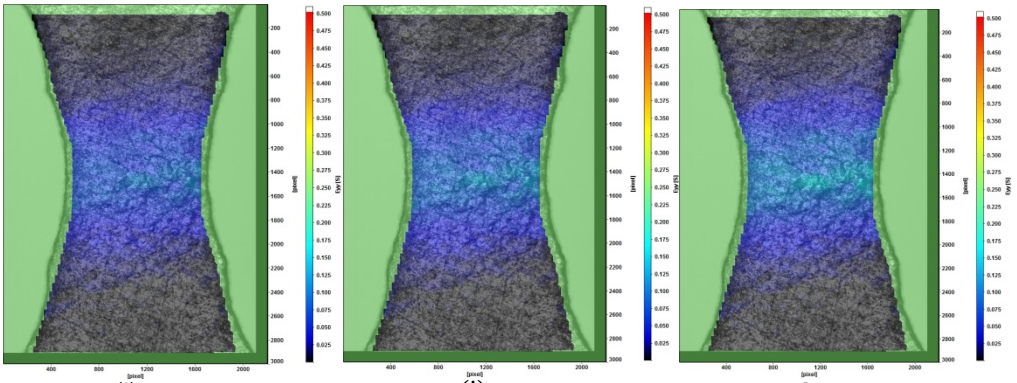

(i) (j) (k)

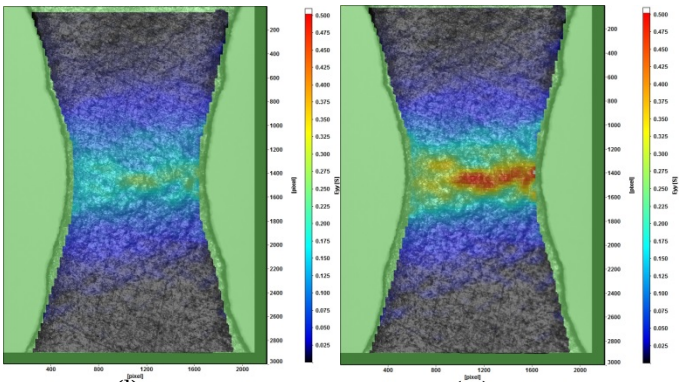

(l) (m)

Figure 95. Stress strain curve of strain path change test (P6_0_S2), which is pre-strained for around 6% and at 0°, and its strain distributions in tensile direction for (a)1.96%, (b) 3.97%, (c) 6%, (d)7.24%, (e) 6.84%, (f) 7.99%, (g)10.06%, (h) 11.96%, (i) 14.08%, (j)15.84%, (k) 17.91%, (l) 24.08%, and (m) 37.7%. (a), (b), (c), (d), and (e) are in the pre-strain stage.

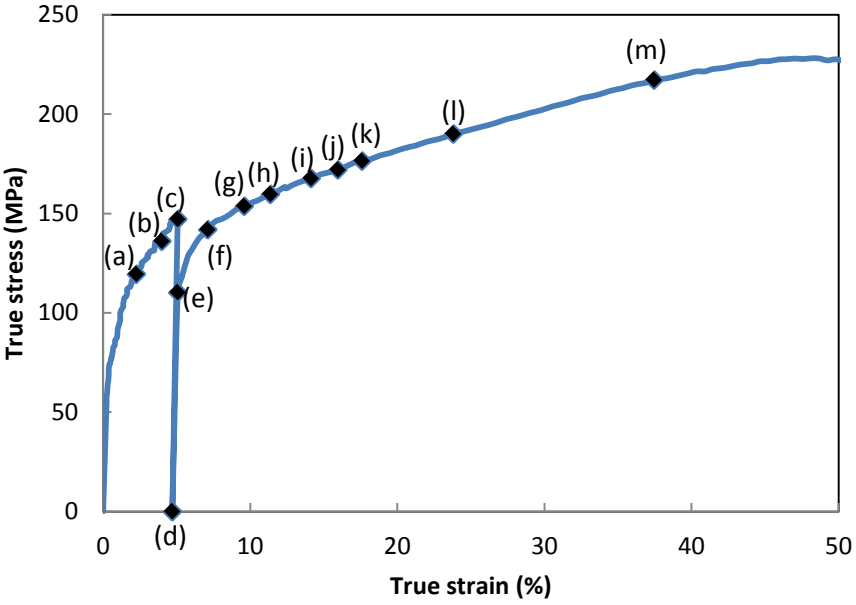
250
200
150
100
50
0
True stress (MPa)
0
10
20
30
40
50
True strain (%)
(a)
(b)
(c)
(d)
(e)
(f)
(g)
(h)
(i)
(j)
(k)
(l)
(m)

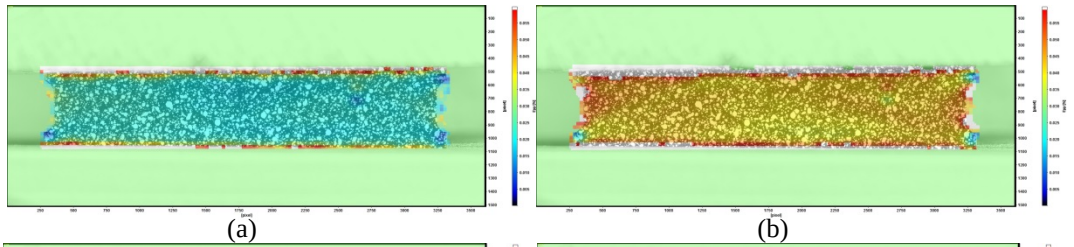
(a)
(b)

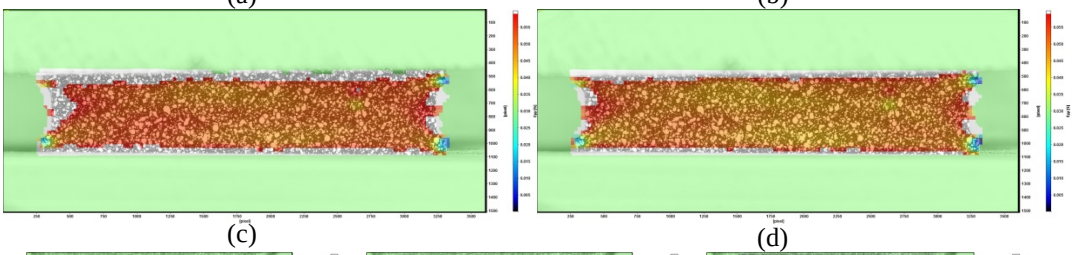
(c)
(d)

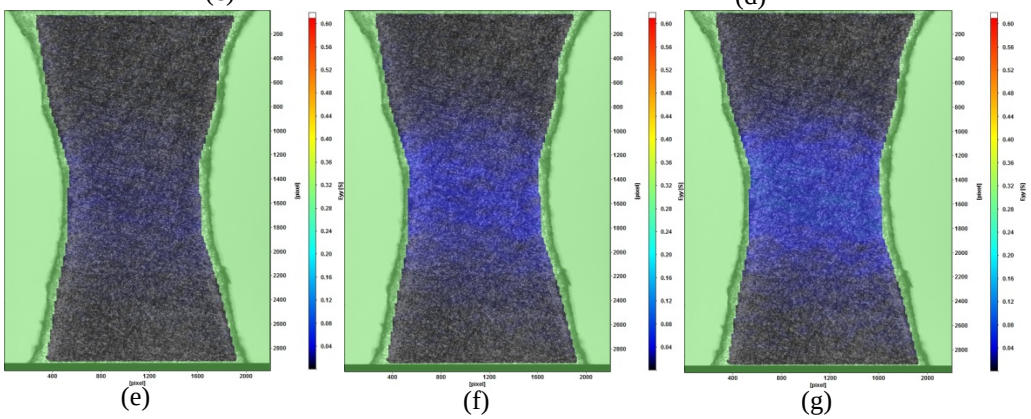
(e)
(f)
(g)

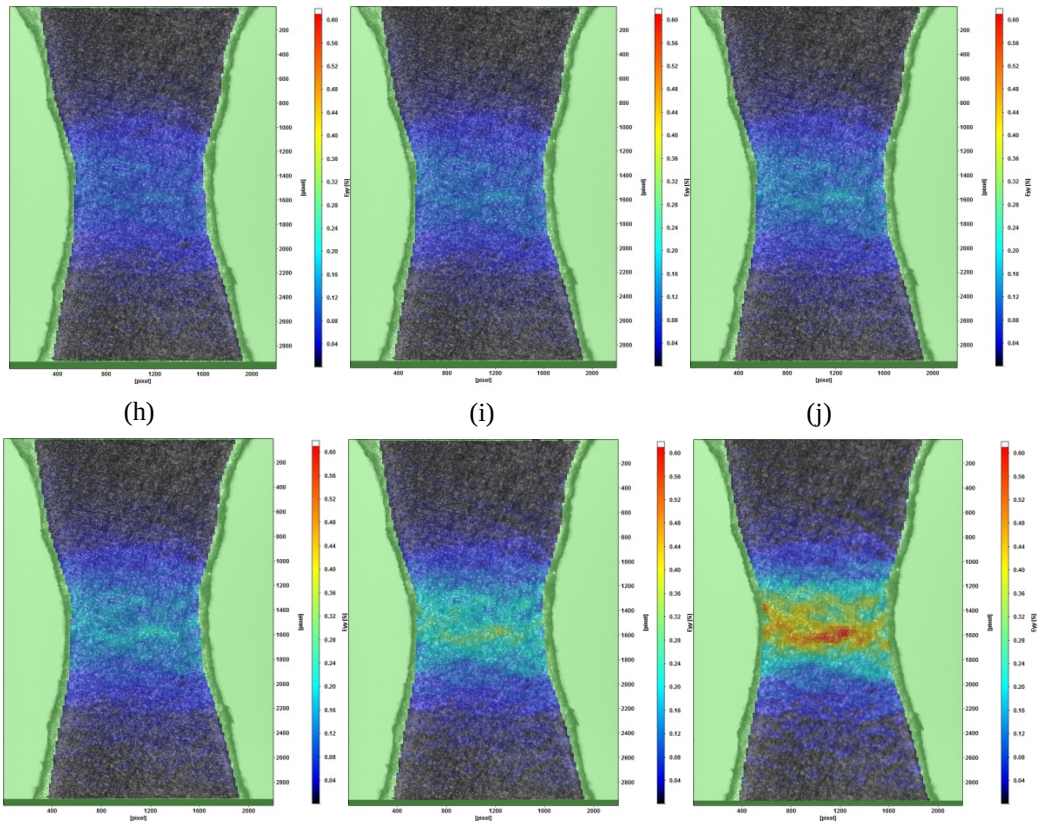

(h) (i) (j)

(k) (l) (m)

Figure 96. Stress strain curve of strain path change test (P6_45_S2), which is pre-strained for around 6% and at 45°, and its strain distributions in tensile direction for(a)1.94%, (b) 4%, (c) 5.06%, (d)4.69%, (e) 5.96%, (f) 8.17%, (g) 9.79%, (h) 12.16%, (i) 14.02%, (j)15.8%, (k) 17.99%, (l) 24.25%, and (m) 38.04%. (a), (b), (c), and (d) are in the pre-strain stage.

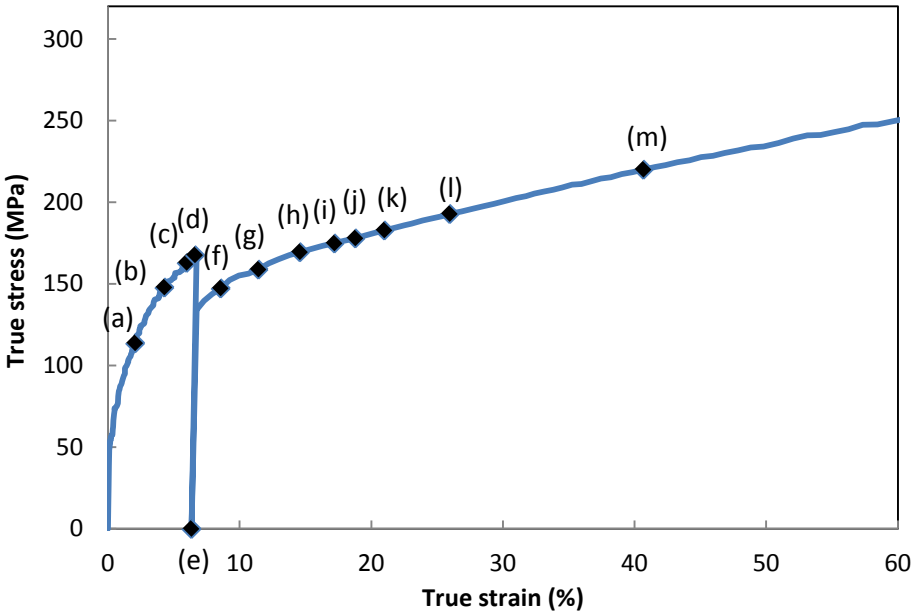
True stress (MPa)
True strain (%)
300
250
200
150
100
50
0
0
10
20
30
40
50
60
(a)
(b)
(c)
(d)
(e)
(f)
(g)
(h)
(i)
(j)
(k)
(l)
(m)

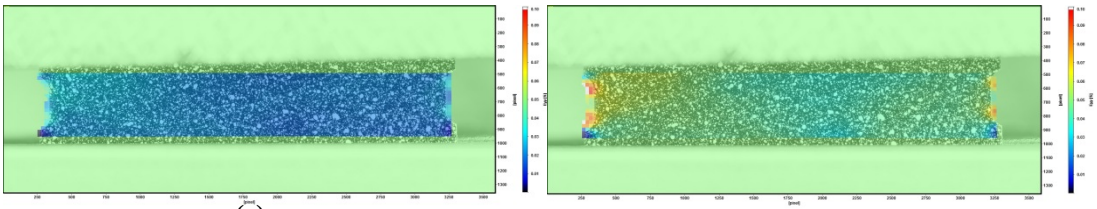

(a) (b)

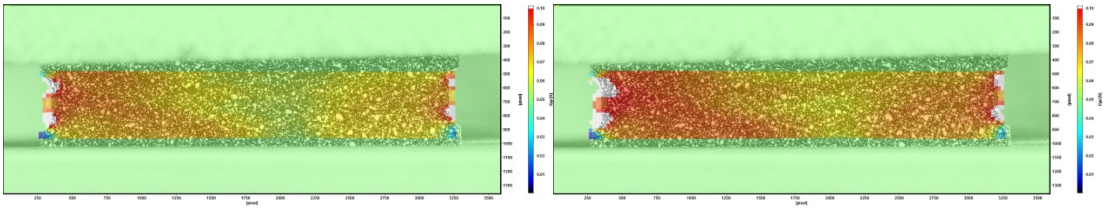

(c) (d)

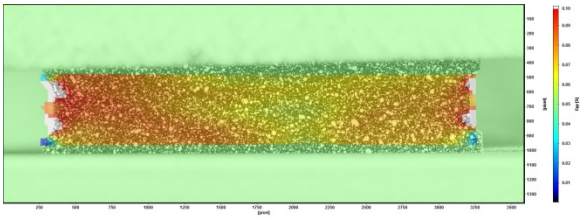

(e)

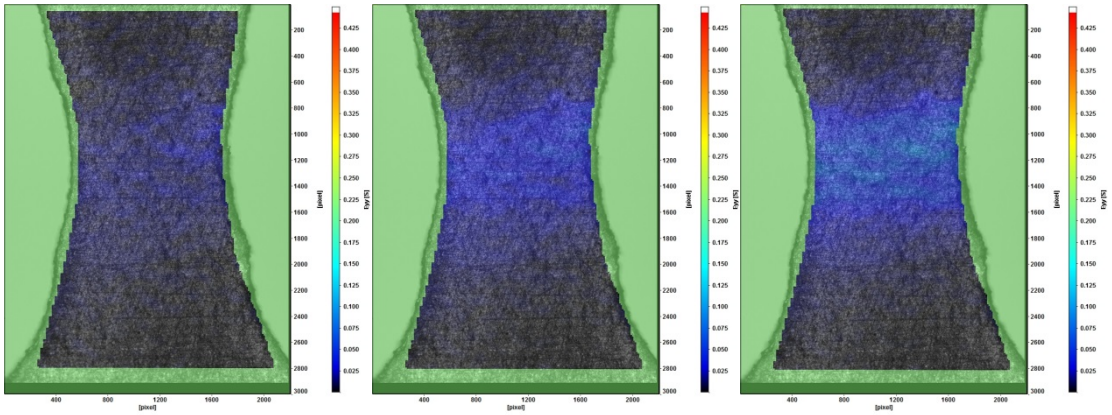

(f) (g) (h)

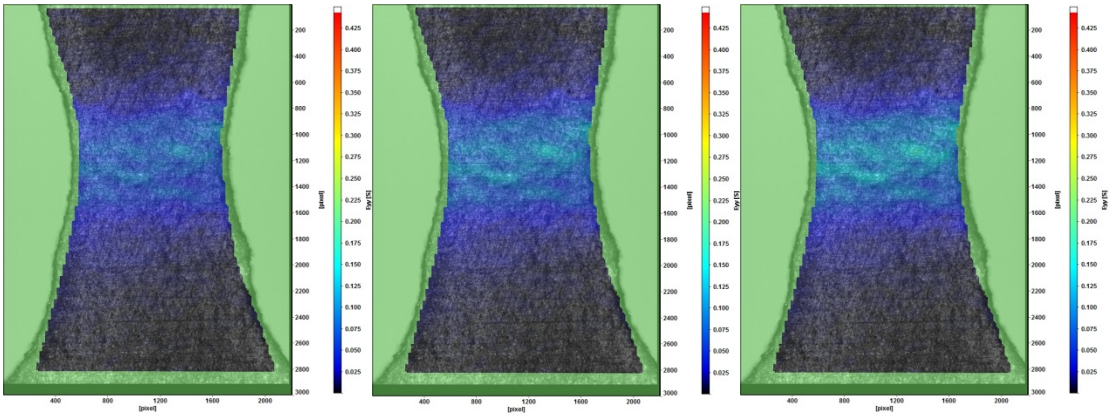

(i) (j) (k)

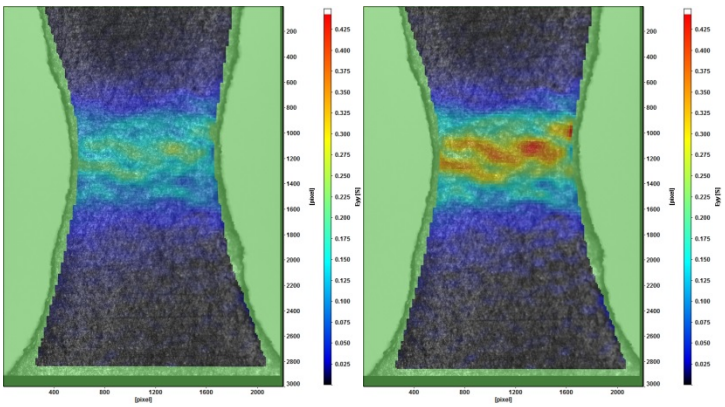

(l) (m)

Figure 97. Stress strain curve of strain path change test (P6_90_S2), which is pre-strained for around 6% and at 90°, and its strain distributions in tensile direction for (a)2.06%, (b) 4.04%, (c) 5.98%, (d) 6.73%, (e) 6.33%, (f) 7.89%, (g) 9.82%, (h) 12.33%, (i) 13.83%, (j)16.07%, (k) 17.68%, (l) 24.36%, and (m) 37.59%. (a), (b), (c), (d), and (e) are in the pre-strain stage.

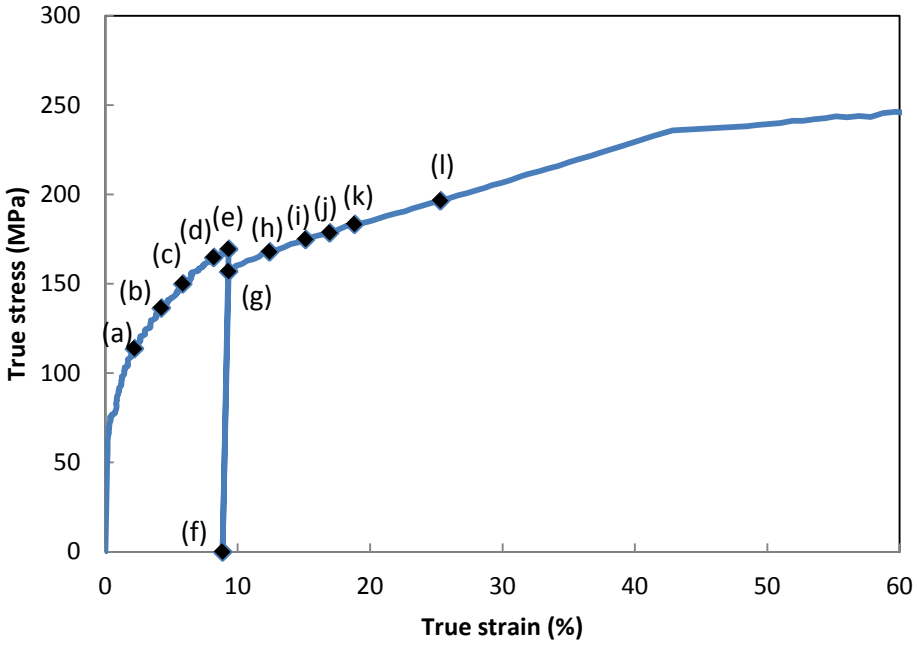
300
250
200
150
100
50
0
True stress (MPa)
0
10
20
30
40
50
60
True strain (%)
(a)
(b)
(c)
(d)
(e)
(f)
(g)
(h)
(i)
(j)
(k)
(l)

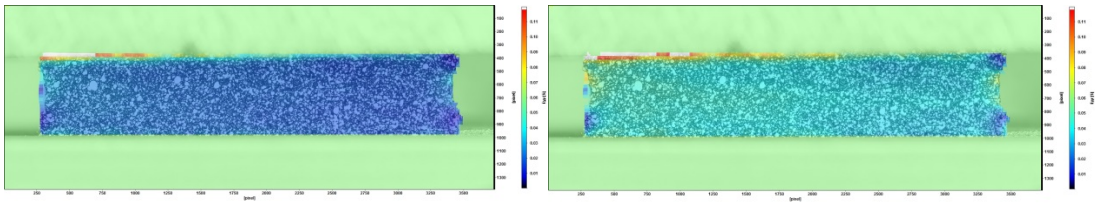

(a) (b)

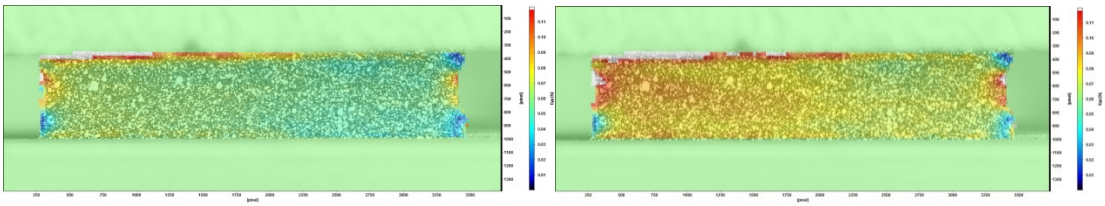

(c) (d)

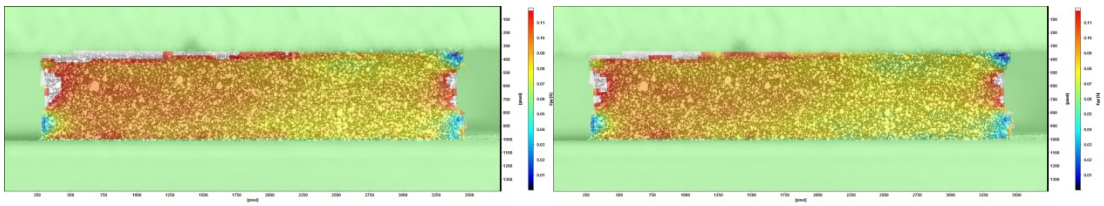

(e) (f)

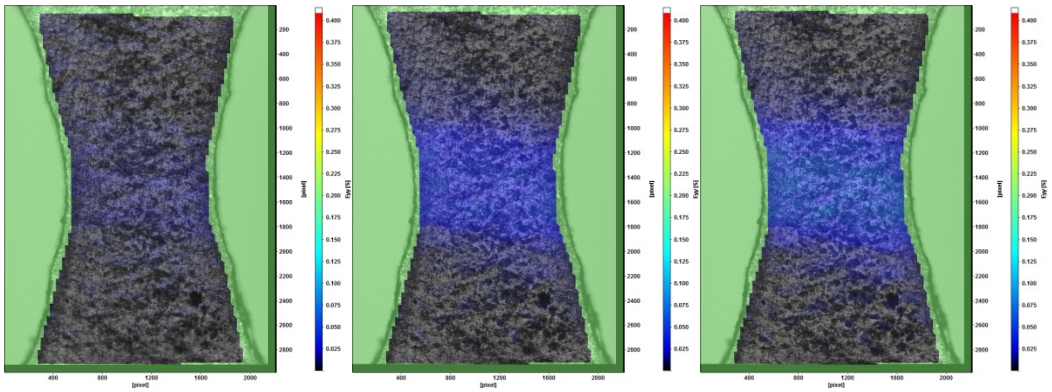

(g) (h) (i)

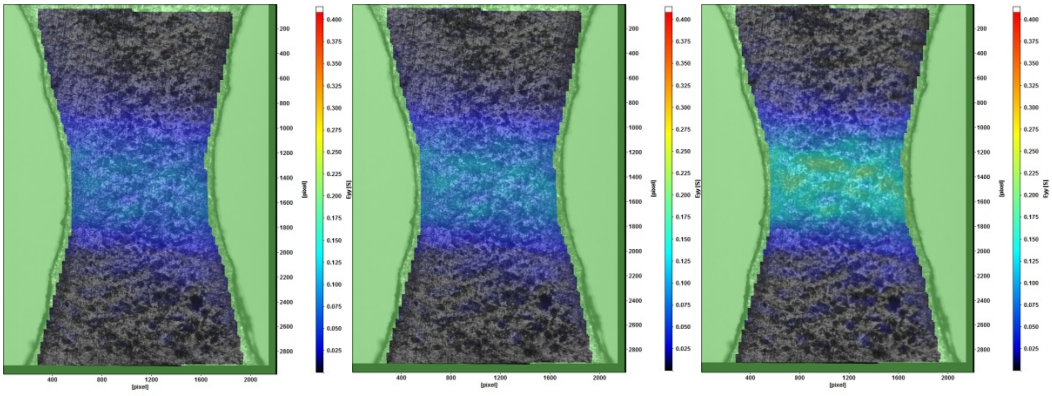

(j) (k) (l)

Figure 98. Stress strain curve of strain path change test (P9_0_S2), which is pre-strained for around 9% and at 0°, and its strain distributions in tensile direction for (a) 2%, (b) 4.04%, (c) 6%, (d)8.02%, (e) 9.3%, (f) 8.86%, (g) 9.86%, (h) 12.26%, (i) 13.94%, (j) 16.08%, (k) 17.86%, and (l) 24.16%. (a), (b), (c), (d), (e), and (f) are in the pre-strain stage.

4.4 Effect of strain path change on facture surface

Fracture surfaces that were observed in the SEM are shown in Figure 99 and 100. From these pictures, the final fracture area (A_f), which corresponds to the dimpled area (see Figure 99 (c)), is measured by using the open-source software ImageJ. The initial thickness (t_o) can be measured using a micrometer after pre-straining. The initial width (L_o) can be known from the optical images taken under the microscope. The true fracture strain ε_f can then be calculated by using the equation (Equation

4-12) below.

$$\varepsilon_f = \ln(\frac{t_o L_o}{A_f}) \qquad \text{(Equation 4-2)}$$

As shown in Figure 101, the final strain for specimens without pre-strain (0%) is lower than those after pre-straining (represented at the horizontal line). In Figure 101, after pre-strains at 0°, 45° and 90° to the tensile axis, no trends can be observed. Figure 102 shows the average final strains after pre-straining at 0°, 45° and 90° to the pre-strain tensile axis. No trends can be observed suggesting that pre-straining the sample does not significantly affect the true failure strains, *i.e.* the ductility of the sample.

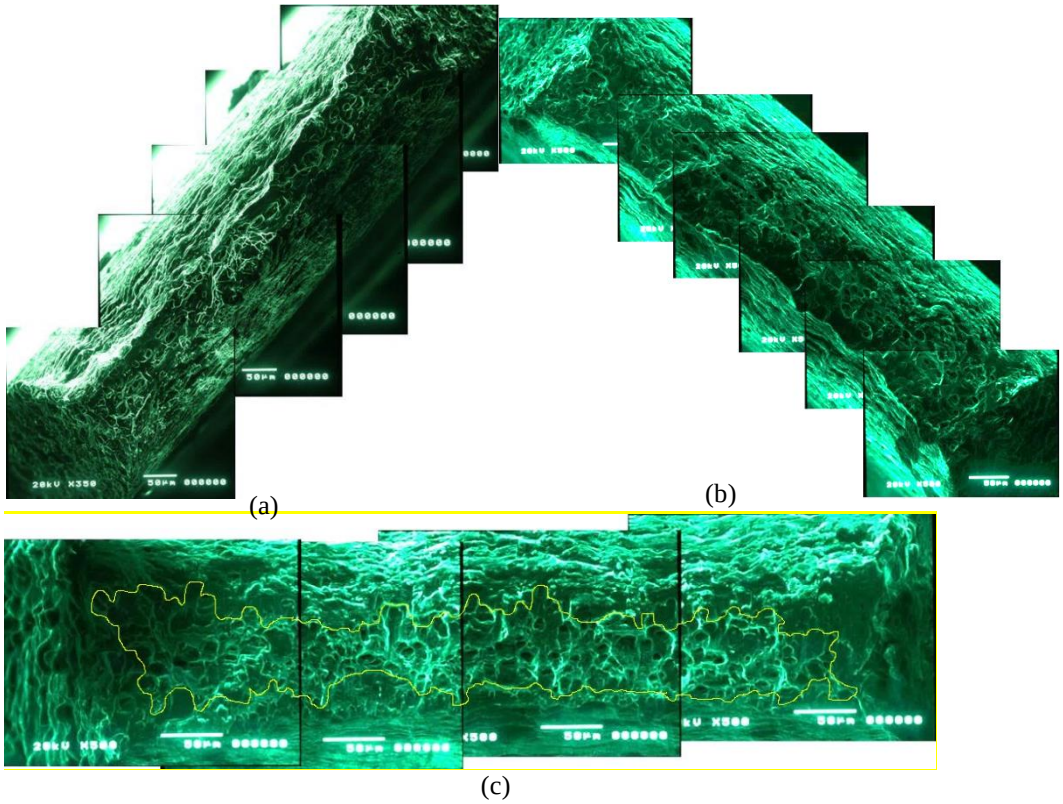

(a) (b)

(c)

Figure 99. SEM image of the fracture surface after the strain path change at 0° angle to the pre-strain axis with the pre-strain amount of (a) 4.15% (P3_0_S3), (b) 6.02% (P6_0_S1), and (c) 7.62% (P9_0S_1).

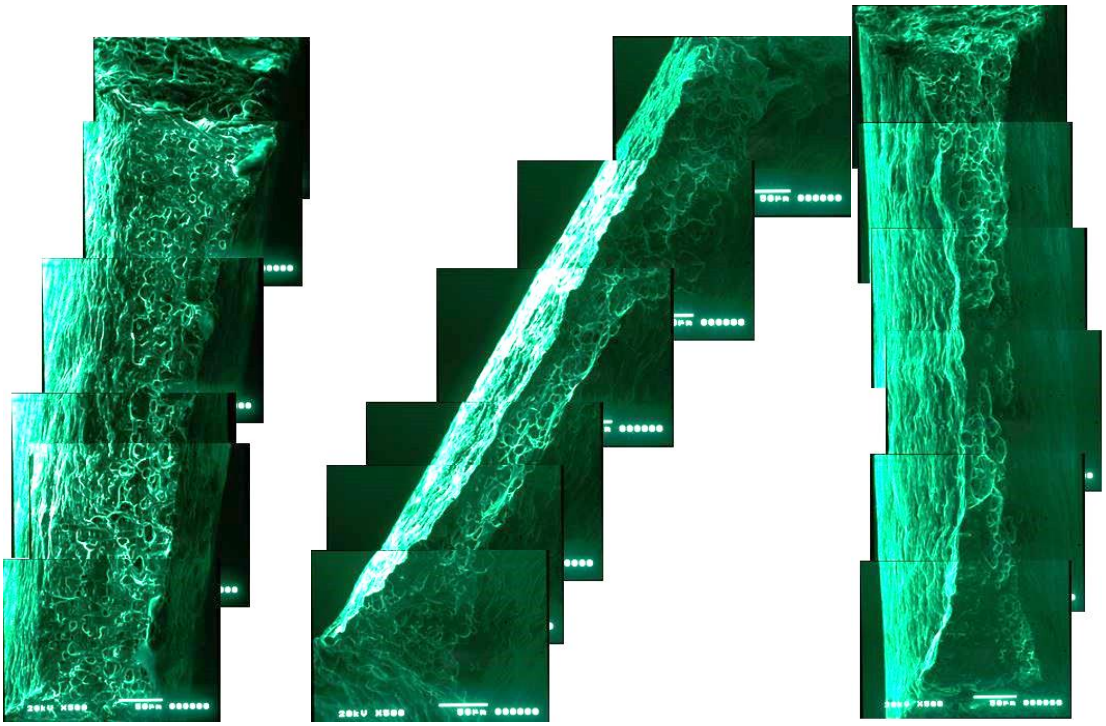

(a) (b) (c)

Figure 100. SEM image of the fracture surface after the strain path change at 45° angle to the pre-strain axis with the pre-strain amount of (a) 3.59% (P3_45_S1), (b) 7.37% (P6_45_S3), and (c) 7.62% (P9_45_S2).

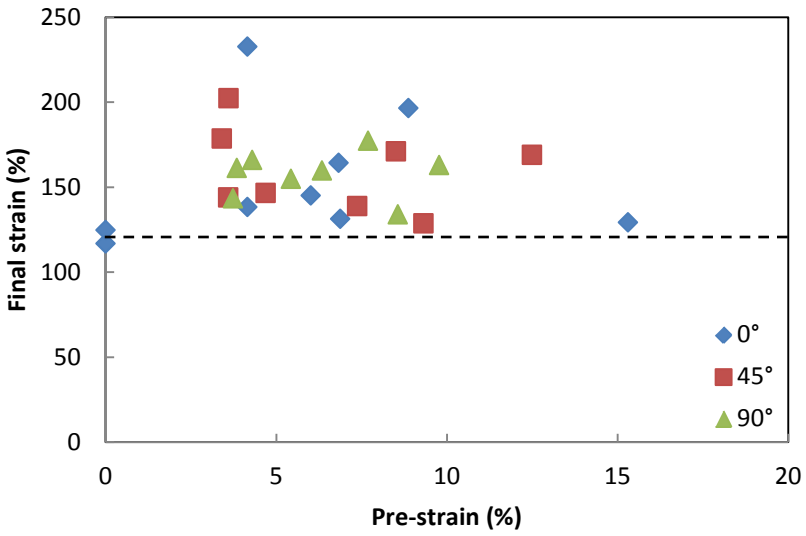

Figure 101. The final strains at various average pre-strains when the pre-strain angle is 0°, 45° and 90° to the pre-strain axis.

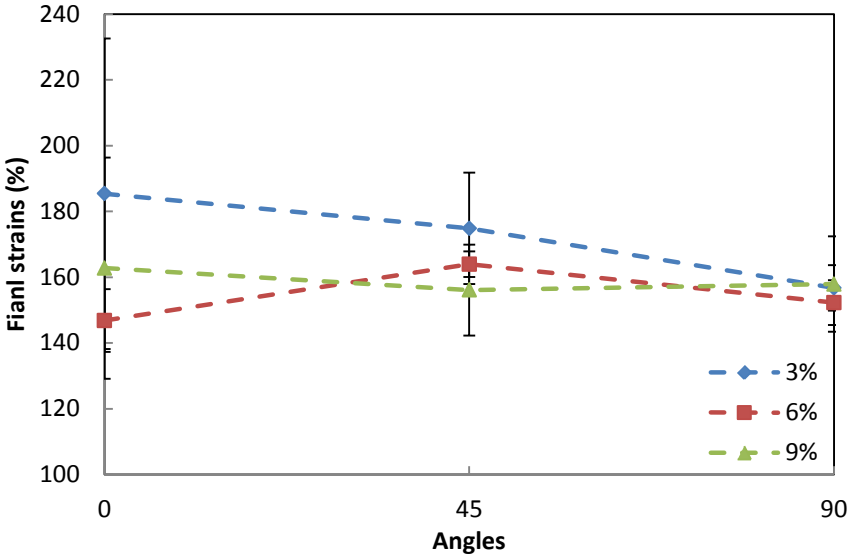

Figure 102. The average final strains at 0°, 45° and 90° to the pre-strain axis after various average pre-strains.

4.5 **Summary of experimental trends**

The main conclusions of the experimental results presented in this section are summarized below.

Table 12. The effect of pre-strain on the reloading yield stress.

Yield stress	**Angles**	**Pre-strains**	**Average value**	**Trend**
Reloading yield stress (σ_{be}) / MPa	0°	3%	111	The reloading yield stress increases with increasing pre-strains.
		6%	140	
		9%	149	
	45°	3%	107	
		6%	118	
		9%	121	
	90°	3%	116	
		6%	137	
		9%	138	
Reloading yield stress/ unloading stress (σ_{be}/σ_{un})	0°	3%	0.83	The reloading yield stress/ unloading stress decreases with increasing pre-strains except at 0º.
		6%	0.91	
		9%	0.83	
	45°	3%	0.97	
		6%	0.77	
		9%	0.71	
	90°	3%	0.87	
		6%	0.84	
		9%	0.8	
Reloading yield stress/reference stress (σ_{be}/σ_{r})	0°	3%	1.07	The Reloading yield stress/reference stress is highest at around 6% pre-strain except at 45º.
		6%	1.22	
		9%	1.13	
	45°	3%	1.08	
		6%	1.05	
		9%	0.95	
	90°	3%	1.14	
		6%	1.18	
		9%	1.1	

Table 13. The effect of strain path change angle on the reloading yield stress.

Yield stress	Pre-strains	Angles	Average value	Trend
Reloading yield stress (σ_{be}) / MPa	3%	0°	111	The smallest reloading yield stress is at 45º.
		45°	107	
		90°	116	
	6%	0°	140	
		45°	118	
		90°	137	
	9%	0°	149	
		45°	121	
		90°	138	
Reloading yield stress/ unloading stress (σ_{be}/σ_{un})	3%	0°	0.83	The smallest reloading yield stress/ unloading stress is at 45º.
		45°	0.79	
		90°	0.87	
	6%	0°	0.91	
		45°	0.77	
		90°	0.84	
	9%	0°	0.83	
		45°	0.71	
		90°	0.80	
Reloading yield stress/reference stress (σ_{be}/σ_{r})	3%	0°	1.07	The smallest reloading yield stress/ reference stress is at 45º.
		45°	1.08	
		90°	1.14	
	6%	0°	1.22	
		45°	1.05	
		90°	1.18	
	9%	0°	1.13	
		45°	0.95	
		90°	1.1	

Table 14. The effect of pre-strain on the work-hardening rate.

Work-hardening rate	Angles	Trends
Work-hardening rate (θ)	0°	The work-hardening rate after strain path change is higher than the one without pre-strain, and they are similar with various pre-strain.
	45°	The work-hardening rate is higher than the one of monotonic loading after strain path change with lower pre-strain, and it gets closer to the one without pre-strain with increasing pre-strain.
	90°	

Table 15. The effect of strain path change angle on the work-hardening rate.

Work-hardening rate	Pre-strains	Trends
Work-hardening rate (θ)	3%	Similar work-hardening rates are observed with similar pre-strains at 0°, 45° and 90°.
	6%	
	9%	

Table 16. The effect of pre-strain on UTS and effective necking strain.

Necking	Angles	Pre-strains	Average value	Trends
UTS (σ_{UTS})/MPa	0°	3%	200	The UTS is highest at around 3% pre-strain, and it decreases with increasing pre-strain except at 0º.
		6%	206	
		9%	213	
	45°	3%	218	
		6%	209	
		9%	184	
	90°	3%	209	
		6%	193	
		9%	181	
The total effective necking strain ($\varepsilon_{total\ necking}$)	0°	3%	32%	The total effective necking strain is highest at around 3% pre-strain, and it decreases with increasing pre-strain except at 0º.
		6%	29%	
		9%	33%	
	45°	3%	37%	
		6%	33%	
		9%	22%	
	90°	3%	32%	
		6%	26%	
		9%	21%	

Table 17. The effect of strain path change angle on UTS and effective necking strain

	Pre-strains	Angles	Average value	Trends
UTS (σ_{UTS})/MPa	3%	0°	200	The UTS is highest at 45° except for the one with 9% pre-strain.
		45°	218	
		90°	209	
	6%	0°	206	
		45°	209	
		90°	229	
	9%	0°	213	
		45°	193	
		90°	181	
The total effective necking strain ($\varepsilon_{total\ necking}$)	3%	0°	32%	The total effective necking strain is highest at 45° except for the one with 9% pre-strain.
		45°	37%	
		90°	32%	
	6%	0°	29%	
		45°	33%	
		90°	26%	
	9%	0°	33%	
		45°	22%	
		90°	21%	

Table 18. The effect of pre-strain on the final strain.

	Angles	Trends
Final strain (ε_f)	0°	The final strain after strain path change is higher than the one without pre-strain.
	45°	
	90°	

Table 19. The effect of strain path change angle on the final strain.

	Pre-strains	Trends
Final strain (ε_f)	3%	No obvious trends can be observed.
	6%	
	9%	

5 Discussion

5.1 Yield stress after strain path change

In Figure 69, higher yield stress in plane strain tension is observed compared to uniaxial tension during proportional loading. In a state of ideal plane strain, the strain in the transverse direction is equal to zero ($\varepsilon_{xx} = 0$), which causes a higher degree of plastic constraint (flow is constrained by the metal around the plastically deforming region), while deformation is less constrained in uniaxial tension. The plastic constraint makes it harder for the material to deform, and hence higher flow stresses are observed for plane strain tension. Wagoner and Laukonis [97] observed similar results on aluminum-killed steel samples, and Wunsch et al. [99] observed similar results during the simulation of plane strain tension of SiC particle reinforced aluminum composites. The much lower strains observed in our experiments in plane strain tension compared to uniaxial tension are mainly due to misalignment of the specimen in the grips, which resulted in a stress concentration at the fillet of the reduced section and thus early failure. The variations in yield stresses observed in the plane strain stress strain curves are due to strain distribution variations in the samples gauge length (see Figure 91 and 92).

As shown in Figure 73, with increasing pre-strain, the reloading yield stress increases. Also, the rate of increase of the reloading yield stress plateaus at around 6% pre-strain. With increasing pre-strain, the density of dislocations building up during pre-strain increases leaving a stronger long-range residual stress during unloading,

which helps to formation of dislocation cell during subsequent loading. Hence the reloading yield stress increases. Hasegawa et al.[44] indicated that local (residual) stresses are left in the dislocation substructure during unloading due to the polarization and memory of the tangled dislocation walls. Rao and Laukonis [19] reached the same conclusions. Also, with increasing pre-strain, the dislocation substructure created during pre-straining is becoming more stable. Less new slip systems can be activated during the subsequent loading and less dislocation can accumulate. As a result, the effect of pre-strain on the reloading yield stress is getting smaller at high pre-strains. Hasegawa et al. [44] observed that the dislocation density is increasing, and the dislocation substructure is becoming more stable with increasing strains.

After strain path change, the reloading yield stress is lower than the pre-strain unloading stress (see Figure 74). However, the reloading yield stress is generally higher than the stress in monotonic loading at a given pre-strain (see Figure 75). The lower reloading yield stress compared to the unloading stress is due to the higher flow stress observed in the plane strain tests (see Figure 69) as discussed earlier (see section 5.1). The pre-strain stage builds up a higher dislocation density, which leads to higher reloading yield stresses as compared to the stress in monotonic loading with equivalent pre-strain (see Figure 75). Rao and Laukonis [19] also observed similar results on aluminum-killed alloys.

Lower reloading yield stresses are observed at 45° and 90° after pre-straining in

uniaxial tension compared to the one at 0º with similar pre-strains (see Figure 76 and Figure 77). Also, a similar trend is observed for the reloading yield stress over unloading stress (see Figure 78) and the average normalized reloading stress σ_{be}/σ_r (see Figure 79). When the major slip system is changed during reloading, there is less interaction between the old slip systems, activated during the pre-strain stage, and the new one, activated during the subsequent loading, and thus the obstacles on the new primary plane are smaller. The dislocations can move more easily on the new slip systems, and the stress is therefore smaller. Wu et al. [100] observed similar results on AA6111. Basinski et al. [53], [54], [55] also reached the same conclusions; the stresses produced by the dislocations meeting the obstacles can be relieved by further slip on the far side of the obstacles. However, there is a significant hardening effect observed for orthogonal change of strain path for aluminum-killed steel and IF steel [19], [77]. This is may be due to the formation of microbands during cross-loading. For aluminum alloys, the dislocation substructure may be similar to the one formed during pre-strain. Barlat et al. [48] and Lopes et al. [47] observed similar dislocation substructure during uniaxial tension and cross-loading for AA10500-O.

5.2 **Work-hardening rate after strain path change**

When the strain path change angle is 0º, the work-hardening rate increases after strain path change when compared to the one without pre-strain (see Figure 80). As deformation proceeds, more slip systems are activated, and the orientation of these new slips systems changes at higher strains. With increasing density of slip systems,

the capacity to activate new slip systems decreases. In this case, the motion of dislocations is becoming more difficult. When the major slip system is changed because of strain path change, the obstacles for the motion of dislocations are relatively thin on the new primary plane. Hence the work-hardening rates increase after the strain path change. J.H. Schmitt et al. [50] observed the number of slip lines increase with increasing strains (see in Figure 14). New sets of slip lines can be observed during the sequential tensile test at the 45º and 90 º directions, and the number of new slip lines increases faster than the one without pre-strains (see in Figure 15 and 16).

When the strain path change angle is 45º and 90º (see Figure 81 and Figure 82), the work-hardening rate increases after strain path change at lower pre-strain as well. It decreases with increasing pre-strains, and it even gets closer to the one of monotonic loading at higher pre-strain. With increasing pre-strains, the number of active slips systems increases, and new slip systems with different orientation are activated. After strain path change, the major slip system is changed, and the work-hardening rate increases. However, at higher strain, the high dislocation density along with the formation of dislocation substructures results in a material whose dislocation structure is similar to that of the non-pre-strained material. Hence the work-hardening rate decreases to reach that of non-pre-strained samples. The effect of strain path change is thus weaker with increasing pre-strains. J.H. Schmitt et al. [50] observed one slip line direction is predominant at lower strains. The number of slip

lines increases, and new slip lines directions appear with increasing strains (see in Figure 14). New set of slip lines can be observed during the sequential tensile test at 45º and 90º (see Figure 15 and 16). As for the dislocation substructure, Barlat et al. [48] observed the transition of new dislocation substructures of AA1050 after the change in strain path at 45º and 90º without dissolution of the dislocation substructure formed during pre-strain which agrees with our explanation.

5.3 UTS and effective necking strain after strain path change

From the work-hardening rate (Figure 80 to 85), UTS (Figure 87 and 89) and effective necking strain (Figure 88 and 90), similar trends are observed. At 0º, the work-hardening rate after strain path change is higher than the one without pre-strain, and they are similar with pre-strains, while trends for the UTS and effective necking strain are similar. At 45º and 90º, the work-hardening rate is also higher than the one of monotonic loading after strain path change with lower pre-strain, and it decreases with increasing pre-strain. The UTS and effective necking strain at 45º and 90º are higher than the one without pre-strain, and they decrease with increasing pre-strain.

As mentioned in 4.2.6, the onset of necking is defined as intersection of true stress strain curve and the work-hardening rate θ ($=^{d\sigma}/_{d\varepsilon}$) curve, which leads to the equation as below.

$$\theta = {}^{d\sigma}/_{d\varepsilon} = \sigma \qquad \text{(Equation 5-1)}$$

From the Hollomon equation (Equation 2-2), one can get

$$\theta = {d\sigma}/{d\varepsilon} = \sigma = K\varepsilon^n \qquad \text{(Equation 5-2)}$$

where n and K are constant. Hence, higher work-hardening rate leads to the higher UTS and effective necking strain. G. E. Dieter [72] has a similar explanation. Also, Zhao et al. [101] indicated that higher work-hardening rate is good for uniform elongation because it can help delay localized deformation (necking) under tensile stress.

5.4 **Strain distributions**

The stain distributions for the plane strain specimens at similar strains are different (see Figure 91 (j), 92 (a), 92 (b), and (c)). This is because the strain distributions rely on how well the grips were tightened and how well the sample was aligned in the grips.

There are no significant differences in the strain distributions for the uniaxial tensile specimen and that of the uniaxial specimens after strain path change (see Figure 93 to 98). This is due to the reduction in the gauge width which creates a stress concentration and forces all deformations to take place in middle of the gauge length.

5.5 **Facture surface**

From Figure 101, the final strain after strain path change is higher than the one without pre-strain. However, after strain path change, no obvious trend can be observed neither regarding the various pre-strains (see Figure 101) nor regarding strain path change angles (see Figure 102). This suggests that pre-straining the sample

does not significantly affect the true failure strains, *i.e.* the ductility in the sample.

6 Conclusions and Recommendations for Future work

The main conclusions presented in this thesis are listed below:

- The flow stress in plane strain tensile tests is higher than the one in uniaxial tensile test. This is probably because the strain in the transverse direction is equal to zero for plane strain tension which causes a higher degree of plastic constraints.
- The reloading yield stress increases with increasing pre-strains, which is due to an increase in the dislocation density.
- The reloading yield stress is lower than the unloading stress during pre-strain due to the flow stress during pre-strain (plane strain tension) being higher than the one in reloading uniaxial tensile test.
- The reloading yield stress is higher than the stress under monotonic loading with equivalent pre-strain. This may be because a higher dislocation density is built during pre-strain leaving a long-range residual stress during unloading.
- The reloading yield stress when the strain path change angle is 0° is higher than that of 45° and 90°, which is probably because the barrier for the motion of dislocation is relatively thinner after the major slip system changed.
- Pre-straining causes the work-hardening rate to increase. This may be because the capacity to store the dislocation on the new slip primary plane increases

after the major slip system has changed.

- The higher work-hardening rate after strain path change leads to higher UTS and effective necking strain.
- The strain distributions of the plane strain specimen depend on the tightening of the grips and alignment of the sample. There are no significant differences between the strain distributions in uniaxial tensile specimens before strain path change and those after strain path change due to the geometry of the specimen which forces deformation to take place in the middle of the gauge length.

Below are a few directions for future work in this field:

- TEM should be used at different levels of deformation to observe the dislocation substructure and the activation of slip systems, which would validate the explanations given in this work.
- Finite element analyses could be carried out to model the mechanical response after strain path change and to predict the effect of strain path change on deformation and fracture.

7 References

[1] J. R. Davis, *Aluminum and Aluminum Alloys*. ASM International, 1993.

[2] J. G. Kaufman, *Introduction to Aluminum Alloys and Tempers*. ASM International, 2000.

[3] X.-M. Cheng, “Earing behavior and crystallographic texture of aluminum alloys during cold rolling,” *J. of Materi Eng and Perform*, vol. 10, no. 4, pp. 399–404, Aug. 2001.

[4] Q. Liu, Z. Yao, A. Godfrey, and W. Liu, “Effect of particles on microstructural evolution during cold rolling of the aluminum alloy AA3104,” *Journal of Alloys and Compounds*, vol. 482, no. 1–2, pp. 264–271, Aug. 2009.

[5] Z. Yao, G. Huang, A. Godfrey, W. Liu, and Q. Liu, “Dislocation Boundary Structure from Low to Medium Strain of Cold Rolling AA3104 Aluminum Alloy,” *Metall and Mat Trans A*, vol. 40, no. 6, pp. 1487–1497, Jun. 2009.

[6] P. D. Wu, M. Jain, J. Savoie, S. R. MacEwen, P. Tuğcu, and K. W. Neale, “Evaluation of anisotropic yield functions for aluminum sheets,” *International Journal of Plasticity*, vol. 19, no. 1, pp. 121–138, Jan. 2003.

[7] A. S. Korhonen and E. Heikinheimo, “Forming and fracture limits of aluminium alloy,” *Materials Science and Technology*, vol. 27, no. 11, pp. 1694–1700, 2011.

[8] A. S. Korhonen, “On the Work-Hardening of AA 3104-H19 Aluminum Alloy,” *J. of Materi Eng and Perform*, pp. 1–7.

[9] J. H. Schmitt, E. Aernoudt, and B. Baudelet, “Yield loci for polycrystalline metals without texture,” *Materials Science and Engineering*, vol. 75, no. 1–2, pp. 13–20, Nov. 1985.

[10] N. A. Sakharova, J. V. Fernandes, and M. F. Vieira, “Strain path and work-hardening behavior of brass,” *Materials Science and Engineering: A*, vol. 507, no. 1–2, pp. 13–21, May 2009.

[11] E. V. Nesterova, B. Bacroix, and C. Teodosiu, “Microstructure and texture evolution under strain-path changes in low-carbon interstitial-free steel,” *Metall and Mat Trans A*, vol. 32, no. 10, pp. 2527–2538, Oct. 2001.

[12] X. Liu, G. He, X. Ding, D. Mo, and W. Zhang, “Fatigue behavior and dislocation substructures for 6063 aluminum alloy under nonproportional loadings,” *International Journal of Fatigue*, vol. 31, no. 7, pp. 1190–1195, Jul. 2009.

[13] N. A. Sakharova and J. V. Fernandes, “Strain path change effect on dislocation microstructure of multicrystalline copper sheets,” *Materials Chemistry and Physics*, vol. 98, no. 1, pp. 44–50, Jul. 2006.

[14] G. Vincze, E. F. Rauch, J. J. Gracio, F. Barlat, and A. B. Lopes, “A comparison of the mechanical behaviour of an AA1050 and a low carbon steel deformed upon strain reversal,” *Acta Materialia*, vol. 53, no. 4, pp. 1005–1013, Feb. 2005.

[15] H. Paul, C. Maurice, and J. H. Driver, “Microstructure and microtexture evolution during strain path changes of an initially stable Cu single crystal,” *Acta Materialia*, vol. 58, no. 8, pp. 2799–2813, May 2010.

[16] A. K. Ghosh and W. A. Backofen, “Strain hardening and instability in biaxially streched sheets,” *MT*, vol. 4, no. 4, pp. 1113–1123, Apr. 1973.
[17] A. J. Ranta-Eskola, “Effect of loading path on stressstrain relationships of sheet steel and brass,” *Metals Technology*, vol. 7, no. 1, pp. 45–49, 1980.
[18] R. H. Wagoner and J. V. Laukonis, “Plastic behavior of aluminum-killed steel following plane-strain deformation,” *Metallurgical Transactions A*, vol. 14A, no. 2, pp. 1487–1495, Jul. 1983.
[19] B. V. N. Rao and J. V. Laukonis, “Microstructural mechanism for the anomalous tensile behavior of aluminum-killed steel prestrained in plane strain tension,” *Materials Science and Engineering*, vol. 60, no. 2, pp. 125–135, Aug. 1983.
[20] S. P. Keeler, *Plastic Instability and Fracture in Sheets Stretched Over Rigid Punches*. MIT, 1961.
[21] J. V. Laukonis and A. K. Ghosh, “Effects of strain path changes on the formability of sheet metals,” *MTA*, vol. 9, no. 12, pp. 1849–1856, Dec. 1978.
[22] W. . Hutchinson, R. Arthey, and P. Malmström, “On anomalously low work-hardening in pre-strained metals,” *Scripta Metallurgica*, vol. 10, no. 8, pp. 673–675, Aug. 1976.
[23] D. J. Lloyd and H. Sang, “The influence of strain path on subsequent mechanical properties—Orthogonal tensile paths,” *MTA*, vol. 10, no. 11, pp. 1767–1772, Nov. 1979.
[24] T. Yalcinkaya, W. A. M. Brekelmans, and M. G. D. Geers, “A composite dislocation cell model to describe strain path change effects in BCC metals,” *Modelling and Simulation in Materials Science and Engineering*, vol. 17, no. 6, p. 064008, Sep. 2009.
[25] B. Peeters, M. Seefeldt, C. Teodosiu, S. R. Kalidindi, P. Van Houtte, and E. Aernoudt, “Work-hardening/softening behaviour of b.c.c. polycrystals during changing strain paths: I. An integrated model based on substructure and texture evolution, and its prediction of the stress–strain behaviour of an IF steel during two-stage strain paths,” *Acta Materialia*, vol. 49, no. 9, pp. 1607–1619, May 2001.
[26] J. J. Gracio, A. . Lopes, and E. . Rauch, “Analysis of plastic instability in commercially pure Al alloys,” *Journal of Materials Processing Technology*, vol. 103, no. 1, pp. 160–164, Jun. 2000.
[27] S. Suwas and N. P. Gurao, “Crystallographic texture in Materials,” *Journal of the Indian Institute of Science*, vol. 88, no. 2, pp. 151–177, Dec. 2012.
[28] N. P. Gurao, S. Sethuraman, and S. Suwas, “Effect of strain path change on the evolution of texture and microstructure during rolling of copper and nickel,” *Materials Science and Engineering: A*, vol. 528, no. 25–26, pp. 7739–7750, Sep. 2011.
[29] N. Jia, P. Eisenlohr, F. Roters, D. Raabe, and X. Zhao, “Orientation dependence of shear banding in face-centered-cubic single crystals,” *Acta Materialia*, vol. 60, no. 8, pp. 3415–3434, May 2012.

[30] I. L. Dillamore, “Occurrence of shear bands in heavily rolled cubic metals,” *Metal Science*, vol. 13, no. 2, pp. 73–77, Feb. 1979.
[31] J. Gil Sevillano, P. van Houtte, and E. Aernoudt, “Large strain work-hardening and textures,” *Progress in Materials Science*, vol. 25, no. 2–4, pp. 69–134, 1980.
[32] P. Van Houtte, J. G. Sevillarno, and E. Aernoudt, “MODELS FOR SHEAR BAND FORMATION IN ROLLING AND EXTRUSION.,” *Zeitschrift fuer Metallkunde/Materials Research and Advanced Techniques*, vol. 70, no. 7, pp. 426–432, 1979.
[33] S. Mahesh, “Deformation banding and shear banding in single crystals,” *Acta Materialia*, vol. 54, no. 17, pp. 4565–4574, Oct. 2006.
[34] H. Paul, J. . Driver, C. Maurice, and Z. Jasieński, “Shear band microtexture formation in twinned face centred cubic single crystals,” *Materials Science and Engineering: A*, vol. 359, no. 1–2, pp. 178–191, Oct. 2003.
[35] C. H. Cáceres and P. Lukáč, “Strain hardening behaviour and the Taylor factor of pure magnesium,” *Philosophical Magazine*, vol. 88, no. 7, pp. 977–989, 2008.
[36] A. Korbel and M. Richert, “Formation of shear bands during cyclic deformation of aluminium,” *Acta Metallurgica*, vol. 33, no. 11, pp. 1971–1978, Nov. 1985.
[37] M. K. Wong, W. P. Kao, J. T. Lui, C. P. Chang, and P. W. Kao, “Cyclic deformation of ultrafine-grained aluminum,” *Acta Materialia*, vol. 55, no. 2, pp. 715–725, Jan. 2007.
[38] X. Huang and N. Hansen, “Grain orientation dependence of microstructure in aluminium deformed in tension,” *Scripta Materialia*, vol. 37, no. 1, pp. 1–7, Jul. 1997.
[39] X. Huang, “Grain Orientation Effect on Microstructure in Tensile Strained Copper,” *Scripta Materialia*, vol. 38, no. 11, pp. 1697–1703, May 1998.
[40] F. Li and P. S. Bate, “Strain path change effects in cube textured aluminium sheet,” *Acta Metallurgica et Materialia*, vol. 39, no. 11, pp. 2639–2650, Nov. 1991.
[41] B. Bacroix and Z. Hu, “Texture evolution induced by strain path changes in low carbon steel sheets,” *MMTA*, vol. 26, no. 3, pp. 601–613, Mar. 1995.
[42] J. T. Fourie, P. J. Jackson, D. Kuhlmann-Wilsdorf, D. A. Rigney, J. H. van der Merwe, and H. G. F. Wilsdorf, “Nomenclature for dislocation arrays,” *Scripta Metallurgica*, vol. 16, no. 2, pp. 157–160, Feb. 1982.
[43] E. . Rauch and J.-H. Schmitt, “Dislocation substructures in mild steel deformed in simple shear,” *Materials Science and Engineering: A*, vol. 113, pp. 441–448, Jul. 1989.
[44] T. Hasegawa, T. Yakou, and U. F. Kocks, “Forward and reverse rearrangements of dislocations in tangled walls,” *Materials Science and Engineering*, vol. 81, no. 0, pp. 189–199, Aug. 1986.
[45] B. Gardey, S. Bouvier, V. Richard, and B. Bacroix, “Texture and dislocation structures observation in a dual-phase steel under strain-path changes at large deformation,” *Materials Science and Engineering: A*, vol. 400–401, no. 0, pp. 136–141, Jul. 2005.

[46] T. Hasegawa, T. Yakou, and S. Karashima, “Deformation behaviour and dislocation structures upon stress reversal in polycrystalline aluminium,” *Materials Science and Engineering*, vol. 20, no. 0, pp. 267–276, 1975.

[47] A. B. Lopes, F. Barlat, J. J. Gracio, J. F. Ferreira Duarte, and E. F. Rauch, “Effect of texture and microstructure on strain hardening anisotropy for aluminum deformed in uniaxial tension and simple shear,” *International Journal of Plasticity*, vol. 19, no. 1, pp. 1–22, Jan. 2003.

[48] F. Barlat, J. M. Ferreira Duarte, J. J. Gracio, A. B. Lopes, and E. F. Rauch, “Plastic flow for non-monotonic loading conditions of an aluminum alloy sheet sample,” *International Journal of Plasticity*, vol. 19, no. 8, pp. 1215–1244, Aug. 2003.

[49] E. M. Viatkina, W. A. M. Brekelmans, and M. G. D. Geers, “The role of plastic slip anisotropy in the modelling of strain path change effects,” *Journal of Materials Processing Technology*, vol. 209, no. 1, pp. 186–193, Jan. 2009.

[50] J. H. Schmitt, J. V. Fernandes, J. J. Gracio, M. F. Vieira, and M. F. Vieira, “Plastic behaviour of copper sheets during sequential tension tests,” *Materials Science and Engineering: A*, vol. 147, no. 2, pp. 143–154, Nov. 1991.

[51] J. L. Bassani, K. Ito, and V. Vitek, “Complex macroscopic plastic flow arising from non-planar dislocation core structures,” *Materials Science and Engineering: A*, vol. 319–321, pp. 97–101, Dec. 2001.

[52] J. V. Sharp and M. J. Makin, “Slip behavior in copper crystals previously deformed on another slip system,” *Canadian Journal of Physics*, vol. 45, no. 2, pp. 519–522, Feb. 1967.

[53] Z. S. Basinski and P. J. Jackson, “THE EFFECT OF EXTRANEOUS DEFORMATION ON STRAIN HARDENING IN Cu SINGLE CRYSTALS,” *Applied Physics Letters*, vol. 6, no. 8, pp. 148–150, Apr. 1965.

[54] Z. S. Basinski and P. J. Jackson, “The Instability of the Work Hardened State. I. Slip in Extraneously Deformed Crystals,” *physica status solidi (b)*, vol. 9, no. 3, pp. 805–823, 1965.

[55] Z. S. Basinski and P. J. Jackson, “The Instability of the Work Hardened State. II. Slip in ‘Alien’ Dislocation Distributions,” *physica status solidi (b)*, vol. 10, no. 1, pp. 45–56, 1965.

[56] J. H. Schmitt, E. Aernoudt, and B. Baudelet, “Yield loci for polycrystalline metals without texture,” *Materials Science and Engineering*, vol. 75, no. 1–2, pp. 13–20, Nov. 1985.

[57] C. Tome, G. R. Canova, U. F. Kocks, N. Christodoulou, and J. J. Jonas, “The relation between macroscopic and microscopic strain hardening in F.C.C. polycrystals,” *Acta Metallurgica*, vol. 32, no. 10, pp. 1637–1653, Oct. 1984.

[58] J. L. Raphanel, J.-H. Schmitt, and B. Baudelet, “Effect of a prestrain on the subsequent yielding of low carbon steel sheets: experiments and simulations,” *International Journal of Plasticity*, vol. 2, no. 4, pp. 371–378, 1986.

[59] S. H. A. Boers, P. J. G. Schreurs, M. G. D. Geers, V. Levkovitch, J. Wang, and B.

Svendsen, “Experimental characterization and model identification of directional hardening effects in metals for complex strain path changes,” *International Journal of Solids and Structures*, vol. 47, no. 10, pp. 1361–1374, May 2010.

[60] B. Gardey, S. Bouvier, V. Richard, and B. Bacroix, “Texture and dislocation structures observation in a dual-phase steel under strain-path changes at large deformation,” *Materials Science and Engineering: A*, vol. 400–401, no. 0, pp. 136–141, Jul. 2005.

[61] D. V. Wilson, M. Zandrahimi, and W. T. Roberts, “Effects of changes in strain path on work-hardening in CP aluminium and an Al-Cu-Mg alloy,” *Acta Metallurgica et Materialia*, vol. 38, no. 2, pp. 215–226, Feb. 1990.

[62] M. Zandrahimi, S. Platias, D. Frice, D. Barrett, P. S. Bate, and W. T. Roberts, “Effects of changes in strain path on work-hardening in cubic metals,” *MTA*, vol. 20, no. 11, pp. 2471–2482, Nov. 1989.

[63] S. Hiwatashi, A. Van Bael, P. an Houtte, and C. Teodosiu, “Prediction of forming limit strains under strain-path changes: Application of an anisotropic model based on texture and dislocation structure,” *International Journal of Plasticity*, vol. 14, no. 7, pp. 647–669, 1998.

[64] A. Graf and W. Hosford, “Effect of changing strain paths on,” *MTA*, vol. 24, no. 11, pp. 2503–2512, Nov. 1993.

[65] Z. Marciniak and K. Kuczyński, “Limit strains in the processes of stretch-forming sheet metal,” *International Journal of Mechanical Sciences*, vol. 9, no. 9, pp. 609–620, Sep. 1967.

[66] M. Symposium on Formability: Analysis, H. L. Gegel, S. S. Hecker, A. K. Ghosh, Metallurgical Society of AIME. Shaping and Forming Committee, and American Society of Metals. Flow and Fracture Committee, “Formability: analysis, modeling and experimentation : Proceedings of a symposium held in Chicago, Ill., October 24 and 25, 1977,” 1978.

[67] J. V. Laukonis, “Anisotropic strain localization in tensile prestrained sheet steel,” *MTA*, vol. 12, no. 3, pp. 467–472, Mar. 1981.

[68] D. Chae, J. . Bandstra, and D. . Koss, “The effect of pre-strain and strain-path changes on ductile fracture: experiment and computational modeling,” *Materials Science and Engineering: A*, vol. 285, no. 1–2, pp. 165–171, Jun. 2000.

[69] T. L. Anderson, *Fracture Mechanics: Fundamentals and Applications, Second Edition*. CRC PressINC, 1995.

[70] K. Enami, “The effects of compressive and tensile prestrain on ductile fracture initiation in steels,” *Engineering Fracture Mechanics*, vol. 72, no. 7, pp. 1089–1105, May 2005.

[71] A. C. Mackenzie, J. W. Hancock, and D. K. Brown, “On the influence of state of stress on ductile failure initiation in high strength steels,” *Engineering Fracture Mechanics*, vol. 9, no. 1, pp. 167–188, 1977.

[72] G. E. Dieter, *Mechanical metallurgy.* New York,, 1961.

[73] J. Arndt, H. Majedi, and W. Dahl, “Influence of Strain History on Ductile Failure

of Steel," *Le Journal de Physique IV*, vol. 06, no. C6, pp. C6–23–C6–32, Oct. 1996.

[74] Z. Marciniak and K. Kuczyński, "Limit strains in the processes of stretch-forming sheet metal," *International Journal of Mechanical Sciences*, vol. 9, no. 9, pp. 609–620, Sep. 1967.

[75] M. Azrin and W. A. Backofen, "The deformation and failure of a biaxially stretched sheet," *MT*, vol. 1, no. 10, pp. 2857–2865, Oct. 1970.

[76] D. Banabic, "A review on recent developments of Marciniak-Kuczynski model," *Computer Methods in Materials Science*, vol. Vol. 10, No. 4, pp. 225–237, 2010.

[77] C. Teodosiu and Z. Hu, "Evolution of the intragranular microstructure at moderate and large strains: Modelling and computational significance," *Simultaion of Material Processing: Theory, Methods and Applications, Shen & Dawson (eds)*, pp. 173–182, 1995.

[78] S. Mahesh, C. N. Tomé, R. J. McCabe, G. C. Kaschner, A. Misra, and I. J. Beyerlein, "Application of a substructure-based hardening model to copper under loading path changes," *Metall and Mat Trans A*, vol. 35, no. 12, pp. 3763–3774, Dec. 2004.

[79] B. Peeters, B. Bacroix, C. Teodosiu, P. Van Houtte, and E. Aernoudt, "Work-hardening/softening behaviour of b.c.c. polycrystals during changing strain:: Part II. TEM observations of dislocation sheets in an IF steel during two-stage strain paths and their representation in terms of dislocation densities," *Acta Materialia*, vol. 49, no. 9, pp. 1621–1632, May 2001.

[80] H. Mughrabi, "The long-range internal stress field in the dislocation wall structure of persistent slip bands," *physica status solidi (a)*, vol. 104, no. 1, pp. 107–120, 1987.

[81] E. M. Viatkina, W. a. M. Brekelmans, and M. G. D. Geers, "Numerical analysis of strain path dependency in FCC metals," *Comput Mech*, vol. 41, no. 3, pp. 391–405, Feb. 2008.

[82] J. Fajoui, D. Gloaguen, B. Courant, and R. Guillén, "Micromechanical modelling of the elastoplastic behaviour of metallic material under strain-path changes," *Comput Mech*, vol. 44, no. 2, pp. 285–296, Jul. 2009.

[83] F. K. G. Odqvist, "Die Verfestigung von flußeisenähnlichen Körpern. Ein Beitrag zur Plastizitätstheorie," *ZAMM - Journal of Applied Mathematics and Mechanics / Zeitschrift für Angewandte Mathematik und Mechanik*, vol. 13, no. 5, pp. 360–363, 1933.

[84] O. U. Colak, "Kinematic hardening rules for modeling uniaxial and multiaxial ratcheting," *Materials & Design*, vol. 29, no. 8, pp. 1575–1581, 2008.

[85] E. Melan, "Zur Plastizität des räumlichen Kontinuums," *Ing. Arch*, vol. 9, no. 2, pp. 116–126, Apr. 1938.

[86] W. Prager, B. U. D. of A. Mathematics, U. S. O. of N. Research, and U. S. N. D. B. of Ships, *A New Method of Analyzing Stresses and Strains in Work-hardening Plastic Solids*. Division of Applied Mathematics, Brown University, 1955.

[87] H. Ziegler, *A modification of Prager's hardening rule*. 1959.
[88] C. O. Frederick and P. J. Armstrong, "A mathematical representation of the multiaxial Bauschinger effect," *Materials at High Temperatures*, vol. 24, no. 1, pp. 1–26, 2007.
[89] M. Jirasek and Z. P. Bazant, *Inelastic Analysis of Structures*. John Wiley & Sons, 2002.
[90] Ansar Ali and Dr. Srinivasa Gopal, "Suitability of Indigenous Aluminium Cans as an Alternative to Tin Cans for Fish Canning and Process Time Evaluation," Cochin University of Science and Technology, India, 2004.
[91] W. H. Peters, W. F. Ranson, M. A. Sutton, T. C. Chu, and J. Anderson, "Application Of Digital Correlation Methods To Rigid Body Mechanics," *Opt. Eng*, vol. 22, no. 6, pp. 226738–226738, Dec. 1983.
[92] M. Sutton, W. Wolters, W. Peters, W. Ranson, and S. McNeill, "Determination of displacements using an improved digital correlation method," *Image and Vision Computing*, vol. 1, no. 3, pp. 133–139, Aug. 1983.
[93] W. H. Peters and W. F. Ranson, "Digital Imaging Techniques In Experimental Stress Analysis," *Opt. Eng*, vol. 21, no. 3, pp. 213427–213427, Jun. 1982.
[94] U. Emekli and A. C. West, "Electrochemical Nucleation of Copper: The Effect of Poly(ethylene glycol)," *J. Electrochem. Soc.*, vol. 157, no. 5, pp. D257–D263, May 2010.
[95] S. Holmberg, B. Enquist, and P. Thilderkvist, "Evaluation of sheet metal formability by tensile tests," *Journal of Materials Processing Technology*, vol. 145, no. 1, pp. 72–83, Jan. 2004.
[96] F. Taha, A. Graf, and W. Hosford, "Plane-Strain Tension Tests on Aluminum Alloy Sheet," *J. Eng. Mater. Technol.*, vol. 117, no. 2, pp. 168–171, Apr. 1995.
[97] R. H. Wagoner and J. V. Laukonis, "Plastic behavior of aluminum-killed steel following plane-strain deformation," *MTA*, vol. 14, no. 7, pp. 1487–1495, Jul. 1983.
[98] "Mechanical Properties - Springer," .
[99] B.Wunsch and N.Chawla, "Serial sectioning for 3D visualizatin and modeling of SiC particle reinforced aluminum composites," *The Mineral, Metals and Materials Society*.
[100] P. D. Wu, S. R. MacEwen, D. J. Lloyd, M. Jain, P. Tugcu, and K. W. Neale, "On pre-straining and the evolution of material anisotropy in sheet metals," *International Journal of Plasticity*, vol. 21, no. 4, pp. 723–739, Apr. 2005.
[101] Y. H. Zhao, X. Z. Liao, S. Cheng, E. Ma, and Y. T. Zhu, "Simultaneously Increasing the Ductility and Strength of Nanostructured Alloys," *Adv. Mater.*, vol. 18, no. 17, pp. 2280–2283, Sep. 2006.

Appendix A: Yield stress, young's modulus, UTS, total effective necking strain, and final strain

Table 20. Pre-strain, reloading yield stress, reference stress, reloading young's modulus, UTS, total effective necking strain and final strain of strain path change specimens at 0°.

Specimen	Pre-strain (%)	Necking in pre-strain	Reloading yield stress (MPa)	Reference stress (MPa)	UTS (MPa)	Total Effective necking strain (%)	Final strain (%)
P3_0_S2	4.2	N	104	103	205	33	138.2
P3_0_S3	4.2	N	117	103	195	31	232.6
P6_0_S1	6.0	N	141	113	200	27	145.0
P6_0_S2	6.8	N	144	116	195	26	164.1
P6_0_S3	6.9	N	136	116	222	35	131.3
P9_0_S2	8.9	N	157	125	222	36	196.4
P9_0_S3	15.3	Y	140	140	194	30	129.1

Table 21. Pre-strain, reloading yield stress, reference stress, reloading young's modulus, UTS, total effective necking strain and final strain of strain path change specimens at 45°.

Specimen	Pre-strain (%)	Necking in Pre-strain	Reloading yield stress (MPa)	Reference stress (MPa)	UTS (MPa)	Total Effective necking strain (%)	Final strain (%)
P3_45_S1	3.6	N	106	100	236	42	143.8
P3_45_S2	3.46	N	106	98	213	37	178.5
P3_45_S3	3.6	N	100	127.4	204	31	202.1
P6_45_S2	4.7	N	114	107	204	30	146.5
P6_45_S3	7.4	N	122	119	214	35	138.7
P9_45_S1	12.5	Y	128	134	175	21	168.8
P9_45_S2	8.5	Y	122	124	181	23	171.0
P9_45_S3	9.3	Y	114	126	196	28	128.5

Table 22. Pre-strain, reloading yield stress, reference stress, reloading young's modulus, UTS, total effective necking strain and final strain of strain path change specimens at 90°.

Specimen	Pre-strain (%)	Necking in pre-strain	Reloading yield stress (MPa)	Reference stress (MPa)	UTS (MPa)	Total Effective necking strain (%)	Final strain (%)
P3_90_S1	3.7	N	122	101	217	35	143.3
P3_90_S2	3.8	N	122	102	202	27	161.1
P3_90_S3	4.3	N	104	104	206	34	165.9
P6_90_S1	5.4	N	133	111	203	30	154.7
P6_90_S2	6.3	N	137	116	197	27	159.6
P6_90_S3	7.7	N	141	120	178	21	177.1
P9_90_S2	8.6	N	132	124	177	22	133.8
P9_90_S3	9.8	Y	144	127	185	21	162.8

Appendix B: True stress strain curve

This appendix contains more graphs that show the all the true stress strain curve of the strain path change samples tested.

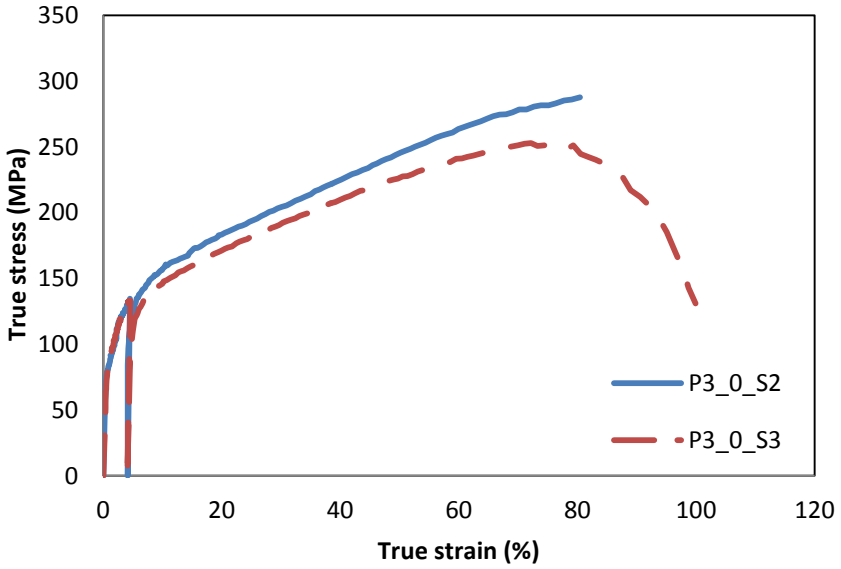

Figure 103. The reloading true stress-strain curve at around 3% pre-strains at 0° to RD directions.

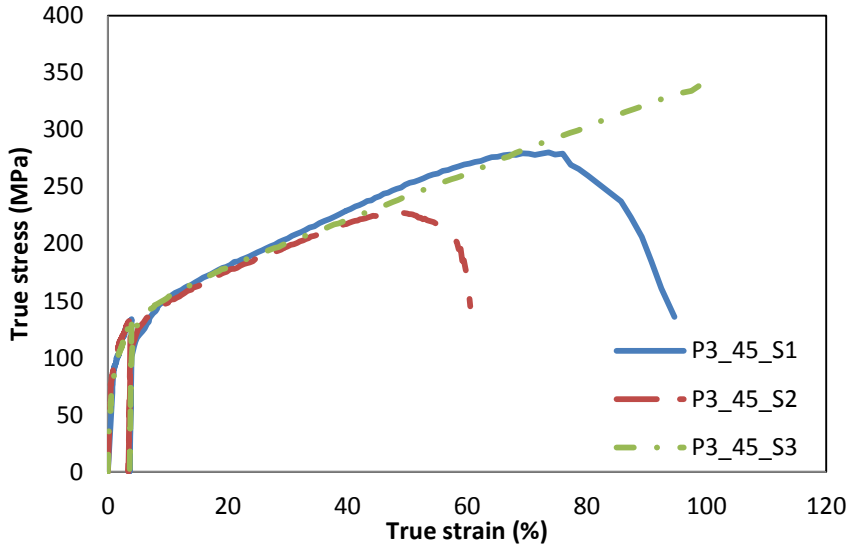

Figure 104. The reloading true stress-strain curve at around 3% pre-strains at 45° to RD directions.

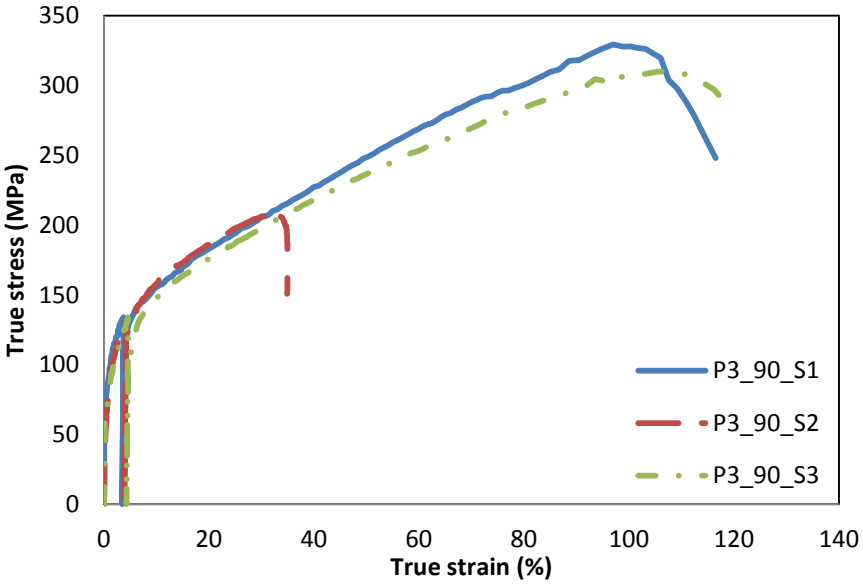

Figure 105. The reloading true stress-strain curve at around 3% pre-strains at 90° to RD directions.

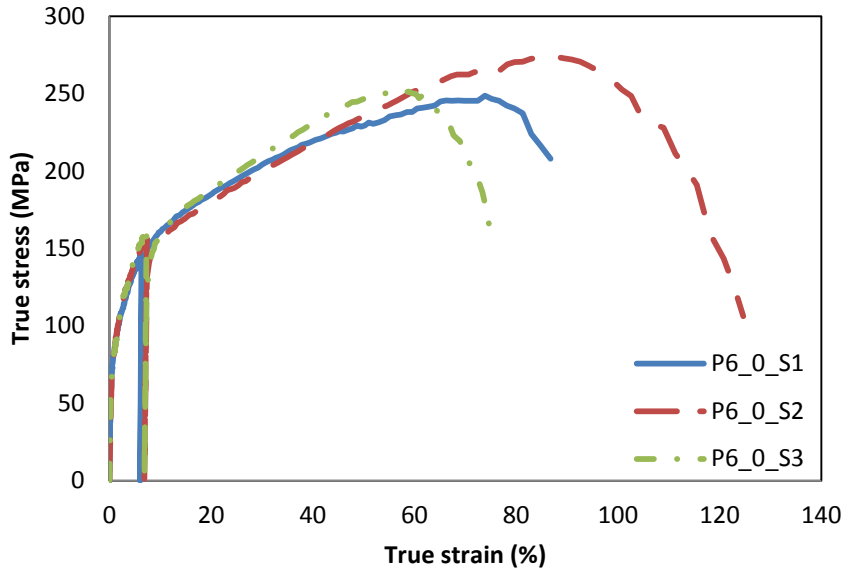

Figure 106. The reloading true stress-strain curve at around 6% pre-strains at 0° to RD directions.

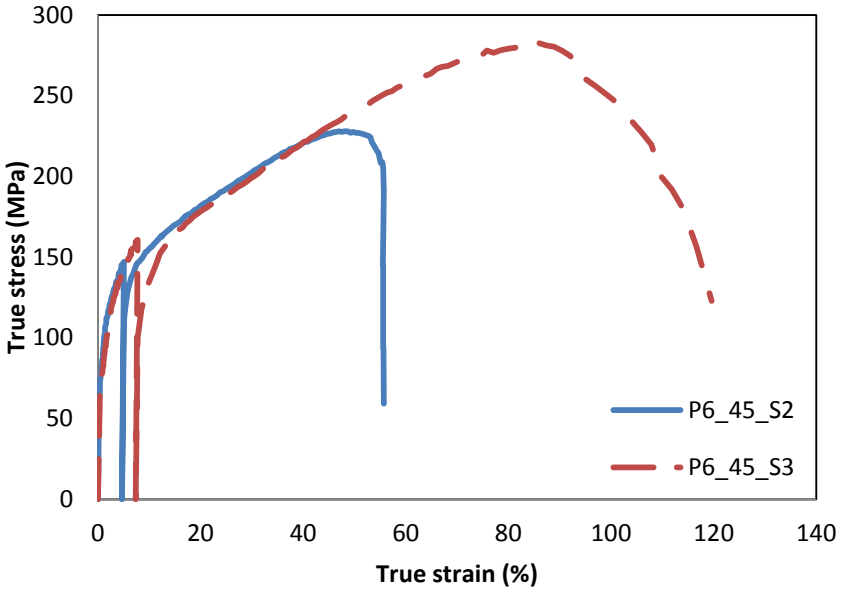

Figure 107. The reloading true stress-strain curve at around 6% pre-strains at 45° to RD directions.

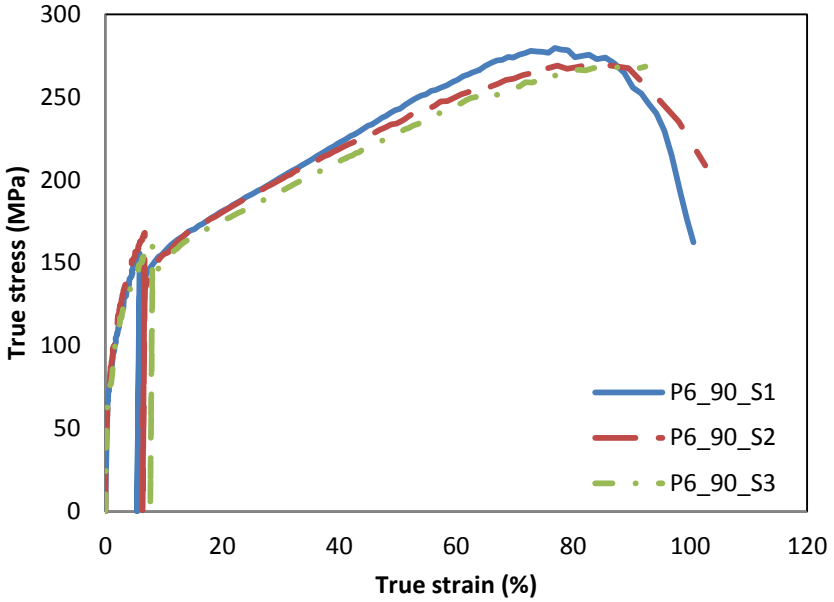

Figure 108. The reloading true stress-strain curve at around 6% pre-strains at 90° to RD directions.

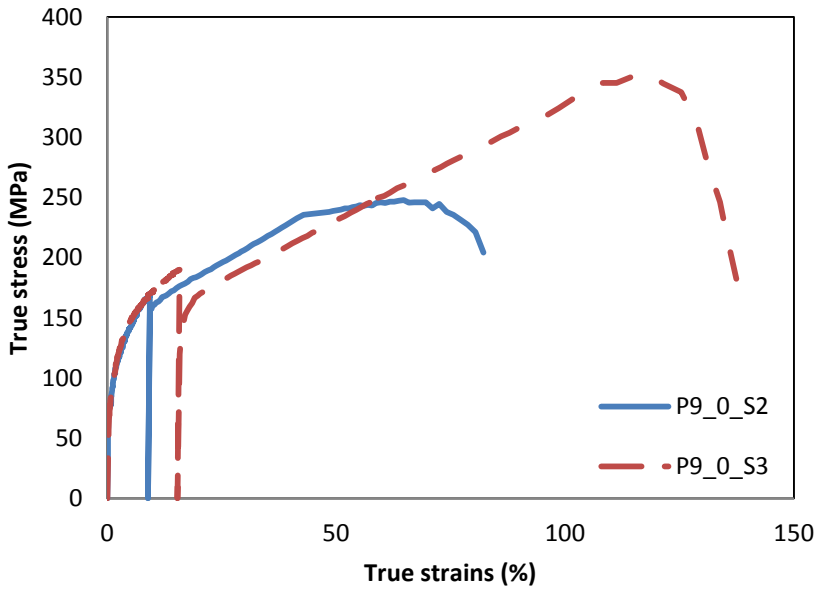

Figure 109. The reloading true stress-strain curve at around 9% pre-strains at 0° to RD directions.

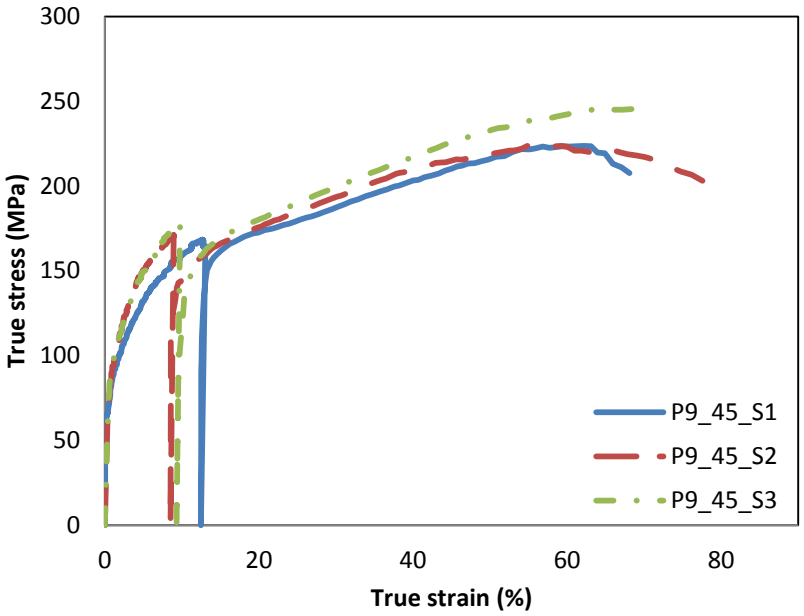

Figure 110. The reloading true stress-strain curve at around 9% pre-strains at 45° to RD directions.

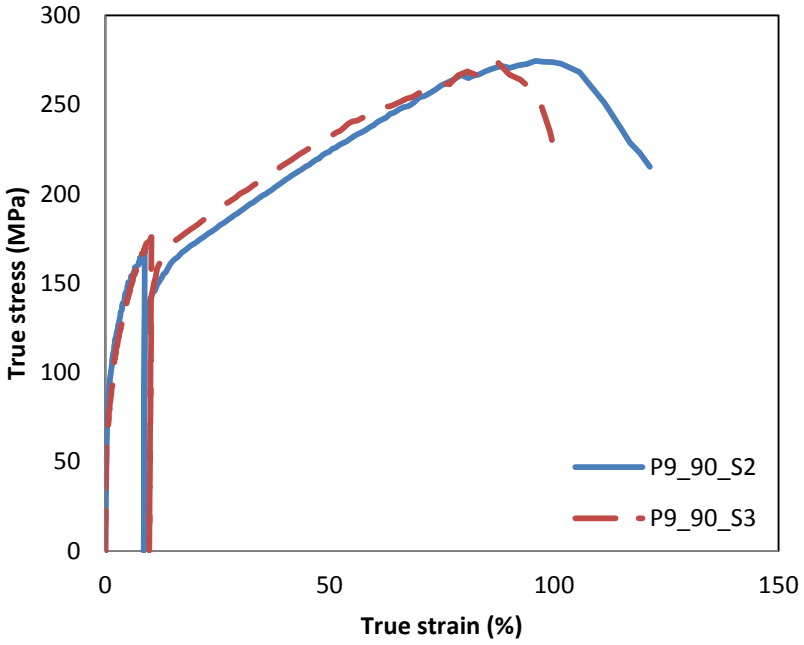

Figure 111. The reloading true stress-strain curve at around 9% pre-strains at 90° to RD directions.

Appendix C: Strain distribution after strain path change

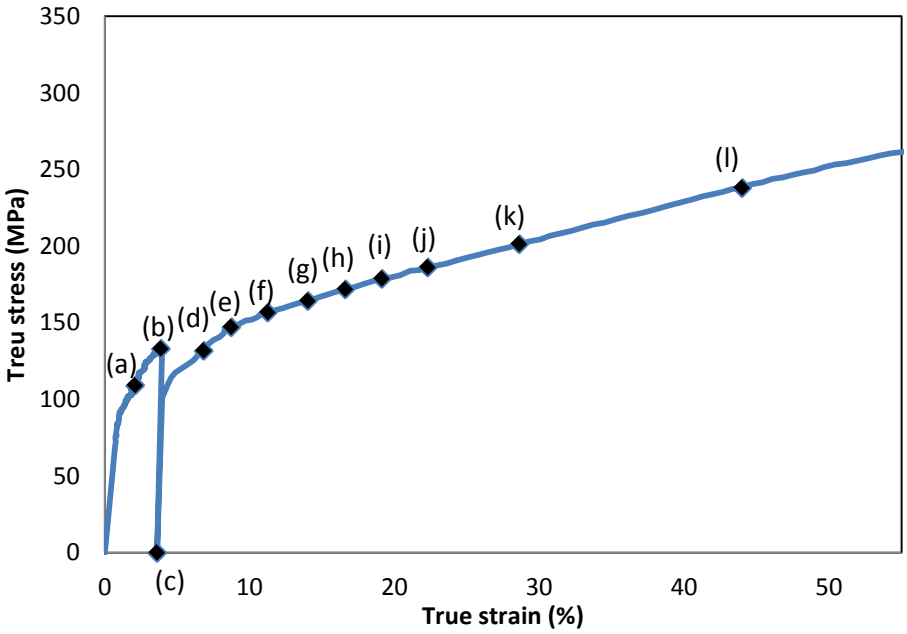

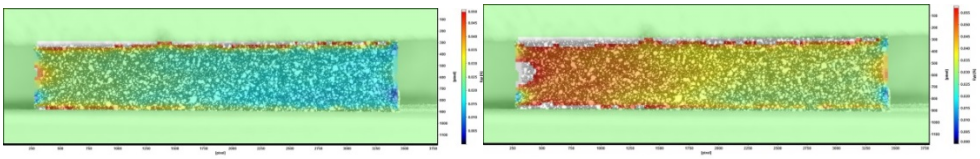

(a) (b)

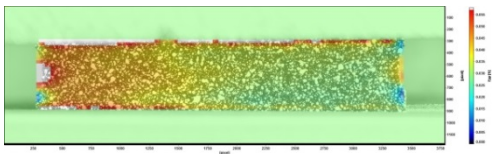

(c)

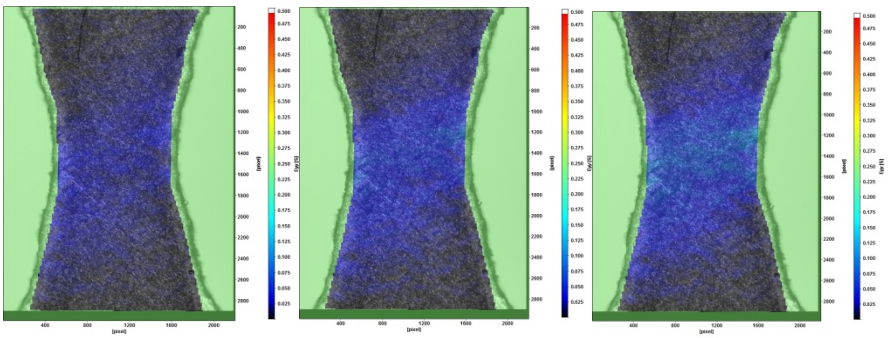

(d) (e) (f)

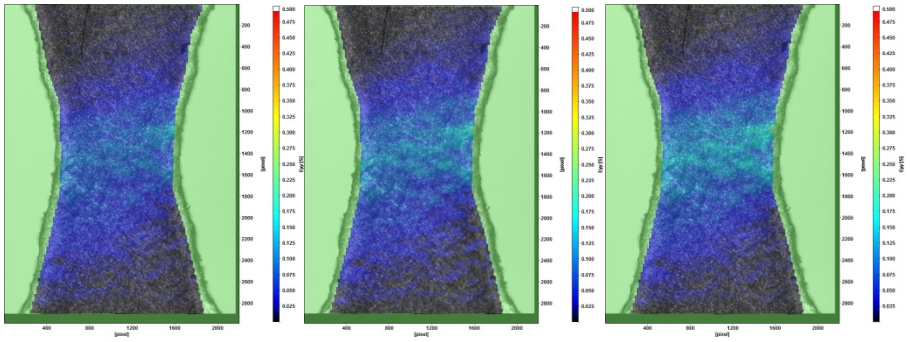

(g) (h) (i)

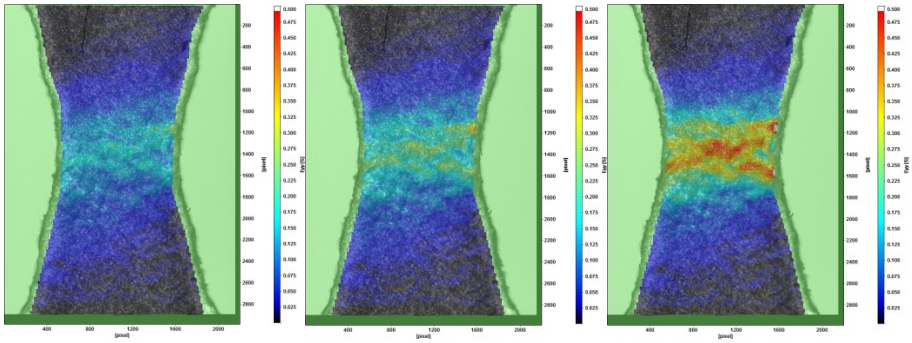

(j) (k) (l)

Figure 112. Stress strain curve of strain path change test (P3_45_S1), which is pre-strained for around 3% and at 45°, and its strain distributions in tensile direction for (a)1.95%, (b) 3.94%, (c) 3.59%, (d)5.97%, (e) 7.94%, (f) 10.06%, (g)11.81%, (h) 14.01%, (i) 16.03%, (j) 18.05%, (k) 24.06%, and (l) 38.02%. (a), (b) and (c) are in the pre-strain stage.

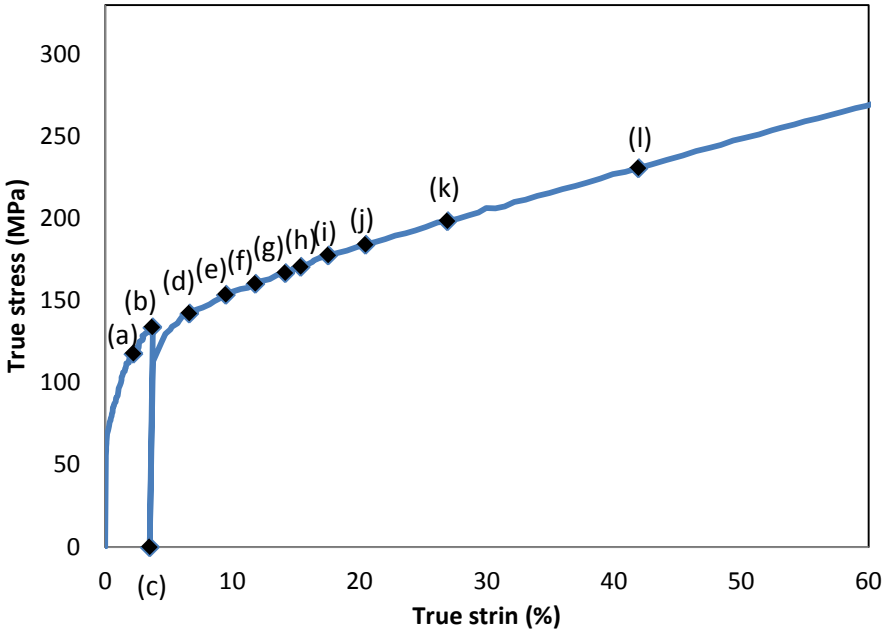
True stress (MPa)
True strin (%)
0
50
100
150
200
250
300
0
10
20
30
40
50
60
(a)
(b)
(c)
(d)
(e)
(f)
(g)
(h)
(i)
(j)
(k)
(l)

(a) (b)

(c)

(d) (e) (f)

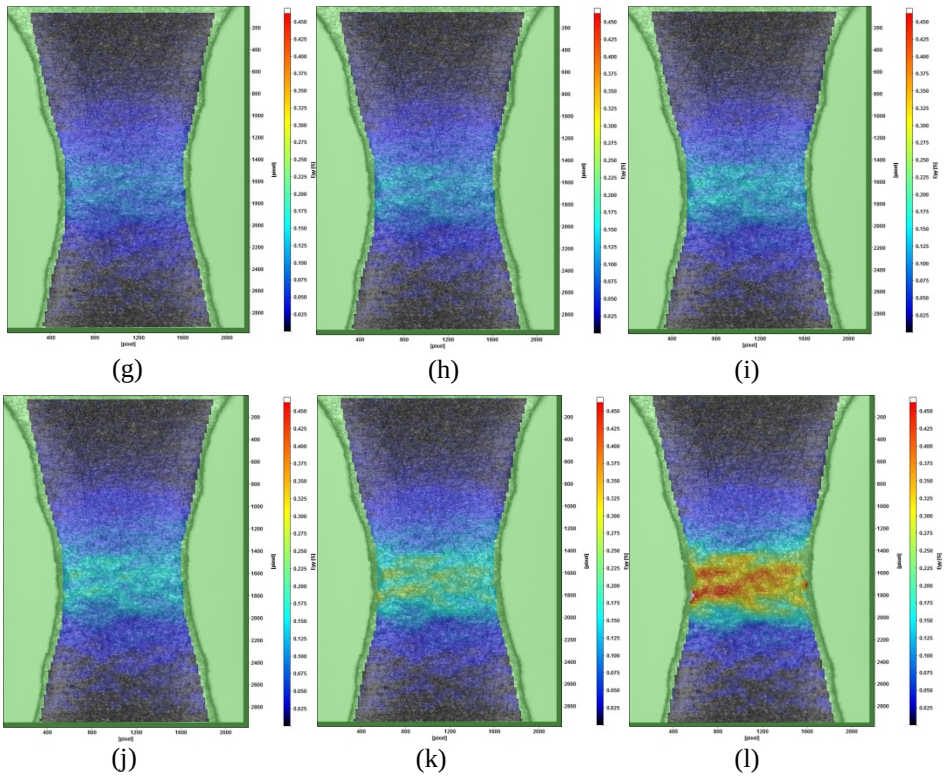

Figure 113. Stress strain curve of strain path change test (P3_90_S1), which is pre-strained for around 3% and at 90°, and its strain distributions in tensile direction for (a)2.08%, (b) 3.99%, (c) 3.73%, (d)6.01%, (e) 7.88%, (f) 9.86%, (g) 11.91%, (h) 14.22%, (i) 15.99%, (j) 18.05%, (k) 24.06%, and (l) 38.22%. (a), (b) and (c) are in the pre-strain stage.

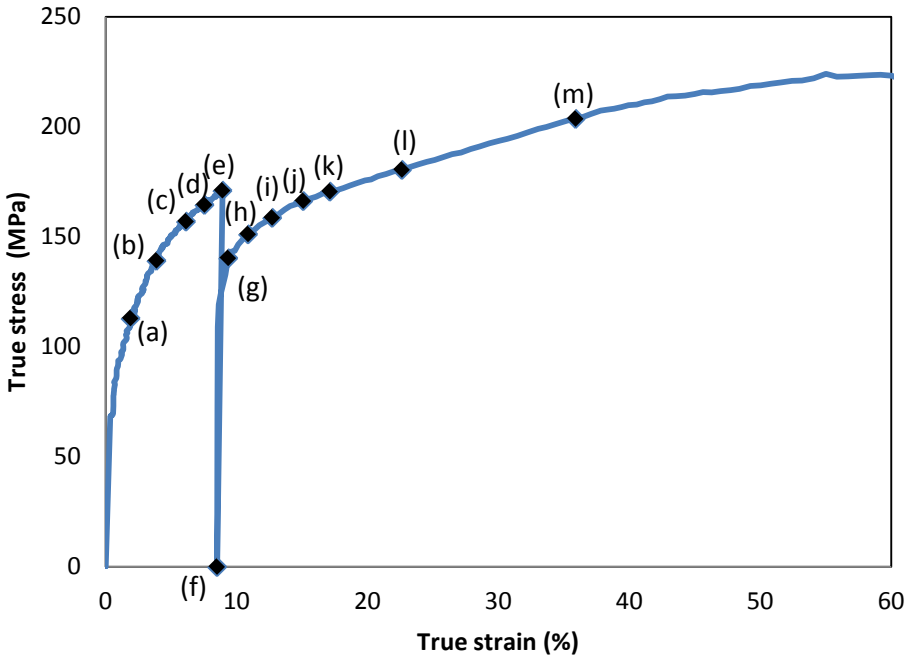
250
200
150
100
50
0
True stress (MPa)
0
10
20
30
40
50
60
True strain (%)
(a)
(b)
(c)
(d)
(e)
(f)
(g)
(h)
(i)
(j)
(k)
(l)
(m)

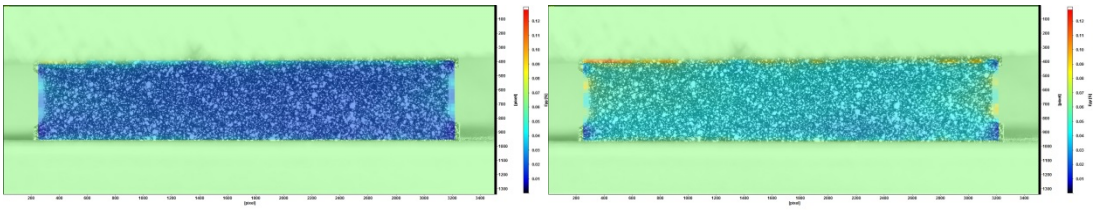

(a) (b)

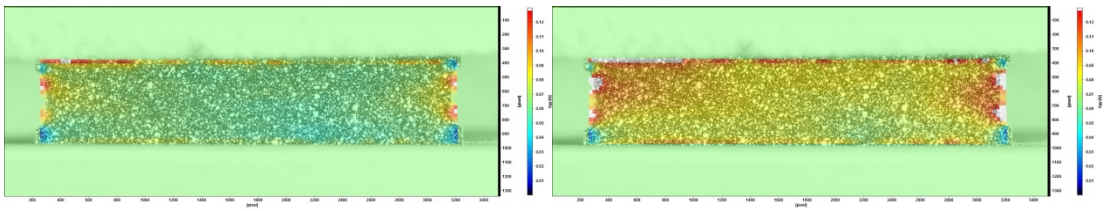

(c) (d)

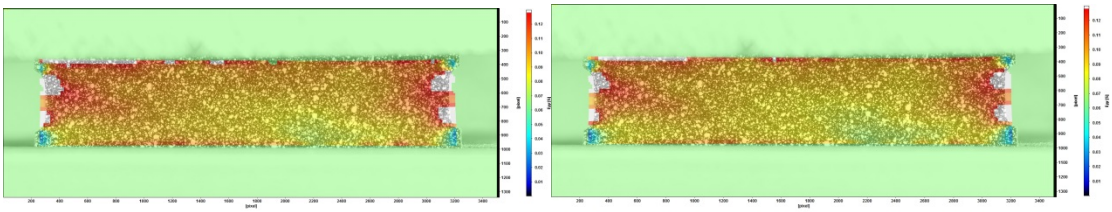

(e) (f)

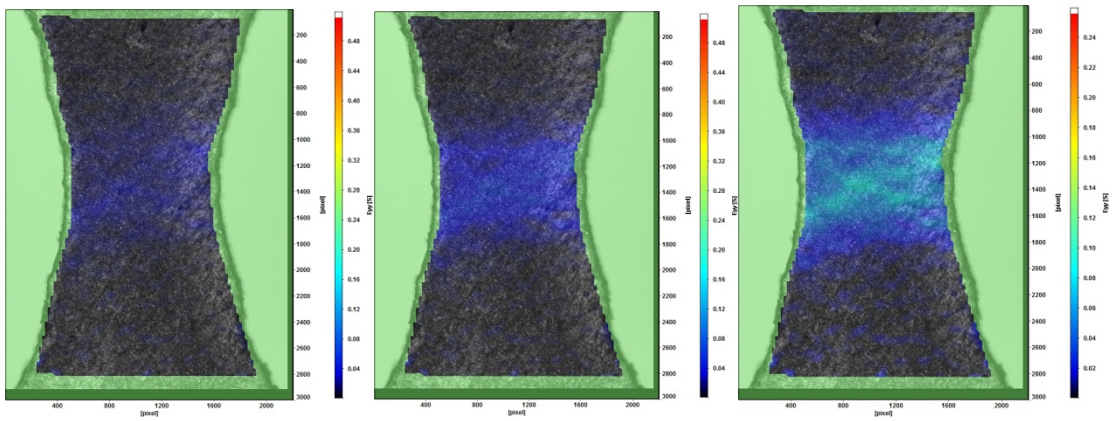

(g) (h) (i)

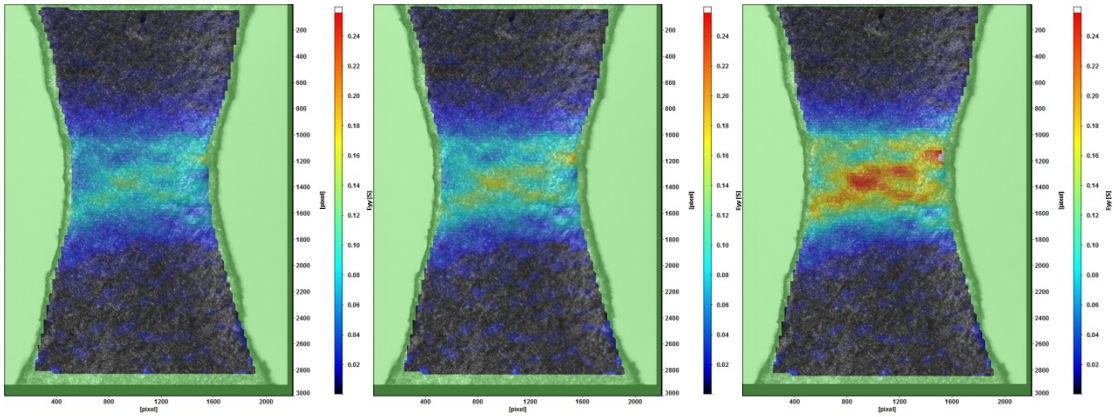

(j) (k) (l)

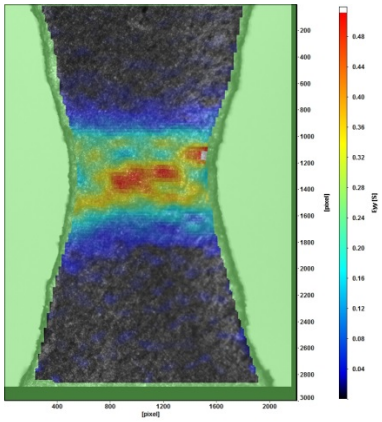

(m)

Figure 114. Stress strain curve of strain path change test (P9_45_S2), which is pre-strained for around 9% and at 45°, and its strain distributions in tensile direction for (a) 1.94%, (b) 4.03%, (c) 5.9%, (d)8%, (e) 8.93%, (f) 8.5%, (g) 10.04%, (h) 12.21%, (i) 14.01%, (j) 15.98%, (k) 18.07%, (l) 23.8%, and (m) 38.2%. (a), (b), (c), (d), (e), and (f) are in the pre-strain stage.

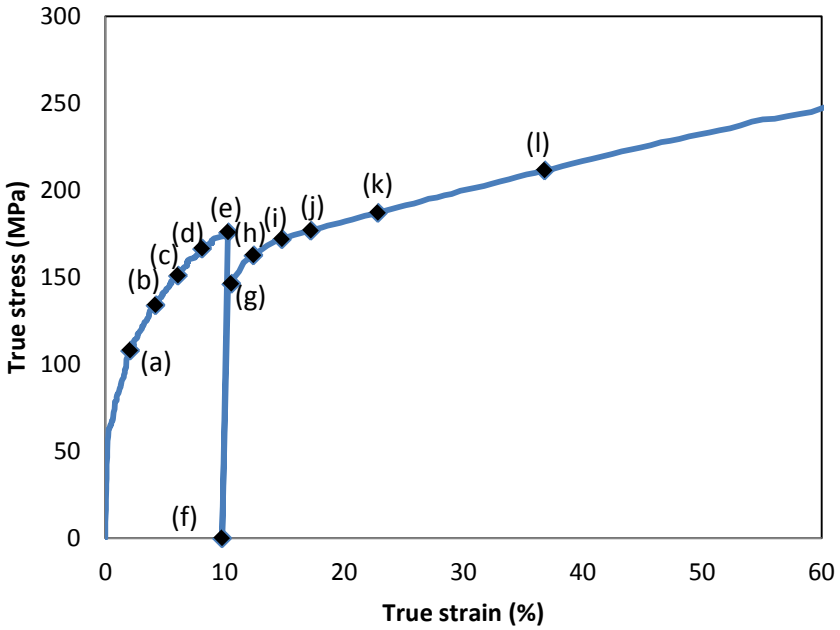
300
250
200
150
100
50
0
True stress (MPa)
0
10
20
30
40
50
60
True strain (%)
(a)
(b)
(c)
(d)
(e)
(f)
(g)
(h)
(i)
(j)
(k)
(l)

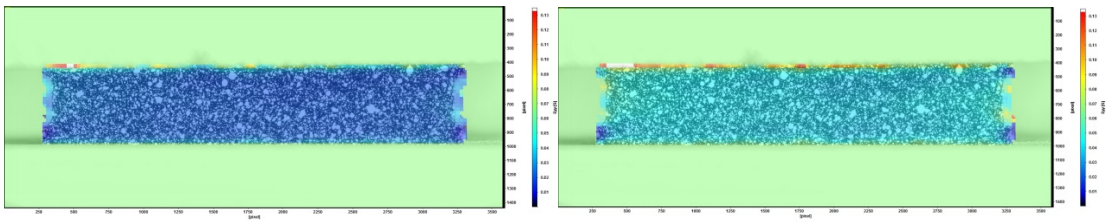

(a) (b)

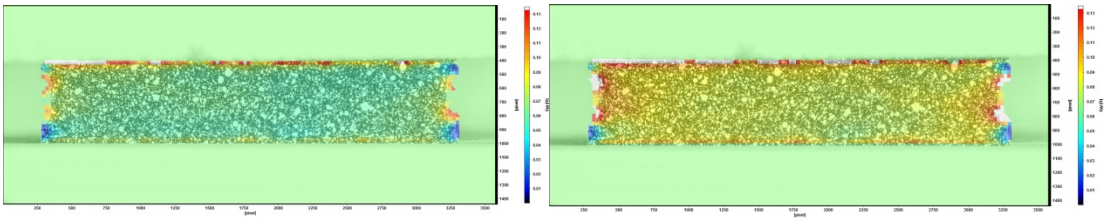

(c) (d)

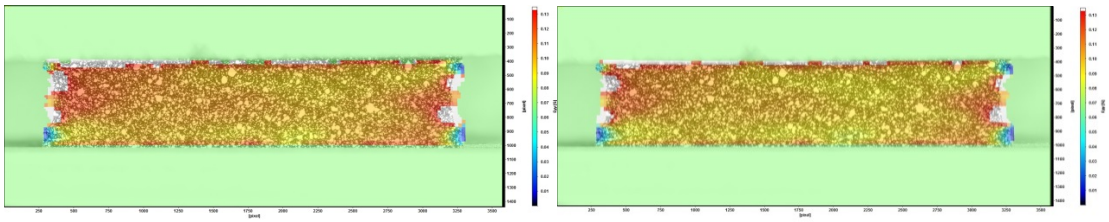

(e) (f)

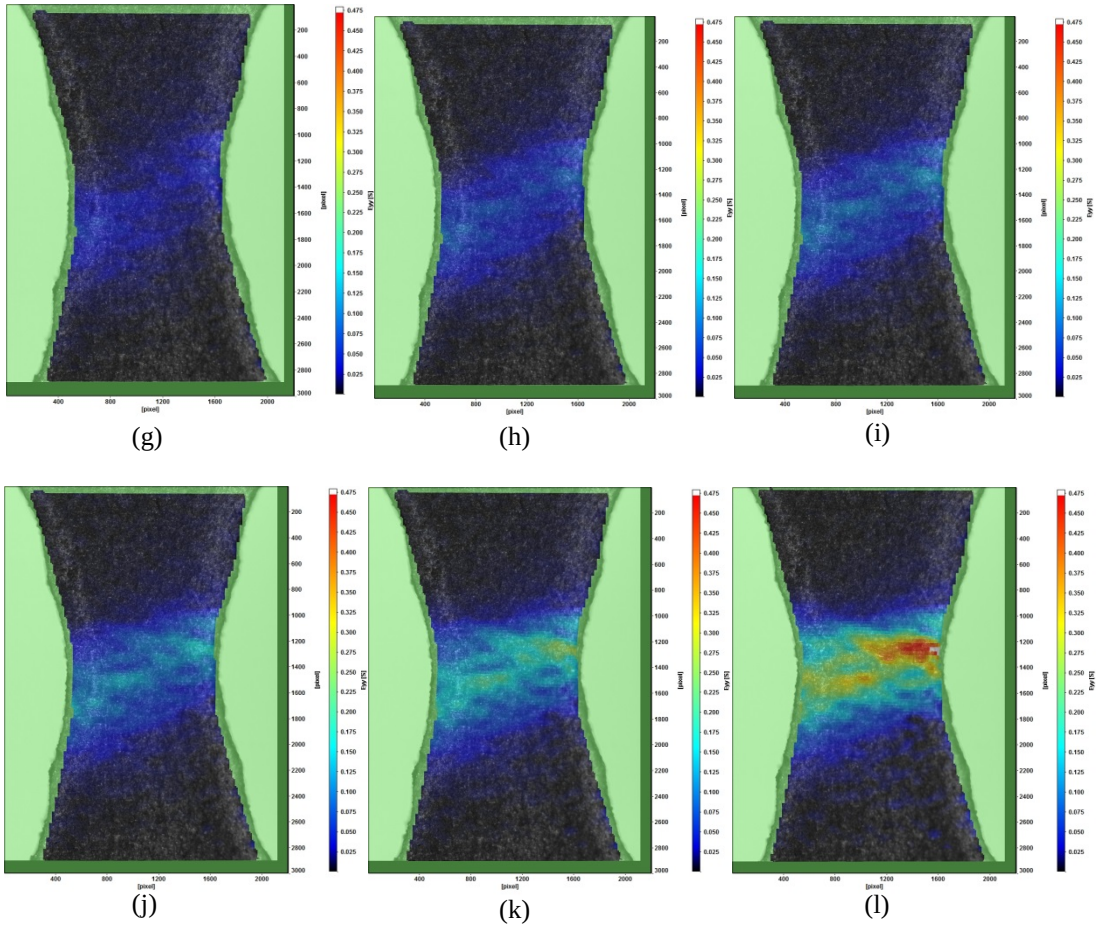

Figure 115. Stress strain curve of strain path change test (P9_90_S3), which is pre-strained for around 9% and at 90°, and its strain distributions in tensile direction for (a) 2.02%, (b) 3.96%, (c) 6.07%, (d)7.93%, (e) 10.27%, (f) 9.77%, (g) 11.91%, (h) 13.87%, (i) 15.86%, (j) 18.19%, (k) 24.18%, and (l) 37.92%. (a), (b), (c), (d), (e), and (f) are in the pre-strain stage.